The effect of landing-gear implementation on Flying V aerodynamics, stability and controllability

by

G. Bourget

in partial fulfilment of the requirements for the degree of

Master of Science

in Aerospace Engineering

at the Delft University of Technology, to be defended publicly on Thursday June 11, 2020 at 9:00 AM.

Student number: 4405420

Project duration: April 15, 2019 – June 11, 2020

Supervisor: Dr. ir. R. Vos, Delft University of Technology
Thesis committee: Prof. dr. ir. L. L. M. Veldhuis, ir. P. C. Roling, Delft University of Technology
Delft University of Technology

An electronic version of this thesis is available at http://repository.tudelft.nl/.



Abstract

Initially conceptualised by Benad in 2015 as a highly-swept flying wing aircraft to replace the A350-900, the Flying V design has since been refined in several later studies at both Airbus and TU Delft. The initial aerodynamic efficiency gain estimation was refined by Faggiano and Rubio-Pascual, confirming the interest of the solution. To prepare sub-scale test flights, wind tunnel tests were performed, showing a complex flow over the wing and providing an aerodynamic model predicting the longitudinal forces and moments in a given condition. In most of these works, the possible influence of the landing gear on the subject studied was mentioned, leading to consider its design. However creating the design itself is not the issue: landing gear have existed for as long as aircraft, thus methods exist to design them and they can be adapted to the Flying V. The more important question is about the influence of the gear on the aircraft: what are the consequences of adding a landing gear to the Flying V? This leads to a four step structure: choosing evaluation criteria for the gear, adapting the design method and criteria computation to work on the Flying V, validating the method and computations, and finally applying them to evaluate the consequences of the gear on the Flying V. Providing both quantified evaluation criteria and explicit design organisation, optimised design methods are used as support for the first two steps. The criteria retained are gear weight, ground manoeuvre, rotation ability, fairing drag, cabin floor height (equivalent to aircraft height from ground) and lateral stability derivatives. The last two were chosen after an exploratory study showing that the gear tends to be long, and can be shortened by increasing wing dihedral. The design methods from literature are adapted by removing the optimiser, and limiting the amount of iterations required since the gear design space on the Flying V is not fully known, which require designer decision more frequently than on conventional aircraft. Validation proves that the modified method is accurate when applied to the A350-900, with the only difference being a smaller gear track. Chosen for their simplicity, the empirical methods used to compute gear weight, shock absorber length (required in gear length) and stability derivatives prove to be quite inaccurate. The other criteria are computed using geometry, and show much better accuracy since there is no assumption of the aircraft configuration as for empirical methods. Following the outcome of the exploratory study, it is chosen to study two airframes with modified dihedral in addition to the original Flying V. The first is chosen to bring the cabin floor at 5.5 m from the ground, the second to have gear as short as possible. The main gear on the original Flying V is 6 m long, placing the cabin floor also at 6 m from the ground for an estimated total gear weight of 12.8 t. This is 10 % higher than the A350-900, and the gear is 20 % heavier than the A350-900 gear, for a similar mission and an expected lower take-off weight. The other criteria are satisfactory. The gear on the modified airframes reduce in length by 12 to 56 %, while reducing in weight by 4 to 25 %, confirming the interest of varying dihedral as suggested in the exploratory study. Other criteria are unchanged by the dihedral variation, except for the lateral stability derivatives. Comparing with an airliner, rolling moment derivative due to sideslip is found to be 3.5 times larger, raising the question of Dutch roll and of controlling the roll angle when landing with sideslip. The other computed derivatives are slightly better but not showing interesting trends when dihedral increases. The consequences of a gear on the Flying V are then either to reduce the payload to accommodate the long and heavy landing gear, or to face undesirable stability derivatives if the gear is made shorter through dihedral.

Acknowledgements

This master thesis is the result of about one year of work, and would not have reached its end without many people I want to thank.

First and foremost, Roelof Vos for being my supervisor during this thesis, and asking the questions I was either neglecting or didn't even think of. These put me back on track more than once, by stopping me from falling further down in a useless rabbit hole, or by pointing to directions I was overlooking. Being new to research work as my previous studies didn't include any, I would have struggled much more without his guidance.

Next to Maurice Hoogreef for stepping in for green light and bringing a different point of view which made shortcomings of my paper clearer to me. And to all the Flying V team, those working or who worked on that fantastic project: Marco, Alberto, Jan-Willem, Malcolm and all the others I have not met or whose name I forgot. Without their work on the Flying V I would not have been able to do this thesis.

Then to the Rotterdam Ravens quidditch team, and all quidditch players I've met while working on this thesis, for being the most awesome group of people I've ever joined. My mental health and my ability to keep going through this whole project owe you a lot.

And finally to my family for the never ending support from the start of this master in Delft to the end of the thesis, at home in France, during coronavirus outbreak.

Grégoire Bourget May 2020

Contents

Li	st of Figures	ix
Li	st of Tables	хi
1	Introduction 1.1 The Flying V	2 3
2	Literature Review 2.1 Landing gear design methods	
3	Gear design and analysis process 3.1 Overall architecture of the process 3.2 Exploratory study 3.3 Stability derivatives 3.4 Design and analysis 3.5 Bogie and tire choice. 3.6 Outrigger initial design 3.7 Main gear initial design 3.8 Main gear refinement 3.9 Nose gear initial design 3.10 Final gear design 3.11 Figures of merit.	12 14 16 18 20 22 23 26 27
4	Process validation 4.1 Position and length	37 38 38 41
5	Results5.1 Exploratory study outcome5.2 Three airframe configurations5.3 Gear design5.4 Evaluation of the figures of merit5.5 Discussion	47 47 57
6	Synthesis 6.1 Conclusion	
A	Turning radius validation data A.1 A350-900	

В	Flying V turning radii	71
	B.1 Turning radii raw data	. 71
	B.2 Comparison with existing aircraft	. 72
Bi	bliography	75

List of Figures

1.1 1.2	Flying V conceptual design (a) 3D rendering, and (b) take-off estimation in side view Flying V preliminary design (a) planform evolution, with A350-900 as reference, and (b)	1
1.2	orthogonal cross section showing the oval fuselage gains in airfoil utilisation	2
2.1	Chai and Mason automatic gear analyses process	6
2.2	Heerens automatic gear design process	7
	Van Oene automatic gear design process	8
2.4	Ground handling equipment required for a Boeing 777	10
	Flow chart of the process overall architecture	11
3.2	Flow chart of exploratory study	12
3.3	Gear position constrained by longitudinal tipover	13
	Dihedral distribution over span, and effect on wing tip height	14
3.5	Antisymmetric effect on the wing due to (a) lateral flow over the nacelle alone, for (b) nacelle in front and below of the wing and (c) nacelle aft and above the wing	16
3.6	Flow chart of gear design and analysis process	17
3.7	Examples of simple landing gear kinematics	18
	Flow chart of bogie and tire choice	18
3.9	Relation between aircraft maximum take-off weight and wheel number	19
	Gear folding margin computation	20
	Flow chart of outrigger initial design	21
3.12	Flow chart of main gear initial design	22
3.13	Computation of landing gear strut length	23
	Flow chart of main gear refinement	24
	Flow chart of nose gear initial design	26
3.16	Flow chart of final gear design	27
	The lateral turnover angle and associated inertia effects	28
	Gear folding axis computation	30
		30
	Fairing shape chosen	31 31
		37 38
4.3		39
4.4		40
		40
	Increase of rudder efficiency with deflection	41
	Variation of pitch and roll moment with elevon deflection	42
4.8	Comparison of Flying V and equivalent wing	44
4.9		44
4.10	Validation fo stability derivatives due to sideslip, part 2	45
5.1	, , , , , , , , , , , , , , , , , , , ,	48
5.2	Flying V lift curves with no control surface deflection	48
5.3	Control surface deflection required for zero total pitching moment	51
5.3	Control surface deflection required for zero total pitching moment	52
5.4	Option considered to fit the nose gear	53
55	Weight-cg diagram focused on nose load limits	54

5.5	Weight-cg diagram focused on nose load limits	55
5.6	Flying V landing gear along with airframe	56
5.7	Isometric view of Flying V gear folding process	57
5.7	Isometric view of Flying V gear folding process	58
5.8	Evolution with dihedral increase of derivatives due to sideslip	61
5.8	Evolution with dihedral increase of derivatives due to sideslip	62

List of Tables

2.1	Door and airframe height for different aircraft	10
4.1 4.2 4.3	Lift coefficient and incidence for A350-900 take-off and landing, from NASA HL-CRM Shock absorber stroke validation	36 38 43
5.11 5.12 5.13	Outrigger characteristics for the different configurations Center of gravity range for the Flying V Final main gear position and strut length Final nose gear position and strut length Main gear braces position and length Gear weight estimation for the different configurations Corrected gear weight estimation for the different configurations Gear characteristics relevant for ground maneuvering Cabin floor height for the different configurations Zero-lift drag of the fairing for each configuration Comparison of sideforce derivative due to sideslip with a conventional airliner Comparison of rolling moment derivative due to sideslip with a conventional airliner	47 49 50 52 53 55 58 59 60 60 62 63
A.2 A.3	Turning radii validation, A350-900 part 2	69 69 70 70
B.2 B.3 B.4 B.5	Turning radii of the Flying V, part 2	71 71 72 72 72 73

Nomenclature

Variables

\boldsymbol{A}	Wing aspect ratio	-
b	Aircraft span	m
$\bar{\mathcal{C}}$	Mean aerodynamic chord (MAC) of the aircraft	m
$\mathcal{C}_{ ext{L}}$	Lift coefficient of the aircraft	-
$C_{\mathrm{L},lpha}$	Lift curve slope	rad^{-1}
$C_{ m m}$	Pitching moment coefficient	-
D	Drag of aircraft	N
$F_{\rm stat}$	Nose strut static loading	kg
$F_{ m dyn}$	Nose strut dynamic loading (braking)	kg
h	Height of a point of the aircraft w.r.t. ground	m
$h_{ m req}$	Required height at a point of the aircraft to meet ground clearance	m
$J_{ m W}$	Wing influence factor on vertical fin	-
L	Lift of the aircraft	N
l	Length of item	m
m	Mass of the item specified in subscript	kg
$m_{ m AC,to}$	Mass of the aircraft at take-off	kg
M	Mach number	-
N	Number of wheel on one gear strut	-
r	Turning radius of point specified in subscript	m
R	Radius of item	m
Re	Reynolds number	-
S	Shock absorber total stroke	m
s_{t}	Tire deflection under landing impact load	m
T	Thrust of the aircraft engines	N
v	Aircraft horizontal airspeed	m/s
$v_{ m s1g}$	Stall airspeed of the aircraft in 1g flight	m/s
$v_{ m z}$	Sink speed of the aircraft during landing	m/s
W	Width of item	m
X	Position along x-axis, standard airframe axes	m
y	Position along y-axis, standard airframe axes	m
Z	Position along z-axis, standard airframe axes	m
β	Nose wheel steering angle	degree
$\eta_{ extsf{s}}$	Shock absorber efficiency	-
$\eta_{ m t}$	Tire shock absorbing efficiency	
γ	Flight path angle	radians
Γ	Wing dihedral angle	degree
Λ	Wing sweep angle	degree
φ	Aircraft roll angle	degree
ψ	Turnover angle	degree
θ	Pitch angle for aircraft, or strut angle w.r.t. vertical for gear	degree
$ heta_{ ext{bogie}}$	Tilt angle of the bogie w.r.t. strut	degree

Subscripts

 O_{ldg} Relative to landing O_{lof} Relative to lift-off

O_{lrp} Relative to longitudinal rotation point

 O_{\max} Maximum

 $\bigcirc_{ ext{tip}}$ Relative to wingtip $\bigcirc_{ ext{turn}}$ Relative to axis of ground turn

Constants

 $\begin{array}{ll} g & \qquad \qquad \text{Gravitational acceleration on earth} & 9.81\,\text{m}\,\text{s}^{-2} \\ N & \qquad \text{Reaction factor for shock absorber stroke} & 1.5 \end{array}$

 $\begin{array}{lll} \rho_{air,MSL} & \text{Air density at mean sea level} & 1.225\,\text{kg}\,\text{m}^{-3} \\ S_{fin} & \text{Reference area of one vertical fin} & 20.0\,\text{m}^2 \\ S_{ref} & \text{Wing reference area} & 883.35\,\text{m}^2 \end{array}$

Introduction

1.1. The Flying V

The Flying V is a V-shaped flying wing aircraft which initial concept was created by Benad [1] to meet the same mission as A350-900 with improved efficiency. This concept is shown in Figure 1.1. The improved efficiency is obtained by a higher integration of the different components. Benad's main idea is to keep circular section fuselage for easier pressurisation, but to align it with the leading edge of a highly swept wing thus providing an oval streamwise section around which a wing profile is easier to create. His conceptual design conclude to a 10% higher lift-to-drag ratio with a 2% lower mass compared to A350-900. A low take-off angle is estimated due to favourable aerodynamic behaviour, leading to a short gear when addressing take-off and landing, as shown in 1.1b.

Such possible improvements triggered the start of preliminary design to refine them. Faggiano [2, 3] performed an aerodynamic optimisation through Euler method CFD computations, leading to a significant sweep increase of outer wing to reduce drag. The aerodynamically optimised planform showed a 25% increase of lift-to-drag ratio compared to the reference aircraft, representative of state-of-the-art conventional airliners. It is compared with conceptual design and A350-900 in Figure 1.2a. These results are however limited to a clean wing in cruise, thus Faggiano states that the performance will decrease when protuberance will be added, and that low speed flight phases need to be investigated to eventually adjust the wing since high lift devices are unusable on flying wing aircraft.

In parallel, structural analyses were performed to ensure the configuration does not bring increased structural weight that would negate the aerodynamic efficiency improvement. Faced with model and software issues, van der Schaft [4] could not provide a reliable weight evaluation, but introduced the oval fuselage from [5] instead of the circular fuselage of Benad. This brings a more efficient airframe space use, as shown in Figure 1.2b, thus reduces the span fraction occupied by the fuselage. Despite the unreliable weight estimation, qualitative observation were made on the locations with highest stress

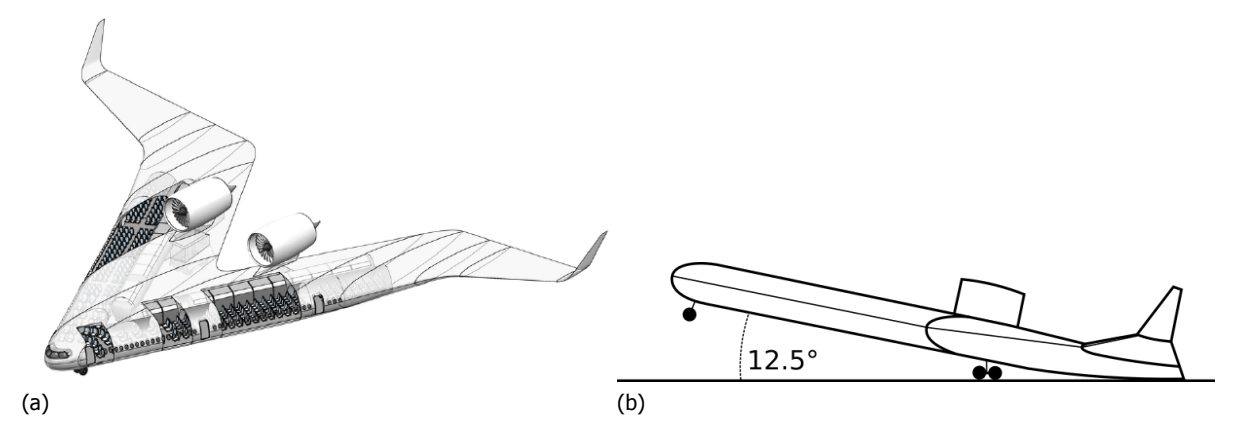


Figure 1.1: Flying V conceptual design (a) 3D rendering, and (b) take-off estimation in side view

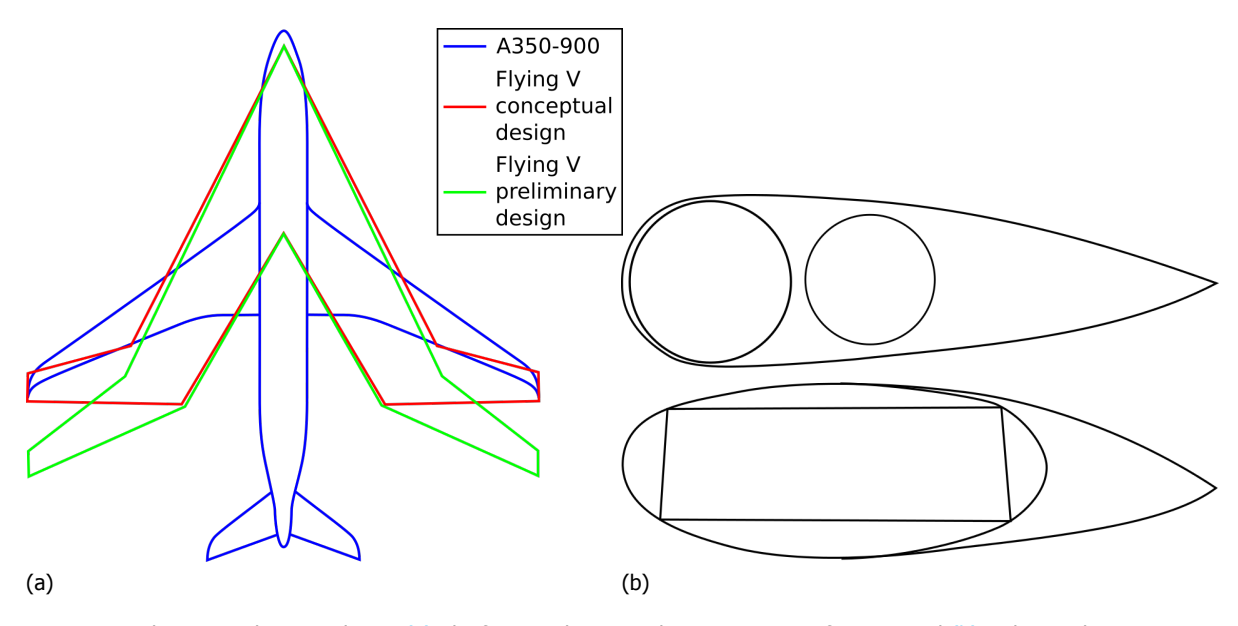


Figure 1.2: Flying V preliminary design (a) planform evolution, with A350-900 as reference, and (b) orthogonal cross section showing the oval fuselage gains in airfoil utilisation

and determining which design cases brought these stresses. It is shown that take-off and landing design cases are critical for a large part of the structure including most of the spars and the skin on outer wing. While the gear location used is roughly assumed thus will change, it shows the influence of its location on structure.

Van der Schaft also set up with Faggiano a knowledge-based engineering (KBE) model of the Flying V in ParaPy [6]. Relying on ParaPy capabilities, this model generates the Flying V shape from a set of input parameters, providing access to multiple automatically computed values with guaranteed update should the parameters change. This will prove very useful for the current work as discussed in 3.2.

Compared to Benad, Faggiano considered only clean wing, thus his results over-estimate the full aircraft performance. This was confirmed by Rubio-Pascual [7] when integrating the engine, showing that, for the engine configurations considered, the minimum decrease of aircraft lift-to-drag ratio is $10\,\%$, similar to existing airliners. If the engine is misplaced, the decrease is much higher, going up to $55\,\%$ compared to ideal position. It is shown that the engine should be slightly above the wing and aft of its trailing edge for best performance. Considering the engine weight, Rubio-Pascual suggests to position each one above a main gear strut so they can share their structure and limit influence on mass and centre of gravity position.

More recently, wind tunnel tests were conducted to prepare sub-scale test flights [8–10], which results gave insights on flow complexity, stability and were aggregated in an aerodynamic model of great use to easily predict the forces an moments in a given flight phase. The sub-scale flight tests are planned to investigate flight dynamics of the aircraft, therefore a Froude-scaling is used to maintain the flight dynamics similarity. The Reynolds number is thus heavily modified, reducing the aerodynamic forces similarity with full scale, thus requiring aerodynamic model adjustments to be used on full scale. The stability results and aerodynamic model are used to suggest centre of gravity and gear positions for the sub-scaled model. The quite flat lift curve obtained by the sub-scaled model increases the take-off incidence compared to Benad's estimated value, raising the issue of gear length.

1.2. Problem statement

While not yet designed, the gear was already considered in three out of four studies on full scale aircraft, and in all three studies on sub-scaled aircraft. Neglecting Benad study as conceptual design address quickly most aspects of the aircraft, the two others full scale studies were interested in the landing gear for its interaction with the disciplines studied. On the other hand the sub-scaled model studies were interested in the gear for its direct use in take-off and landing, such that dynamics in all flight phases (including take-off and landing) could be covered when testing the model.

The importance of landing gear is already known in aircraft design, and the Flying V is no exception as shown in previous paragraph. Adding the landing gear to the current Flying V would allow to refine structure and weight estimation, as well as studying low speed phases, thus making more precise the estimation of Flying V gains compared to existing airliners. Gear design methods exist for conventional airliners, and they can be adapted to the Flying V unconventional shape.

Therefore the problem is not designing the gear, but determining the influence it will have on the aircraft, as this can determine if the Flying V is a feasible design. Moreover, since the Flying V is still in preliminary design phase, the configuration will likely change, requiring to redesign the gear and re-evaluate its influence. Thus the design and analysis method needs to be sufficiently accurate while allowing for relatively quick iteration when the Flying V is modified.

1.3. Research objective

To solve the problem stated above, the objective of this work is thus to evaluate the consequences of the landing gear on the other disciplines of the Flying V, by designing a preliminary gear for the Flying V and applying adequate analysis methods.

This raise several questions: How are landing gear designed? Which figures of merit are used to evaluate a gear design? How are the figures of merit computed for the Flying V? Which gear can be designed for the Flying V? How does that gear perform in terms of the defined figures of merit? How does that gear compare to other gear? These questions can be synthesised in a single research question that will drive the thesis:

What are the consequences on the Flying V of adding a landing gear to it?

1.4. Thesis outline

To answer the research question, the subquestions listed before all need to be answered in order. In 2, literature landing gear design methods will be investigated to identify the steps required to design a gear for the Flying V. Since gear are designed to be used, design methods come along with criteria to evaluate the design created. This will allow to determine interesting figures of merit to evaluate the Flying V gear.

Then in 3, the design method and the figures of merit computation will be adjusted to match the Flying V specificity, but mostly to match the need of a sufficiently accurate design and analysis method providing results in reasonable time. The adjusted method and figures of merit computations are then validated in 4 to ensure their correctness and quantify their accuracy. Once validated, the method and computations are applied on the Flying V in 5. They provide a gear design and its evaluation, which are then discussed and compared to existing gears, drawing trends and outlining trade-off. Finally in 6, the research question is answered by stating the consequences of fitting a gear on the Flying V, outlining the limits of current work and suggesting future research directions.

Literature Review

In this chapter, gear design methods in literature are reviewed and discussed for their applicability to the Flying V. The design workflow and the figures used to assess the final gear are the main focus.

2.1. Landing gear design methods

Landing gear have existed for as long as aircraft, and had to evolve alongside it to satisfy the needs of new aircraft. The design methods and design options have thus evolved as well. A chapter on gear design can be found in every aircraft design textbook, with more or less details depending on if the book address conceptual design such as [11] or preliminary design such as [12, 13]. More detailed gear design process literature is less common, with Conway [14] and Currey [15] as main sources, the latter considering his work to be a well-needed update and rework of the former. Currey's work is widely reused in later publications, and considered as "one of the most valuable references in landing gear design" [16, p. 431].

However the landing gear design methods presented in the textbooks above are experienced-based and do not present the items in the order in which they are to be applied to design a gear from scratch. This makes them not directly applicable to automatic design, as remarked by Chai and Mason [17, p. 1] and Van Oene [18, p. 1]. This observation led them to re-arrange the different aspects of landing gear design in a sequence usable for automatic design, including an optimisation. While not stating the inadequacy of literature for optimisation, a similar objective is achieved by Heerens [19] earlier in the same project as Van Oene, which work aimed at solving some shortcomings of Heerens' work. The design strategies developed in these three work are now presented and discussed.

2.1.1. Chai and Mason automatic design

The structure of Chai and Mason design method [17] is shown in Figure 2.1. A gear geometry is created from input parameters in CONFIG, and is then analysed in PAVE to determine the runway stress it generates (the flotation), in LIMIT to check various constraints determined by user or regulation, and finally in GEARWEI to estimate its weight. The outputs are then generated.

CONFIG requires generic aircraft shape parameters, but also specific gear parameters such as gear location, number of wheels and tires, stowage space. It is stated that the code does not have the capability of deriving those gear parameters from the aircraft geometry alone. Thus these parameters are left to be varied manually by the user or an optimiser. User modifications are also required within the method in case the input parameters provide a configuration that violates design constraints. This is an improvement over the textbooks above in the sense that the analyses to be performed are ordered, but the method is more an automatic analysis method than a design method, as no design decisions are taken within the described modules.

2.1.2. Heerens automatic design

The structure of Heerens design method [19] is shown in Figure 2.2. From aircraft geometry data and aircraft preliminary sizing, a complete gear is designed in successive steps. The design process is included in an aircraft design framework, thus making the obtained design available to run additional

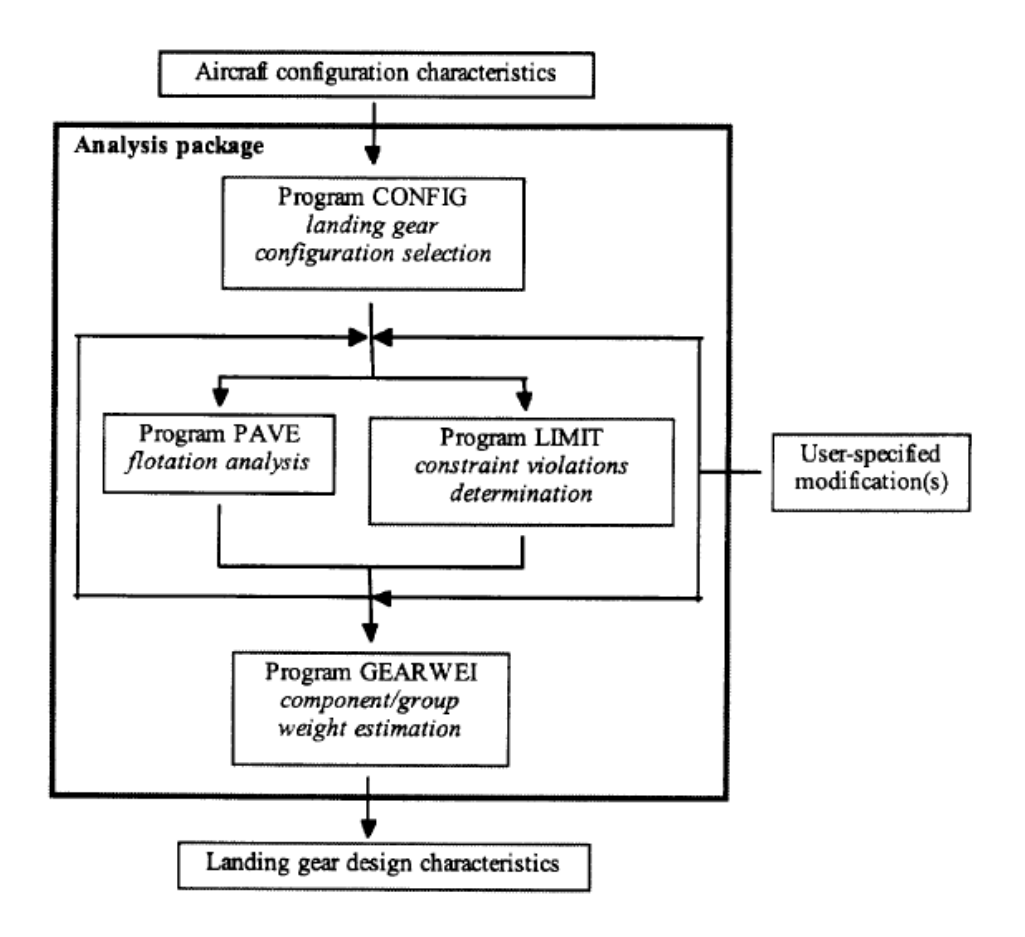


Figure 2.1: Chai and Mason automatic gear analyses process[17]

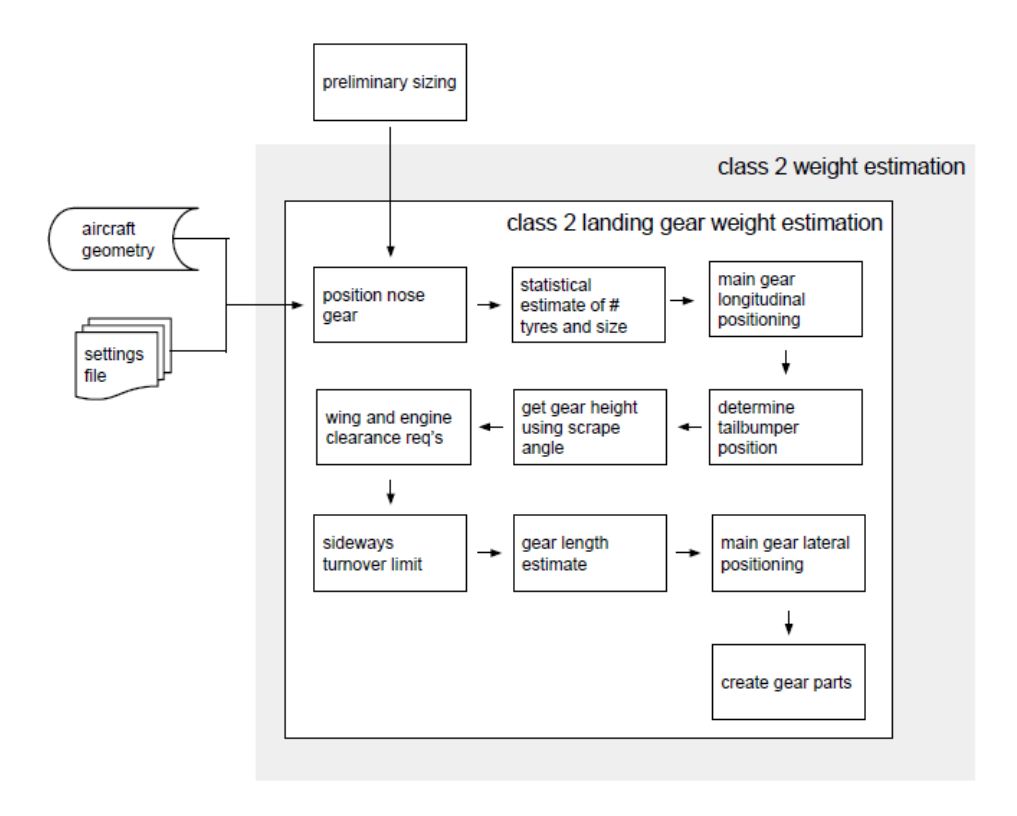


Figure 2.2: Heerens automatic gear design process[19]

analyses. Compared to Chai and Mason method, this is an actual gear design process, requiring only aircraft geometry to produce a gear.

The number of wheels and their size is estimated statistically and they are arbitrarily positioned w.r.t. each other. Flotation computation is performed using existing programs linking it to wheel position [20] according to the ICAO standard [21], but does not seem to be iterated on. Several constraints checked by Chai and Mason after the gear is placed (lateral stability, scrape margins) are here checked within the design process to directly position the gear where the constraint is satisfied. This eliminates the need for user intervention if the constraints are not met.

It is quite interesting to note that the nose gear is placed first using loading limits, while load computation requires to know both gear positions [12, 13, 15].

2.1.3. Van Oene automatic design

The structure of Van Oene design method [18] is shown in Figure 2.3. This work came after Heerens in order to solve a major issue: the gear design process came after the aircraft configuration was fixed, preventing many configurations to have a feasible landing gear because the gear could not be attached to the structure. Van Oene solves this by allowing the wing to move such that the gear can be attached to the structure, while accounting for the effect of moving the wing on aircraft characteristics. Thus compared to Heerens designing an optimal gear for a fixed configuration, Van Oene could be said to design an optimal gear-wing combination.

As for Heerens, the bogie and tire choice are done statistically from existing aircraft based on maximum take-off weight (MTOW). Before considering moving the wing, a first design try is made, which is then used as starting point to optimise the wing position to get a better gear. This allows to restrict the possible changes to the wing, preventing the gear addition to completely change the aircraft configuration. The gear strut design is limited to computing the strut length (including shock absorber) and position, while for Heerens and Chai and Mason it included defining the different structural elements to allow for later structural sizing.

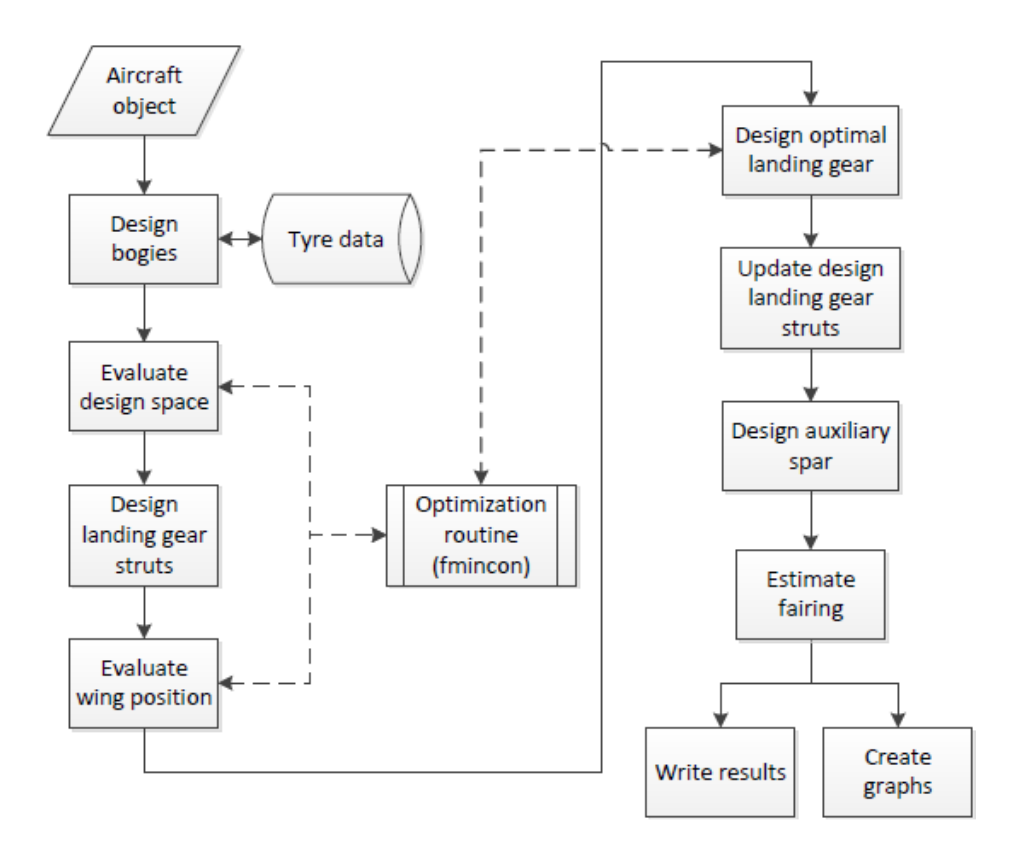


Figure 2.3: Van Oene automatic gear design process[18]

2.2. Landing gear design figures of merit

The three previously described design process aim to provide an optimal gear, thus in addition to design steps, there are also values that were chosen to determine which gear is better than the other. In the LIMIT analysis component, Chai and Mason mention many computed values such as lateral turnover, ground clearance or longitudinal stability at touch-down. They can be used to evaluate the gear design, but Heerens and Van Oene showed that some are better used within the design process to ensure that the gear design created meets these requirements.

2.2.1. Weight

The main evaluation value is weight, appearing in all three processes. Heerens include the gear design process within a weight estimation, to immediately attach a weight to the design and evaluate the aircraft performance based on this. Van Oene states that the final gear chosen among all the possible designs is the lightest. This importance is simply because on any aircraft the gear is used only on the ground, and is a dead weight all along flight, thus a heavy gear is a penalty during flight, reducing payload.

2.2.2. Flotation

Flotation is computed accurately by Chai and Mason and Heerens, thus it is considered an important parameter to evaluate a gear design. Van Oene does not clearly specify if it is computed or simply estimated. With the available programs [20, 22] accurate computation is feasible from bogie geometry and gear load. However Currey [15] suggests a different approach: selecting the bogie of an aircraft of similar weight and similar mission (passenger, cargo, military, ...) will ensure similar flotation. This allows to move on with the design, and refine the bogie later on to meet the exact needs of the aircraft, but removes flotation from the possible gear evaluation parameters.

2.2.3. Ground manoeuvring

Turning radii and ground manoeuvring characteristics are computed by all three. Flotation determines if the pavement is structurally able to withstand the aircraft, while ground manoeuvring determines if the aircraft is able to reach the different parts of the airport. Thus the two are equally important. Van Oene even uses it as part of the design process, by selecting the gear design that allows the lowest wheelbase (longitudinal distance from nose gear to main gear) as it helps improving the aircraft ground manoeuvrability.

2.2.4. Fairing drag

Only Van Oene considers fairing design, since some gear configurations covered by his design process require a fairing. The fairing can have a large impact on the aircraft performance through drag (skin friction, but also interference with other airframe components), thus it can be an important evaluation parameter. This is not the case in Van Oene since the fairing drag is computed at the end without influencing the gear choice. A major limit to using the fairing drag to evaluate the gear is that only skin drag can be easily estimated from the fairing shape while interference drag requires more advanced simulation.

2.2.5. Rotation ability

Chai and Mason, Heerens and Van Oene were focusing on conventional tube-and-wing airliners, however the Flying V is a flying wing aircraft, which are known to have lower control surface efficiency due to a shorter moment arm w.r.t. centre of gravity [12]. The effect of gear on take-off ability is acknowledged by Van Oene, but it is considered that horizontal tail sizing will take place later and thus account for the increased required authority.

This cannot be done on the Flying V, as the pitch control surfaces are included in the airframe planform which was optimised earlier. Compared to the historical low sweep angle flying wings aircraft, the Flying V high sweep increases the moment arm. However Figure 1.2a showed the much shorter airframe compared to A350-900, making clear that control surfaces moment arms will still be shorter on the Flying V. Thus an additional evaluation parameter for the gear could be the ability of the Flying V to rotate for take-off.

A possible solution to this is provided in [23] by using active lengthening/shortening all of the gear struts to reach the appropriate attitude for take-off. Another option is the nose jump-strut in [24] pushing the aircraft nose up at the beginning of rotation to reduce the force required from pitch control. Such active systems raise the issue of reliability, but could help making the Flying V gear feasible.

2.2.6. Ground handling

Different from ground manoeuvring, ground handling regroups all the activities happening around the aircraft from the moment it arrives at, to the moment it leaves the terminal. This includes passenger (de)boarding and refuelling, but also multiple other operations that require to access to the airframe or the aircraft doors using special equipment as shown on Figure 2.4. Therefore if the current equipment cannot reach the airframe, there will be extra costs. It can be checked in Table 2.1 ¹that airframe lower surface height and cabin floor height do not exceed respectively 2.5 m and 5.5 m, for aircraft of similar mission to the Flying V. It can thus be assumed that ground handling material is not made for much higher values, therefore evaluating the gear impact on airframe height could be a justified assessment parameter.

The Flying V has only one deck, giving it a very thin airframe, thus the difference between airframe lower surface and door heights will be small, and only one of the two can be checked to see if ground handling is satisfactory or not.

¹Airbus data from www.airbus.com/aircraft/support-services/airport-operations-and-technical-data/aircraft-characteristics.html. Boeing and Douglas data from www.boeing.com/commercial/airports/plan_manuals.page

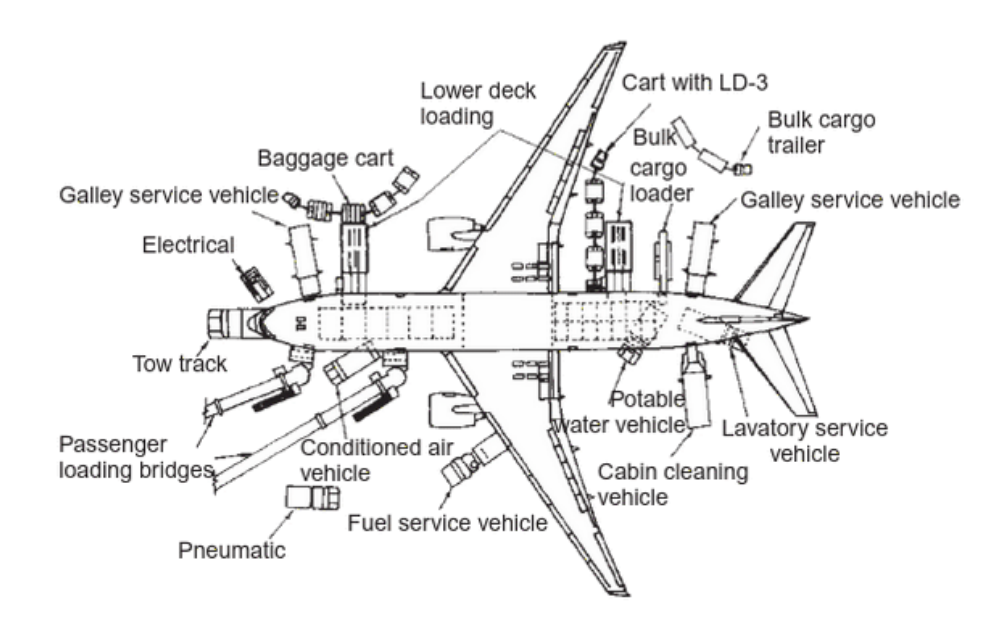


Figure 2.4: Ground handling equipment required for a Boeing 777 [25]

Aircraft	Door sill height (m)	Airframe lower surface height (m)
Douglas DC-8	3.2	2.2
Boeing 747	4.7	1.8
Douglas DC-10	4.8	2.3
Airbus A330	5.0	2.3
Boeing 777	5.3	3.0
Airbus A380 (main deck)	5.3	2.3
Airbus A350	5.3	2.5

Table 2.1: Door and airframe height for different aircraft

Gear design and analysis process

The design and analysis processes discussed in previous chapter were all made to be used with an optimiser to obtain the best gear. This was possible because they were used on conventional configurations on which the interactions between gear and airframe were known, even if not always taken into account: Van Oene [18] points that neglecting gear-wing interaction led to Heerens [19] algorithm failure in multiple cases.

However the interactions between gear and airframe on the Flying V are not known since it is the goal of this work to investigate them. Therefore including an optimiser in the design method is risking ending up in a situation similar to Heerens with no feasible gear, just because some interactions were neglected. Therefore no optimiser is used in this work to allow uncovering the interactions.

All the geometry in this section is performed in the standard aircraft reference frame: x-axis pointing to aircraft nose, z-axis pointing downward, and y-axis completing the frame toward the right wing. The origin point from the ParaPy model is used, located at the aircraft nose. Pitching moment coefficient is thus positive for nose-up, and forces coefficients are positive if the force acts in the direction of the axis.

3.1. Overall architecture of the process

The overall architecture of the process is visible in Figure 3.1. It starts from the existing Flying V airframe definition, on which an exploratory study is conducted. The goal of this exploratory study is to get a feeling of the main interactions between gear and airframe, such as the pitch and roll angles allowed for a given gear, or the definitely infeasible positions. The exploratory study is further detailed in 3.2. Using the exploratory study results, the airframe used for gear design is defined more precisely (more details on that in 5.2). Then the gear is designed and analysed to provide relevant figures of merit such as those discussed in 2.2. The design method is inspired by the design methods of Heerens and Van Oene, but takes into account the absence of optimisation and some interactions uncovered in the exploratory study. It is further detailed in 3.4. The design and analysis method provides a gear design and figures of merit which are then discussed to uncover the other gear-airframe interactions.

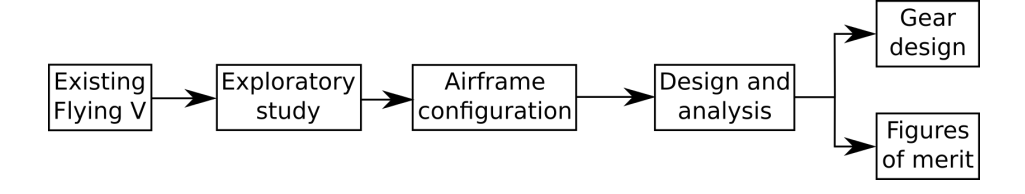


Figure 3.1: Flow chart of the process overall architecture

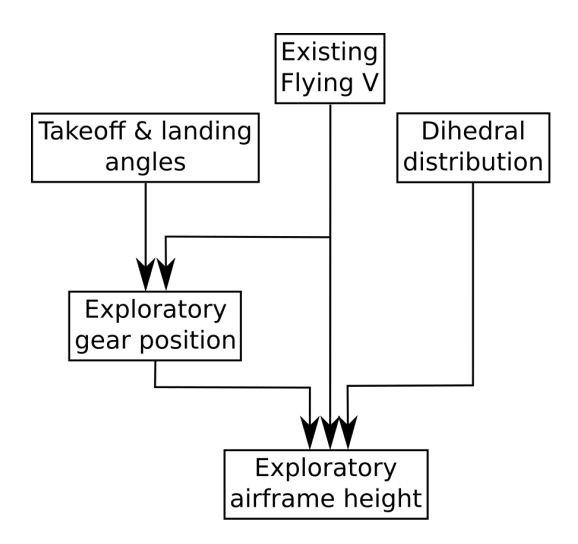


Figure 3.2: Flow chart of exploratory study

3.2. Exploratory study

The objective of the exploratory study is to try multiple options for gear positioning, and see how they interact with the airframe. Its architecture is presented in Figure 3.2. The diagram shows only one iteration, but in an exploration phase several iterations are made to try different options. The airframe centre of gravity and the take-off and landing pitch angles limit the gear position to avoid longitudinal tipover, i.e. having the gear in front of the centre of gravity. Based on this criterion and the airframe geometry, a gear position is chosen. Since the gear has to prevent the airframe from scraping the ground in normal operation, the required height of the gear position can be determined. The gear length itself is not determined as it depends on more parameters such as tire chosen, shock absorber or strut orientation, for which no design decision is made yet.

3.2.1. Comparison with literature

The structure of this study reuse steps 3 to 6 of Heerens method (see Figure 2.2). Heerens' step 1 is the nose positioning, left out here for the reason pointed in 2.1.2: nose gear is placed using loads. Computing nose gear loads requires the main gear position (see 3.10.2), thus it makes more sense to position it after the main gear as the main gear has other constraints on position. Heerens' step 2 is the choice of wheel number and of tires used, neglected here since Heerens and Van Oene make them to depend only on aircraft weight (see 3.5.2), which is not expected to vary significantly between the different gear tried.

The other difference with Heerens method is the inclusion of dihedral angle variation. It is used to investigate the interaction between wing tips and gear design, and is discussed in more details in 3.2.4.

3.2.2. Take-off and landing angles

Regulation imposes margins with stall speed during take-off and approach [26, 27]. Assuming a $0.05v_{s1a}$ deceleration from approach to impact (thrust reduction), this translates easily to limitations on take-off and landing lift coefficients:

$$C_{\text{L,lof}} = \frac{C_{\text{L,max}}}{1.13^2}$$
 (3.1)
 $C_{\text{L,ldg}} = \frac{C_{\text{L,max}}}{1.18^2}$ (3.2)

$$C_{\text{L,ldg}} = \frac{C_{\text{L,max}}}{1.18^2} \tag{3.2}$$

which determines the incidence through the aircraft lift curve.

In addition to take-off speed, the aircraft needs to climb after leaving the ground, even in one

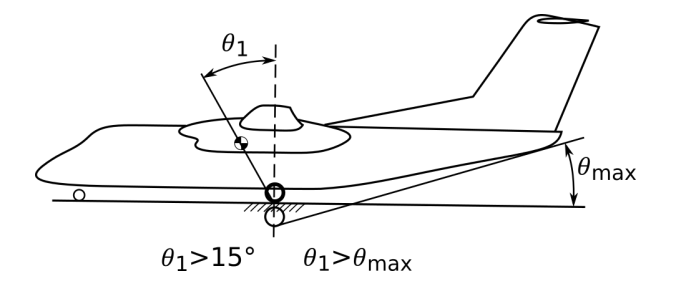


Figure 3.3: Gear position constrained by longitudinal tipover [13]

engine inoperative (OEI) condition. The flight path angle in climb can be estimated by:

$$\sin \gamma = \frac{T}{m_{\text{AC,to}} \,\mathrm{g}} - \frac{1}{\frac{L}{D}} \tag{3.3}$$

derived from [28]. Lift-to-drag ratio usually decreases at high incidence, while OEI condition decreases thrust-to-weight ratio. As such, the take-off incidence obtained from free air lift curve can lead to a too low lift-to-drag ratio thus requiring to lower the incidence to obtain a higher lift-to-drag ratio.

In addition to pitch angle, roll angle needs to be accounted for, to allow for cross-wind conditions. Regulation do not specify roll angle values, but cross-wind speeds that the aircraft must accommodate. Deriving a roll angle from these wind speed would require a Flying V dynamic simulation, for which data is not available. It must thus be approximated, with two options available: Heerens[19] choice based on Raymer[11], or Van Oene[18] choice based on Torenbeek[12].

3.2.3. Exploratory gear position

In the exploratory study, only longitudinal tipover is considered, determining the longitudinal position. Lateral and vertical positions are arbitrarily decided by the user, allowing more exploration. The lateral position link with lateral turnover is neglected for now, based on the fact that specific gear design can allow to deal with theoretically insufficient lateral turnover stability [12, 15]. The gear position is limited by longitudinal tipover as shown in Figure 3.3, with θ_{max} at least equal to the highest angle between required take-off and landing angles.

The centre of gravity position required is the most aft [13], but is not available since Van der Schaft [4] could not size the structure. It is derived from the aerodynamic centre position computed by Faggiano [2, 3], by adding a stability margin in front of it.

3.2.4. Dihedral effect on airframe

As visible on Figure 3.3, the maximum reachable angle θ_{max} depends on the first point to touch the ground, and of the gear length and position, which is why extended gear is considered on the figure. It can be easily verified that the Flying V first point to touch the ground will be the wing tip, thus its position interacts with the gear design to provide sufficient pitch angle for take-off and landing. It can be checked in [2] that while planform is optimised, dihedral is completely left aside and ends up being the only available parameter that can move the wing tip. Due to the presence of the fuselage on the inboard part of the airframe, the Flying V displays dihedral only outboard of the trailing edge kink, as shown on Figure 3.4 with the effect of varying dihedral on wing tip position. When dihedral is modified, the twist angle determined by Faggiano is kept the same. These angles are already implemented in the ParaPy model of the Flying V, thus can easily be modified and the airframe updated.

3.2.5. Exploratory airframe height

If placed at a given height from the ground, the airframe will be able to pitch and/or roll until a particular angle before the wing tip touches the ground. This angle is only dependent from the airframe height, and not from the gear itself that, whichever design it has, just needs to guarantee this height. This avoid making design decisions or assumptions on the gear, which is convenient in an exploratory study to keep it as generic as possible. The required height to reach desired pitch and roll angles is computed

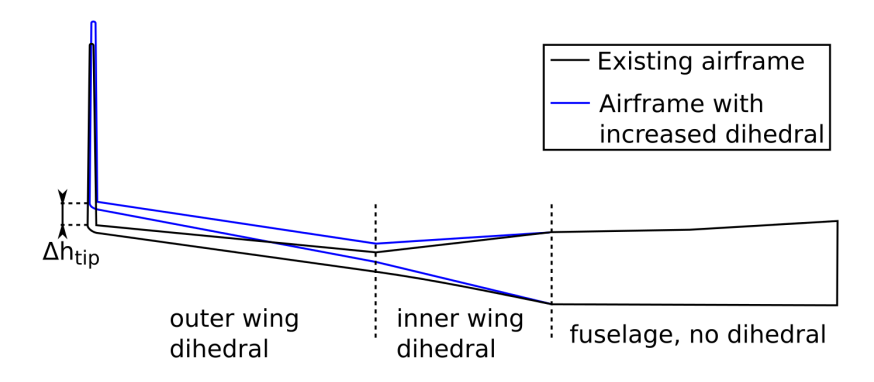


Figure 3.4: Dihedral distribution over span, and effect on wing tip height

as follows:

$$h_{\rm req} = -(x_{\rm mlg} - x_{\rm tip})\sin\theta_{\rm AC} + (y_{\rm mlg} - y_{\rm tip})\cos\theta_{\rm AC}\sin\phi_{\rm AC} + (z_{\rm mlg} - z_{\rm tip})\cos\theta_{\rm AC}\cos\phi_{\rm AC} + h_{\rm tip} \tag{3.4}$$

3.3. Stability derivatives

Modifying the dihedral not only has an influence on the gear length: the airframe modification changes the way it behaves, which can be characterised by the stability derivatives. Since dihedral is modified, one thinks immediately of the so-called dihedral effect, which is part of the sideslip related lateral stability derivatives defining the reaction of the aircraft to sideslip variation. The reaction of aircraft to sideslip is particularly important close to the ground for cross-wind operations, however dihedral likely influences the other stability derivatives.

According to ESDU AERO A.06.01.00 [29] and A.07.01.00 [30], respectively treating of the rolling moment derivatives coverage in ESDU and of the yawing moment and sideforce derivatives coverage in ESDU, the sideslip derivatives are the most important lateral derivatives. With ESDU items being extensively supported by experimental data, this assertion was considered true, and used to reduce the number of derivatives studied to only sideslip derivatives, which include the so-called dihedral effect.

3.3.1. Computation method

Stability derivatives can be computed from the results of CFD computation, and with the vortex lattice method (VLM) AVL already implemented in the ParaPy model of the Flying V, the issue could have been solved easily. However VLM appears to not be very accurate on lateral stability derivatives [31, 32]. Higher order methods such as 3D panel methods could improve accuracy with constrained computation time, but required validation data on a similar configuration to adjust the computation. The Flying V existing wind tunnel tests or CFD simulations could not be used because the setup (see [8–10]) only allowed for longitudinal characteristics study. This left only RANS simulation for validation, and since the existing RANS simulations on the Flying V considered only longitudinal aspect, new simulations were required. The time to obtain lateral stability derivatives through this method with sufficient confidence about the results was considered too high to fit in this study, and simulations were discarded.

This left only the lowest order methods available: empirical methods. ESDU [33] is one of the most known methods, but others with more limited applicability can be found [34, 35]. Empirical methods are statistically derived from existing aircraft, which have a configuration very different from the Flying V, thus their accuracy is not expected to be very good. However they are relatively quick to implement and ESDU has a modular structure which allows to adjust and use only the formulas applicable to the Flying V.

The stability derivatives due to sideslip in ESDU are defined as Y_v , L_v , and N_v respectively for sideforce, rolling moment and yawing moment derivatives. They represent the same coefficients as the usual $C_{Y,\beta}$, $C_{l,\beta}$, and $C_{n,\beta}$, but with a sideslip angle in radians instead of degrees.

3.3.2. Equivalent wing

The equivalent wing planform of the Flying V wing is required to use the different ESDU formulas, since the Flying V does not have a straight tapered wing which is required by the different ESDU formulas.

The computation method is detailed in Annex A of ESDU 76003[36] and applied identically to the Flying V

3.3.3. Sideforce derivative due to sideslip Y_n

It is divided in four components, of which the flaps component is neglected as the Flying V has no high-lift devices. The components are then added to provide the derivative.

Wing-body component The ESDU formula requires a separate fuselage in addition to the wing [37]. Two options are considered to solve the absence of separate fuselage on the Flying V, with a choice made through validation:

• "ESDU+T&Q": it mixes ESDU with Toll and Queijo work [34] which focused on swept wings of taper ratio 1 without fuselage. The Toll and Queijo formula [34] for Y_v is added to the dihedral component that remains in ESDU formula with no fuselage:

$$Y_{\nu,\text{wing-body}} = C_{L}^{2} \frac{6 \tan \Lambda_{1/4} \sin \Lambda_{1/4}}{\pi A \left(A + 4 \cos \Lambda_{1/4} \right)} - 0.006 |\Gamma|$$
 (3.5)

with Γ a weighted average using the span fractions as weights.

• "ESDU fake body" defines a fake fuselage using a span fraction around aircraft midline, and applies the ESDU formulas from [37] using that fake fuselage.

Nacelles component The ESDU formula covers the typical airliner configuration with nacelles below and in front of the wing. However the formula is independent of nacelle position w.r.t. wing, thus no modifications were considered necessary to the formula from ESDU [37].

Fin component ESDU offers three different situations for fin influence: single fin attached to the fuselage, twin fins attached to the fuselage or twin fins attached to the horizontal tailplane tips. The last one is too limited geometrically, and the second one include the interaction between the fins, which is not expected to be significant on the Flying V since the fins are far apart. This leaves only the single fin formula from [38], which is adapted by considering the Flying V fins are independent (thus their contribution can be summed). The ESDU formula introduces scaling parameters for wing, fuselage and tail, but none of the methods to obtain these coefficients match the Flying V. Therefore a single scaling coefficient J_W is kept, to be adjusted through validation. The component is computed as follows:

$$Y_{\nu,\text{fin}} = -J_{\text{W}} \left(C_{\text{L},\alpha} \right)_{\text{fin}} \frac{2S_{\text{fin}}}{S_{\text{ref}}}$$
(3.6)

with $(C_{L,\alpha})_{fin}$ obtained graphically in [39].

3.3.4. Rolling moment derivative due to sideslip L_v

It is divided in seven components, of which flaps, body and wing-body interference components are neglected as the Flying V has no high-lift devices and no body. The components are then added to provide the derivative.

Dihedral component The ESDU formula applies to the Flying V equivalent wing. It is computed for the Flying V compound dihedral wing as [40]:

$$L_{v,\Gamma,\text{total}} = L_{v,\Gamma_{inner},[0,\text{outer kink}]} - L_{v,\Gamma_{inner},[0,\text{inner kink}]} + L_{v,\Gamma_{outer},full} - L_{v,\Gamma_{outer},[0,\text{outer kink}]}$$
(3.7)

with each $L_{\nu,\Gamma}$ interpolated from graphs in [40, 41], using 2D inviscid properties from [42]. The interpolation degree is decided from the examples shown in [40, 41]: linear for full-span, similar to second order for part-span.

Wing planform component The ESDU formula [43] applies to the Flying V, being simply a linear function of the lift coefficient.

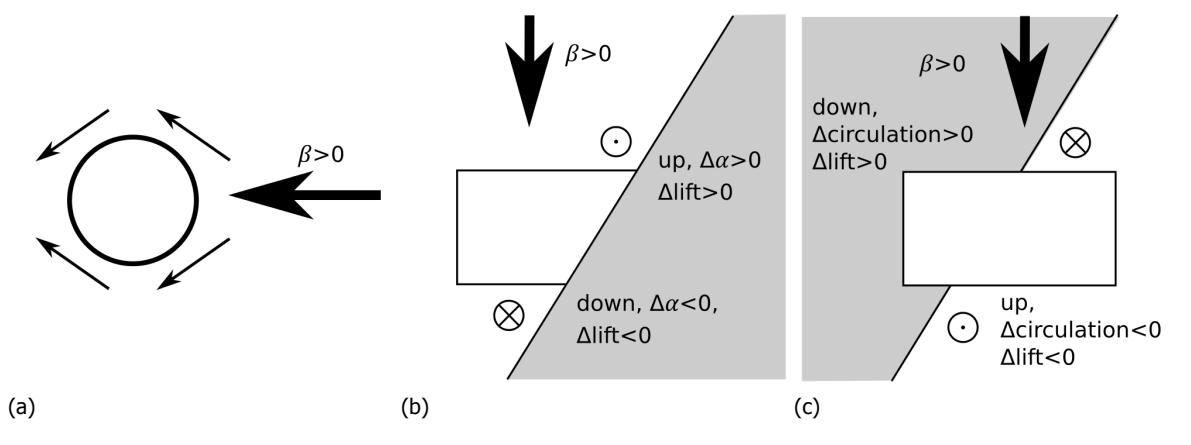


Figure 3.5: Antisymmetric effect on the wing due to (a) lateral flow over the nacelle alone, for (b) nacelle in front and below of the wing and (c) nacelle aft and above the wing

Nacelles component ESDU formula still considers nacelle below and in front of the wing [44]. This time the nacelle position w.r.t. wing creates an antisymmetric effect responsible for the nacelle component. Following the reasoning in Figure 3.5 it is concluded that the antisymmetric effect of a nacelle aft and above the wing (in Figure 3.5c) is similar to a nacelle below and in front of the wing (in Figure 3.5b). Thus the formula from [44] is used.

Fin component The ESDU formula [38] is simply converting Equation 3.6 to rolling moment, thus is applicable to the Flying V.

3.3.5. Yawing moment derivative due to sideslip N_{ν}

It is divided in the same components as Y_{ν} . The components are then added to provide the derivative.

Wing-body component The ESDU formula has the same requirements as for $Y_{v,wing-body}$, thus the same options are considered, with a choice made through validation:

"ESDU+T&Q":

$$N_{\nu,\text{wing-body}} = C_{L}^{2} \left[\frac{1}{4\pi A} - \frac{\tan \Lambda_{1/4}}{\pi A (A + 4\cos \Lambda_{1/4})} \left(\cos \Lambda_{1/4} - \frac{A}{2} - \frac{A^{2}}{8\cos \Lambda_{1/4}} \right) + 6 \frac{(x_{\text{ac}} - x_{\text{cg}})\sin \Lambda_{1/4}}{b} \right] - \frac{0.006 x_{\text{cg}}}{b} |\Gamma|$$
(3.8)

with Γ as for $Y_{v,wing-body}$.

• "ESDU fake body" with the formula from [37] and the same fake fuselage as for Y_{ν} .

Nacelles component The ESDU formula [37] is independent of the nacelle position w.r.t. the wing, thus can be used without modifications.

Fin component As for the rolling moment derivative, the ESDU formula [38] is simply converting Equation 3.6 to yawing moment. It is therefore used on the Flying V.

3.4. Design and analysis

Using the outcome of the exploratory study, the design and analysis section aims at creating a preliminary gear design, to allow later computing of the relevant figures of merit used to compare it with other gear. The design and analysis process is presented in Figure 3.6.

Based on the literature (see 2.2) and the outcome of the exploratory study (see 5.2), the following figures of merit are evaluated:

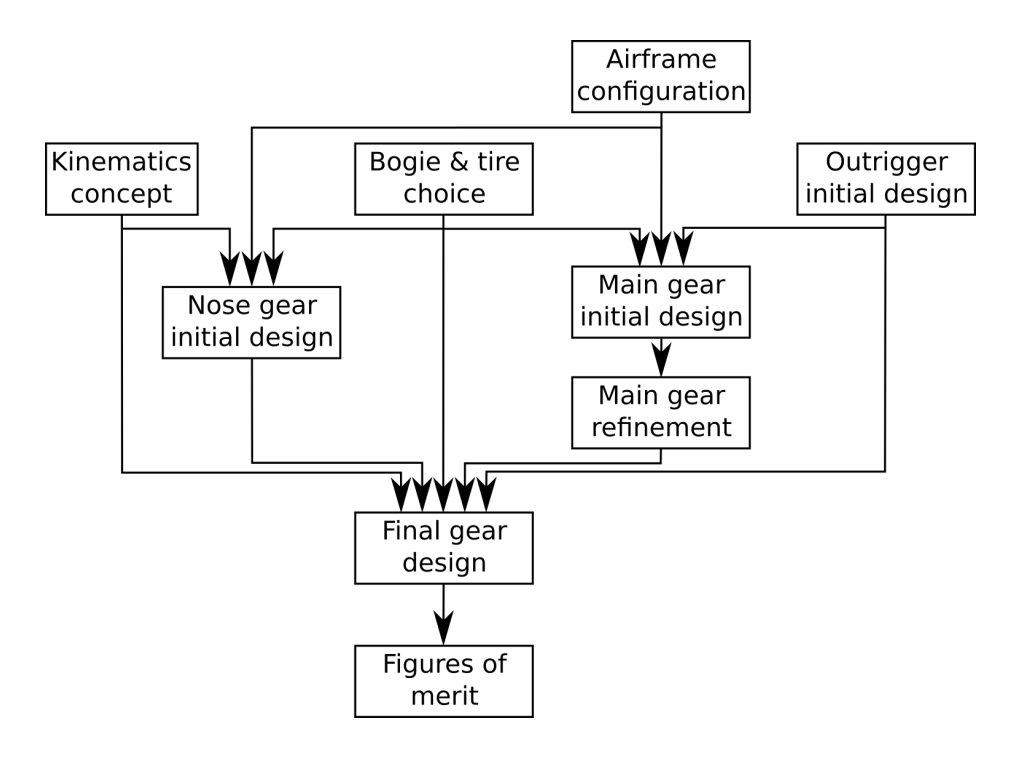


Figure 3.6: Flow chart of gear design and analysis process

- · Gear weight.
- Ground manoeuvring.
- Cabin floor height, to assess the ability to use the ground support equipment.
- Rotation ability.
- Fairing drag, if a fairing is required.
- Lateral stability derivatives, to assess the aerodynamic effect of dihedral variation (see 3.3 and 5.2).

Flotation is not considered because of the suggestion of Currey to reuse the bogie of an existing aircraft of similar weight and mission. While this prevents from having an accurate flotation value, such value would be hard to evaluate with precision since the aircraft mass is not fully defined. Thus the approximation was favoured, and flotation was taken out of the figures of merit.

3.4.1. Comparison with literature

Compared to the methods from literature, particularly Heerens and Van Oene who use a linear process, not all steps are ordered w.r.t. each other. Instead some steps are presented at the same level, and can be performed in any order provided that their inputs are available. This allows to modify one of these steps without wondering if the other steps need to be recomputed, a particularly useful feature when the interactions between gear and airframe are not known and can create unexpected situations, or simply if one wants to modify only part of the gear.

Compared to Heerens, the nose gear positioning is moved later, because its initial design requires to know the tire choice (more details in 3.9). A noticeable addition is the outrigger design, which was added following the exploratory study (more details in 3.6). The succession of initial design for each component, and then combining them all in a final design is inspired by Van Oene who allows the wing to move between the two steps. Such airframe modification does not happen here, and the succession of the two is used to adjust the gear characteristics after performing checks that need a preliminary design of all gear, a task delegated to the optimiser in Van Oene work.

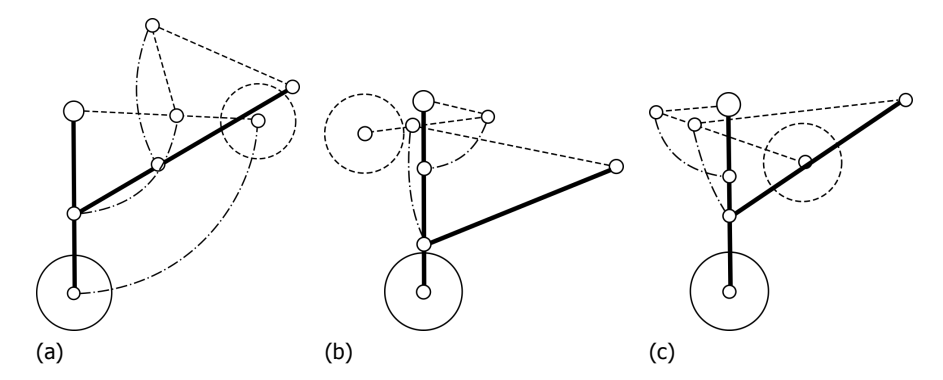


Figure 3.7: Examples of simple landing gear kinematics [15]

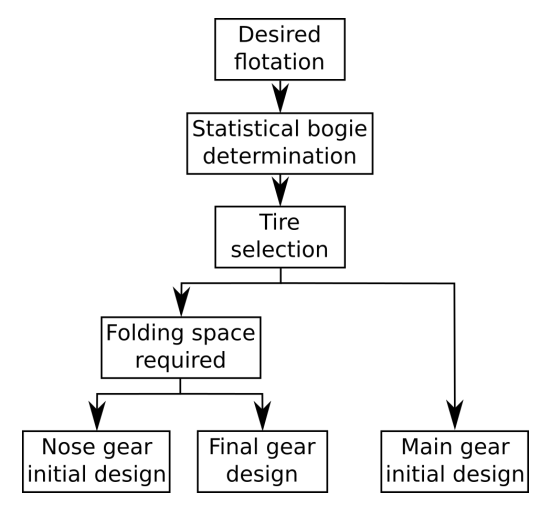


Figure 3.8: Flow chart of bogie and tire choice

As it does not include an optimiser, this process does not aim at creating the best gear possible, but only a feasible gear. Some values can be chosen early in the process, and are not modified because they did not lead the gear to fail the different checks performed, while they could have improved some aspect if they were changed.

3.4.2. Kinematics concept

Similarly to Van Oene, who adjusts the gear design depending on its position using predefined kinematics, here a kinematic concept is chosen early and used on the design. It could have been simply included inside final gear design, but the Flying V airframe led to use this concept when creating the nose gear initial design (more details in 3.9), thus it was taken out as a separate component.

According to [15], the simplest kinematics are also the most reliable and often the lightest and cheapest, thus they should be prioritized and deviations should be given careful thought. Examples of simple kinematics are shown in Figure 3.7. For example, the kinematic concept of Figure 3.7a is used for nose gear and main gear of current airliners, with the wheel direction changed for main gear. This shows that the concepts on Figure 3.7 are used as starting points and then precised during the design to meet the exact needs of the aircraft.

3.5. Bogie and tire choice

As did Heerens and Van Oene, the bogie is defined and the tire selected early in the process, because it does not require data from other items, and is used for nose and main gear initial design. The process to choose bogie and tire is given in Figure 3.8.

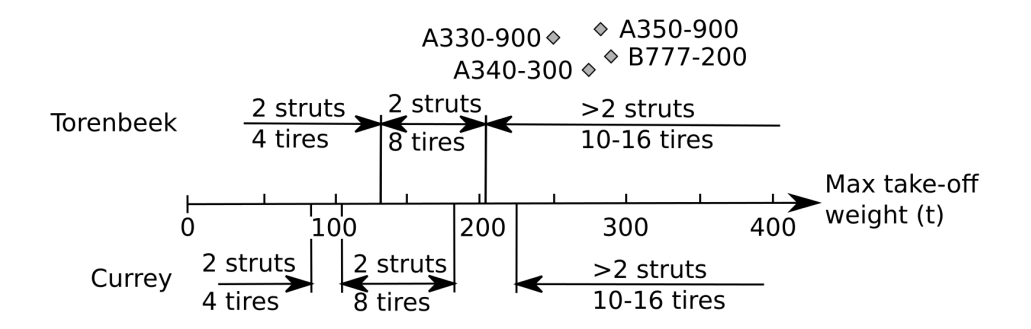


Figure 3.9: Relation between aircraft maximum take-off weight and wheel number [12, 15, 45–48]

3.5.1. Desired flotation

As explained in 2.1.1, flotation is a measure of the runway/taxiway stress created by the aircraft landing or rolling on them. It determines which runways/taxiways the aircraft can use [21], thus which airport it can operate from. Based on airports one wants the aircraft to access, a desired flotation can be determined, which the bogie design will aim to satisfy. This desired flotation can be achieved by actually checking the airport technical data to derive a flotation value, or by aiming for a similar flotation to an existing aircraft [15].

3.5.2. Relation between weight and wheel number

It is shown on Figure 3.9 that for Torenbeek [12] and Currey [15] the number of wheels in an aircraft main landing gear can be related to the aircraft maximum take-off weight. While they do not fully agree on the design to chose for lower weights, they state that a gear for an aircraft heavier than 225 t, should have more than 2 struts with 10 to 16 wheels in total.

Four existing aircraft of maximum take-off weight around 270 t tell otherwise. Except for the A340-300 three struts, all others have only two struts, and only the A340-300 and B777-200 have more than 8 wheels. The A340-300 is contemporary to Currey's and Torenbeek books, thus it seems logical that it complies with it. All other are more recent, and suggest that Currey and Torenbeek ranges are out of date. Therefore it seems more reliable to derive the Flying V wheel number from these existing aircraft than from Currey and Torenbeek.

3.5.3. Tire selection

Based on bogie wheel number, tires can be found to support the required loads on each wheel. The tire load can be estimated by dividing the strut load by the number of wheels, adding a 7 % margin for approximations [12] and 25 % margin for future gross weight increase [13, 15]. Since the gear are not yet positioned, the strut load are not known precisely. According to Currey, they can be approximated by assuming the main gear support 90 % of aircraft weight, and using maximum take-off weight as sizing case. Current aircraft suggest a main gear static load closer to 95 % of total weight [47–49]. For nose gear, braking case is limiting since it will increase the load on nose gear. The load increase can be about twofold compared to static case, depending on the exact gear setup.

It is strongly advised [12, 13, 15] to look for existing tires (for example in [50, 51]) to use reliable tire properties when designing the rest of the gear.

3.5.4. Folding space required

After take-off, the gear is folded within the airframe, with sufficient space in the wheel well to accommodate the bogie. Indeed, in addition to the dimensions due to the geometric layout and tire dimensions, margins with the structure are required to avoid the tire getting damaged by contacting a structural element:

Lateral margin =
$$0.015w_{\text{tire}}$$
 (3.9)

Radial margin =
$$0.03(R_{\text{tire}} - R_{\text{wheel}})$$
 (3.10)

Moreover the take-off run leads to tire growth due to centrifugal forces and tire heating [12], requiring larger margins. The minimum clearance to account for that effect is obtained from Figure 3.10. Take-off

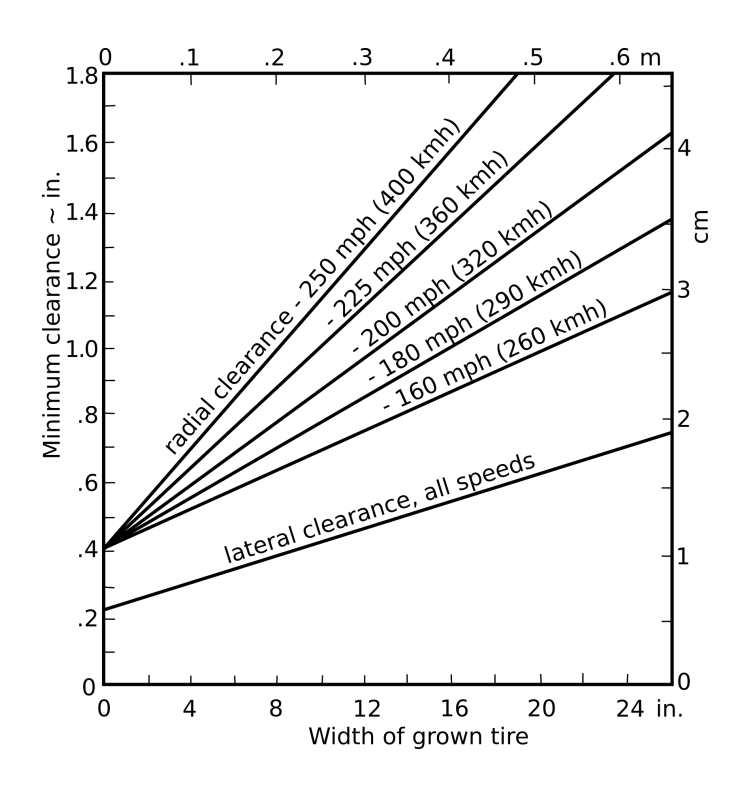


Figure 3.10: Minimum margin between tires and aircraft parts based on tire size and rotation speed [12]

speed is required for radial margin, and can be estimated with:

$$v_{\rm lof} = \sqrt{\frac{m_{\rm AC,to} g}{0.5 \rho_{\rm air,MSL} S_{\rm ref} C_{\rm L,lof}}}$$
(3.11)

By adding the two margins to the geometric layout, the space required to accommodate the folded gear can be computed, allowing to determine where the gear can fold.

3.6. Outrigger initial design

Considering the Flying V airframe geometry, the first point to touch the ground when pitching or rolling will be the wing tip (see Figure 1.2a). Because the fins are attached to the wing tip, a wing tip ground strike can have more important consequences than on conventional aircraft, therefore it must be avoided even more. This led to consider an outrigger to ensure a wing tip ground clearance within the normal operating conditions. The flow chart of outrigger initial design is shown on Figure 3.11.

3.6.1. Desired ground margin

This is the minimum ground margin the designer wants to keep in normal operations. It can allow for airframe flexibility (which has not been studied since structure has not been sized) or pilot imprecision. This margin is the design objective of the outrigger.

3.6.2. Outrigger position and length

To position the outrigger and determine its length from the objective, design cases must be defined. As already mentioned, the wing tip will touch the ground first, whether the aircraft is pitching up, rolling or a combination of both. Pure roll is not an operational case with a gear touching the ground: roll appears with crosswind take-off or landing, thus the aircraft will be pitched up as well. The design cases are thus:

• Combined pitch and roll, for cross-wind. The outrigger should guarantee wing tip ground margin at maximum pitch and roll angles in normal operation.

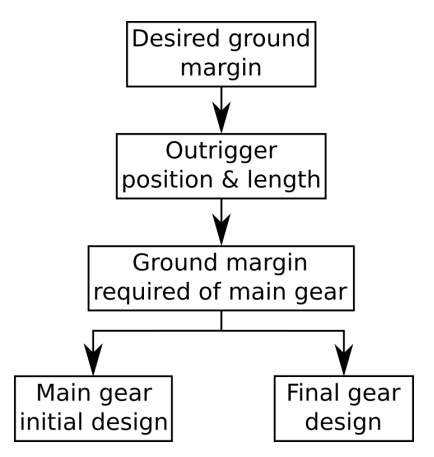


Figure 3.11: Flow chart of outrigger initial design

• Pure pitch, for over-rotation. The outrigger should allow sufficient pitch angle for take-off before touching the ground, and guarantee wing tip ground margin once touching the ground.

Outrigger position

To allow for optimal load support, the outrigger should touch the ground on the runway. While this varies with the actual position of the aircraft on the runway, aircraft are supposed to be approximately at the centre of the runway. Runways for aircraft of similar size to the Flying V are at least 45 m wide, according to regulations [52, 53]. Regulation also allows the aircraft to deviate laterally by at most 9.1 m in case of engine failure during take-off [26, 27].

The combination of these two constrains the lateral position of the outrigger to 13.4 m if it must touch ground on the runway. Around the runway is a landing strip that has some load bearing capability (defined by regulations) and could eventually support the outrigger load, allowing to lower the lateral constraint. Longitudinal position can be adjusted to meet the design cases while having a short (thus lighter, see 3.11.1) outrigger, and to offer good structural integration.

Outrigger length

From the design cases, the required height at the outrigger position can be computed with Equation 3.4. By deciding of the outrigger strut pitch angle w.r.t. airframe axes, the outrigger length can then be deduced as follows:

$$l_{\text{outrig}} = \frac{h_{\text{req}}}{\cos(\theta_{\text{AC}} - \theta_{\text{outrig}})}$$
(3.12)

It must be noted that this equation considers only a pitch angle between strut and airframe axes. This was done by analogy with airliner main gear struts, and with B-52 Stratofortress outriggers, which both are not tilted along roll direction.

A second thing to note is that the length computed is from airframe to ground such that the ground margin h_{tip} included in Equation 3.4 is satisfied. Therefore this length is with loaded tire and compressed shock absorber. No literature support was found to select the outrigger tire and size its shock absorber, and it seemed excessive to select them with the same stresses as main gear, thus it was chosen to compute the overall length instead of subcomponent values.

3.6.3. Ground margin required of main gear

The exploratory study shows that the gear required will necessarily be quite long (see 5.2). Since an outrigger was added to ensure ground clearance, it could be used to shorten the main gear. If the outrigger is ensuring the wing tip clearance under normal operating conditions, the main gear only needs to allow for required pitch angle for take-off and landing with the outrigger. This modifies the pitch and roll angles used in Equation 3.4, thus changes the required airframe height and the strut length derived from it.

Lower angles bring a shorter main gear, thus an airframe closer to the ground when parked which would make ground handling easier. An outrigger deployment failure however needs to be considered

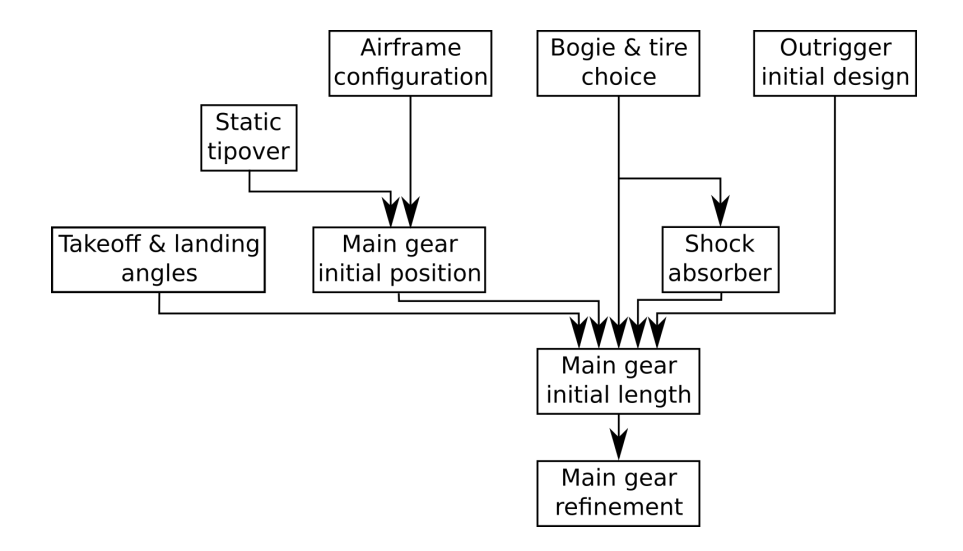


Figure 3.12: Flow chart of main gear initial design

in that case. With such modification, the outrigger would touch the ground first at high roll angles, reducing roll angle until main gear touches the ground. The airframe stress created could lead to an undesirable heavier structure, depending on the stress generated.

3.7. Main gear initial design

With the outrigger, bogie and tire defined, the main gear initial design can be performed according to the flow chart in Figure 3.12. Take-off and landing angles are obtained as detailed in 3.2.2.

3.7.1. Main gear initial position

As explained in 3.2.3, the gear position fwd limit is determined by longitudinal tipover. The positioning method described in Figure 3.3 combines three aspects:

- Static tipover: when the aircraft is at rest on the ground, the centre of gravity is in front of the gear.
- Push-back tipover: when the aircraft brakes after push-back from the airport gate, it must not tipover due to inertia. It is approximated [13, 15] by $\theta_1 > 15^\circ$ in Figure 3.3. This limit could be brought down if it is shown that no tip-over occurs during push-back with a lower limit, but without data to support it the empirical value given by Roskam and Currey is kept.
- Rotated tipover: when the aircraft rotates at its maximum pitch angle, the centre of gravity should be in front of the gear. It is represented by $\theta_1 > \theta_{\rm max}$ in Figure 3.3.

The last two push the gear backward with an increased effect for long gear and high required incidence, which is the case of the Flying V. It was thus decided to analyse them in more detail (see 3.8) based on an initial design, therefore only static tipover is considered to position the gear here.

The centre of gravity position can be obtained by any available mean. Since Van der Schaft could not evaluate it on the Flying V, it will be deduced from the aerodynamic centre of Faggiano, using a stability margin. The range can then be deduced from existing aircraft.

The gear is longitudinally positioned where static tipover is satisfied. Lateral and vertical positions are respectively constrained by an interaction with nose wheel and the kinematics requirement, thus will be updated later. For now they are left free to the designer, keeping in mind that a position closer to main structural element will lower the weight [15].

3.7.2. Shock absorber

The shock absorber is the intermediary between the bogie and the aircraft, to limit the loads supported by the airframe. Its main characteristic is the total stroke s, defined by the sizing case of absorption in

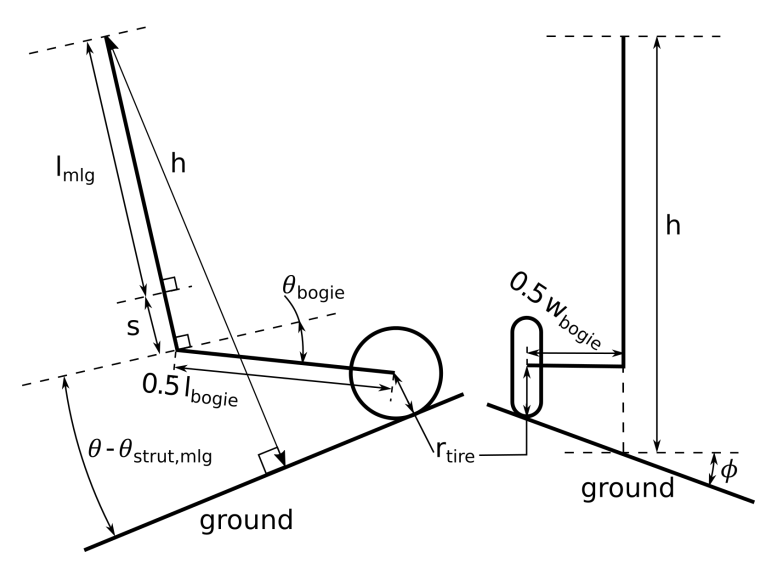


Figure 3.13: Computation of landing gear strut length

the tire and the shock absorber of the vertical kinetic energy and the potential energy of the aircraft at impact during landing [12, 15]:

$$\underline{s_t \eta_t N m_{\text{AC,ldg}} g} + \underline{s \eta_s N m_{\text{AC,ldg}} g} = \underbrace{\frac{m_{\text{AC,ldg}} v_z^2}{2}}_{\text{Kinetic energy}} + \underbrace{\frac{(m_{\text{AC,ldg}} g - L)(s + s_t)}{Potential energy}}$$
(3.13)

Regulation (CS-25, [26, 27]) allows to assume lift equal to weight ($L = m_{AC,Idg}g$), making the total stroke s to depend only on vertical speed at impact:

$$s = \frac{v_z^2}{2g} - N\eta_t s_t$$
 (3.14)

3.7.3. Main gear initial length

As for the outrigger, the main gear length is derived from the airframe required height computed from Equation 3.4, with the angle adjustments discussed in 3.6.3. Equation 3.12 could be used, however here a bogie design is available from 3.5 and a shock absorber from 3.7.2, therefore they can be accounted for when computing the gear length. The option to use an actuated tilting bogie (raising the aircraft at high incidence as on the A330¹) is considered to help reduce the static gear length. This is included in the length computation, based on the geometry shown in Figure 3.13:

$$l_{\text{mlg}} = \frac{h_{\text{req}} - R_{\text{tire}} - 0.5l_{\text{bogie}}\sin\left(\theta_{\text{bogie}} + \theta_{\text{AC}} - \theta_{\text{mlg}}\right) - 0.5w_{\text{bogie}}\tan(\phi_{\text{AC}})}{\cos\left(\theta_{\text{AC}} - \theta_{\text{mlg}}\right)} - s \tag{3.15}$$

The actuated tilting bogie option can be deactivated by setting $\theta_{bogie} = \theta_{mlg} - \theta_{AC}$ if the option is not used.

3.8. Main gear refinement

The main gear initial design provides with a first draft of the gear design, but with no certainty it is acceptable. Therefore some additional checks are performed to refine the gear design. The flow chart of this section is provided in Figure 3.14.

3.8.1. Push-back tipover

This is the second aspect of longitudinal tipover (see 3.7.1), dealing with inertia effects due to braking after push-back. This effect is accounted for in literature [12, 13, 15] by the 15° lower limit on θ_1 in

¹A330 Flight Crew Operating Manual, Volume 1 - System Description, Airbus, Unpublished

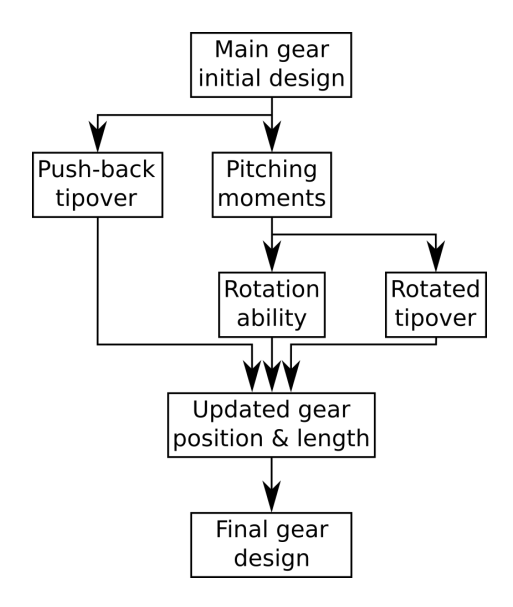


Figure 3.14: Flow chart of main gear refinement

Figure 3.3.

The axis around which the aircraft would tipover is the axis between the gear strut and the bogie which position can be computed from the gear position as follows:

$$\begin{cases} x_{\rm lrp} = x_{\rm mlg} + l_{\rm mlg} \sin \theta_{\rm mlg} \\ y_{\rm lrp} = y_{\rm mlg} \\ z_{\rm lrp} = z_{\rm mlg} - l_{\rm mlg} \cos \theta_{\rm mlg} \end{cases} \tag{3.16}$$

This assumes that the shock absorber is fully compressed at that moment, and that as for outrigger the gear strut is only tilted along pitch axis. From this equation, the gear length computed from Equation 3.15 and the centre of gravity position, one can compute the gear position required to match the push-back tipover criterion.

It is obvious that the longer the gear, the more aft it will be pushed (all other parameters constant). With the exploratory study suggesting long gear and flying wings aircraft having low pitch control moment arm, an option to loosen this constraint was investigated. A possible answer was found through the active tilting bogie: using the bogie actuator to lock it when braking after push-back could briefly move aft the point around which the aircraft tipover, to become the most aft wheel axis:

$$\begin{cases} x_{\rm lrp} &= x_{\rm mlg} + l_{\rm mlg} \sin \theta_{\rm mlg} + 0.5 l_{\rm bogie} \cos \theta_{\rm AC,rest} \\ y_{\rm lrp} &= y_{\rm mlg} \\ z_{\rm lrp} &= z_{\rm mlg} - l_{\rm mlg} \cos \theta_{\rm mlg} + 0.5 l_{\rm bogie} \sin \theta_{\rm AC,rest} \end{cases}$$
(3.17)

This would allow to move the gear forward while satisfying push-back stability constraint.

3.8.2. Pitching moment

As already mentioned several time, rotation ability is a concern for flying wing aircraft. With no available dynamics of the aircraft on the ground, it was decided to approximate it by determining if the aircraft can generate nose-up pitching moment around the longitudinal rotation point. The total pitching moment in the aircraft reference frame can be broken down in three components:

Weight-induced pitching moment:

$$C_{\text{m,weight,lrp}} = \frac{m_{\text{AC,to}} \, \text{g} \cdot \text{moment arm}}{0.5 \rho_{\text{air}} v^2 S_{\text{ref}} \bar{c}}$$

$$\text{moment arm} = \left(x_{\text{cg}} - x_{\text{lrp}} \right) \cos \left(\theta_{\text{AC,rest}} \right) + \left(z_{\text{cg}} - z_{\text{lrp}} \right) \sin \left(\theta_{\text{AC,rest}} \right)$$
(3.18)

moment arm =
$$(x_{cg} - x_{lrp}) \cos(\theta_{AC,rest}) + (z_{cg} - z_{lrp}) \sin(\theta_{AC,rest})$$
 (3.19)

Thrust pitching moment, assuming horizontal thrust in airframe axes:

$$C_{\text{m,thrust,lrp}} = \frac{-T(z_{\text{thrust}} - z_{\text{lrp}})}{0.5\rho_{\text{air}}v^2S_{\text{ref}}\bar{c}}$$
(3.20)

Aerodynamic pitching moment, using the model from Ruiz-Garcia[10]:

$$C_{\text{m,aero,lrp}} = C_{\text{m,aero},\bar{c}/4} + \frac{1}{\bar{c}} \left(\left(x_{\bar{c}/4} - x_{\text{lrp}} \right) C_{z} - \left(z_{\bar{c}/4} - z_{\text{lrp}} \right) C_{x} \right)$$
(3.21)

This breakdown is specific to the Flying V as it is available currently: the aerodynamic model includes control surface deflection, flaps have no effects since the Flying V has none, and the nacelle aerodynamic effect is neglected because it was not included in the model by Ruiz-Garcia.

There is however a limit to Ruiz-Garcia aerodynamic model: it was obtained on the sub-scale model with a smaller range of deflection. To be extended for the full-scale aircraft, two separate effects needs to be accounted:

- A Reynolds number correction that increases the control surface efficiency by 20 % in all conditions. The efficiency increase is applied only to the terms related to control surface deflection in [10] model.
- A deflection correction until -30° extrapolates the forces and moment coefficients generated at higher deflection than covered by the model. The extrapolation is assumed linear until a saturation value:
 - 0.151 for vertical force coefficient of all surfaces.
 - 0.11 for moments coefficients by a single control surface. Without literature addressing interaction between surfaces, the value is conservatively kept at the polynomial model maximum allowed deflection.

No literature was found to support drag extrapolation with these effects. However it is expected to increase, and being located above the longitudinal rotation point, it should help rotation. Therefore neglecting its increase is conservative.

3.8.3. Rotation ability

Rotation ability is checked qualitatively by comparing the control surface deflection required to obtain zero pitching moment with the maximum deflection. This is tested in the most adverse case for rotation in terms of control surface deflection required: full thrust and fwd centre of gravity. The pitching moment is computed by summing all three components listed in 3.8.2. This checking method is more of an indicator than an actual verification of ability to rotate, however it avoids having to simulate the aircraft dynamics, which would make the study unnecessarily more complex.

The fwd centre of gravity position is derived from the aft centre of gravity position computed in 3.2.3 by adding the centre of gravity range. Torenbeek [12] provides a table of airliners with their centre of gravity range, which is consistently close to 20 % of mean aerodynamic chord (MAC). However the Flying V has a very large MAC compared to conventional airliner, thus keeping the same ratio would not make sense, and absolute length of the range is used.

The ability to reach zero pitching moment far from maximum deflection is checked at low incidence for initial rotation and at high incidence to ensure that pitch control is able to maintain the aircraft attitude at high pitch angle around the end of take-off.

3.8.4. Rotated tipover

This is the last part of tipover detailed in 3.7.1. Literature requires the centre of gravity to be in front of the gear even at maximum pitch angle (see Figure 3.3). At maximum pitch angle, the point around which the aircraft rotate (and at which the pitching moments need to be computed) is the following:

$$\begin{cases} x_{\rm lrp} = x_{\rm mlg} + (l_{\rm mlg} + s) \sin \theta_{\rm mlg} + 0.5 l_{\rm bogie} \cos(\theta_{\rm bogie} - \theta_{\rm mlg}) \\ y_{\rm lrp} = y_{\rm mlg} \\ z_{\rm lrp} = z_{\rm mlg} - (l_{\rm mlg} + s) \cos \theta_{\rm mlg} - 0.5 l_{\rm bogie} \sin(\theta_{\rm bogie} - \theta_{\rm mlg}) \end{cases}$$
(3.22)

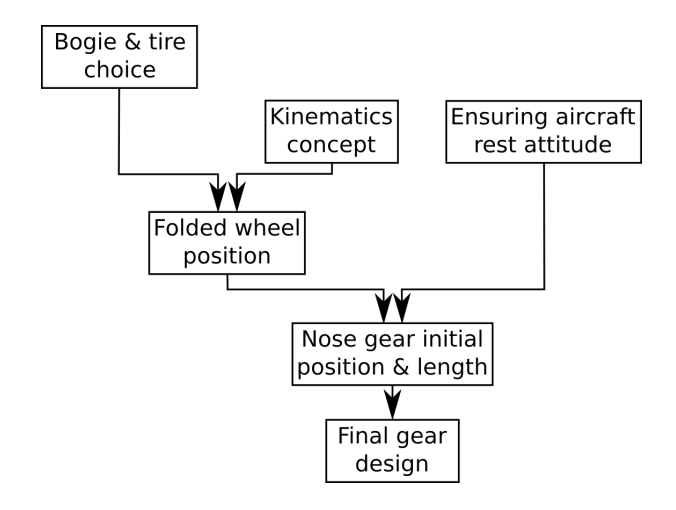


Figure 3.15: Flow chart of nose gear initial design

This assumes bogie tilted and shock absorber fully extended. Setting $\theta_{\text{bogie}} = \theta_{\text{mlg}}$ removes the effect of the actuated tilting bogie if the option is not used.

As for push-back tipover, the longer the gear, the more aft it is pushed (all other parameters constant). Thus an option to loosen this constraint was also investigated. The idea is here to use control surface to compensate a nose-up weight pitching moment at high incidence, until incidence decreases and makes the moment nose-down again. This is checked as for rotation ability: zero pitching moment must be achieved with control deflection far from maximum deflection. The test case is the most adverse case in terms of control surface deflection required: maximum pitch angle, aft centre of gravity and no thrust. The most adverse case being at maximum pitch angle, low incidences are not considered for this check.

3.8.5. Updated gear position and length

From its initial position, the gear is moved longitudinally to satisfy both push-back and rotated tipover, accounting for the modifications made to loosen the constraint they place on the gear. The lateral and vertical position will be updated later when the constraints applying on them can be computed. The new gear length can be computed from Equation 3.15. The use of ParaPy made the update quite easy as the different positioning constraint computation were implemented and just needed to be executed with the new gear position to check if it was better.

The initial main gear design and its refinement can be regrouped as one design step, if all aspects are implemented. This avoids to compute a useless initial position (since it is immediately updated). However the author felt it made the process less clear, and preferred to separate it in two components.

3.9. Nose gear initial design

Compared to Heerens, nose gear is moved later in the process because of the Flying V airframe: it is very thin with most of space in the fwd part taken by the fuselage. There is therefore very little space to fit the nose gear below the passenger cabin as it is usually done on airliners, requiring to know the space taken by the tires before positioning it. The process of nose gear initial design is shown in Figure 3.15.

3.9.1. Folded wheel position

Based on the tire chosen to support the load, the required stowage space can be computed using the margins from 3.5.4. The simplest kinematics concept for nose gear is forward folding, used on most existing airliners. The limited space available in the Flying V leads to first choose a position for the wheel before placing the gear itself.

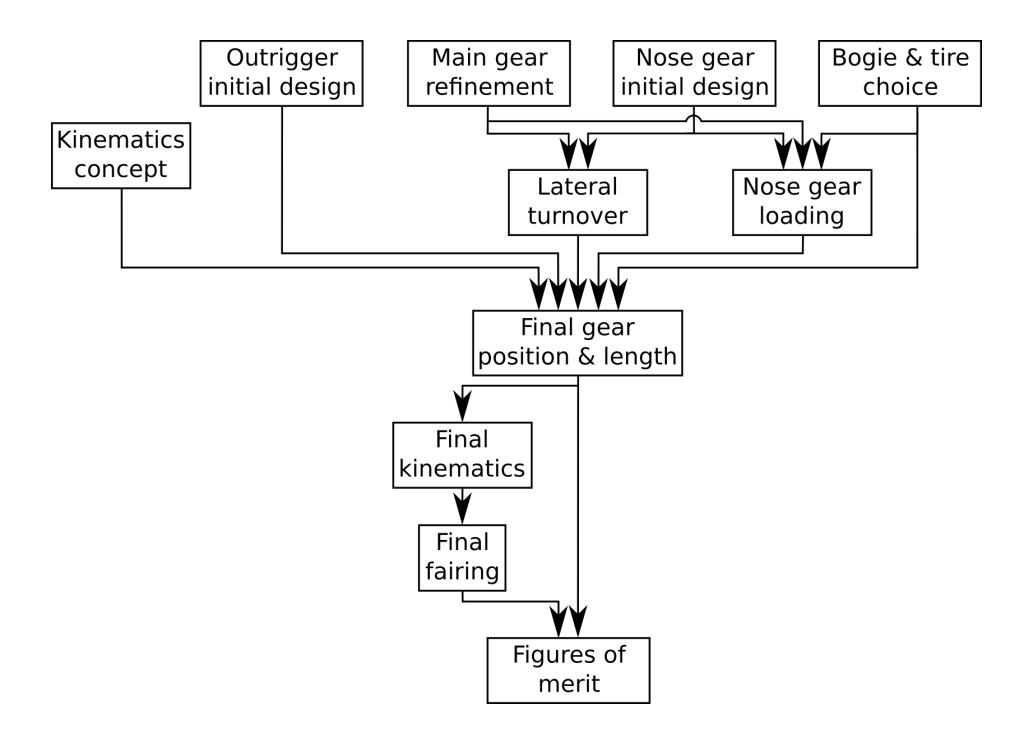


Figure 3.16: Flow chart of final gear design

3.9.2. Aircraft rest attitude

The nose gear is such that it guarantees the desired aircraft rest pitch angle when on the ground. Values close to zero are advised [15] to avoid the feeling of climbing or descending the aisle for the passengers.

3.9.3. Nose gear initial position and length

The gear length must satisfy the desired aircraft rest attitude. It is linked to the gear position as follows:

$$l_{\text{nlg}} = \frac{l_{\text{mlg}} \cos \left(\theta_{\text{mlg}} - \theta_{\text{AC,rest}}\right) + R_{\text{tire}} - \left(x_{\text{mlg}} - x_{\text{nlg}}\right) \sin(|\theta_{\text{AC,rest}}|)}{\cos(\theta_{\text{nlg}} - \theta_{\text{AC,rest}})} + z_{\text{nlg}} - z_{\text{mlg}}$$
(3.23)

The chosen folded gear position is obviously linked with the gear position and its length:

$$x_{\text{nlg,wheel,folded}} = x_{\text{nlg}} + l_{\text{nlg}}$$
 (3.24)

providing the second equation of the system which can be solved for x_{nlg} and l_{nlg} . z_{nlg} is left to the designer choice, ideally inside the airframe but below the cabin floor.

Equation 3.23 neglects the nose shock absorber stroke. According to Currey, it can be sized based on nose gear braking load, which are not available at this point of the design process. The exact folding angle of the nose gear is neglected in Equation 3.24 to ensure that the wheel keeps clear of the vertical plane at $x_{\text{plg wheel folded}}$, and to avoid introducing an additional unknown.

3.10. Final gear design

With all parts of the gear designed separately, the gear is almost finished. It only remains to make the parts interact to perform some checks, and the final gear design can be determined. It is reminded that the outcome of this step is not guaranteed to be the best design, but only a feasible design if all constraints are satisfied. The process of this final design step is detailed in Figure 3.16.

3.10.1. Lateral turnover

Lateral turnover is the equivalent of longitudinal tipover but considering lateral inertia as well. If the ground intersection of the weight force accounting for lateral and longitudinal inertia effects is outside

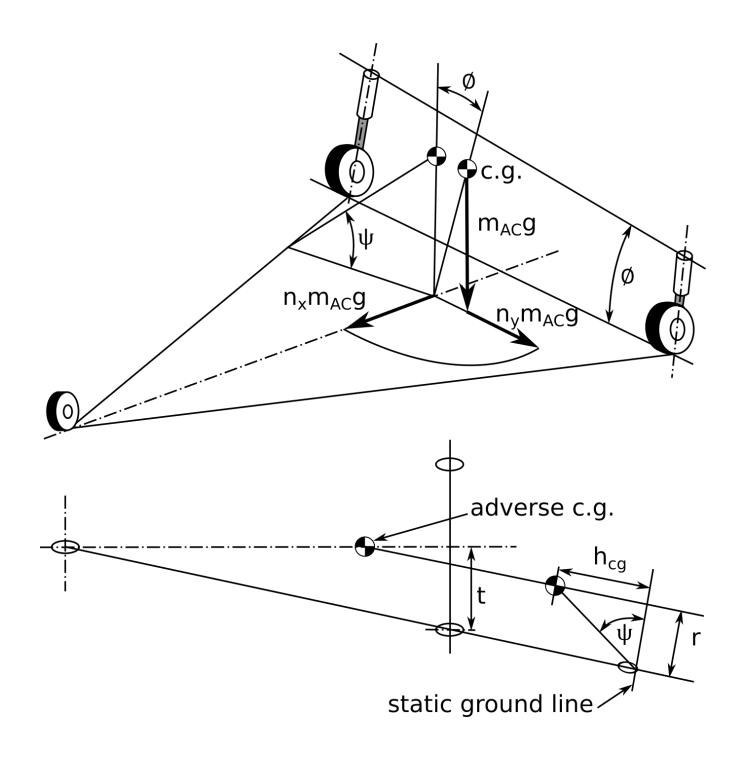


Figure 3.17: The lateral turnover angle and associated inertia effects[12]

of the triangle defined by the main gear struts and the nose gear, the landing gear cannot oppose this force and the aircraft tip over laterally. The aircraft operation type (airliner, military, carrier-based,...) determines the required lateral inertia to withstand to avoid lateral turnover.

This limit is checked using the turnover angle ψ on Figure 3.17, on which a limit is set depending on the aircraft type of operation.

$$\psi = \arctan\left(\frac{h_{\rm cg}}{a}\right) \tag{3.25}$$

$$a = (x_{\text{cg,fwd}} - x_{\text{nlg}}) \sin \left(\arctan \left(\frac{y_{\text{mlg}}}{x_{\text{mlg}} - x_{\text{nlg}}} \right) \right)$$
 (3.26)

Turnover angle determines most inboard main gear position for given nose gear position, or most aft nose gear position for given main gear position. Thus to decrease turnover angle, one can move the nose and main gear further apart longitudinally, or move the main gear outboard.

3.10.2. Nose gear loading

Nose gear load is needed in two cases:

- In the static case, where it must guarantee sufficient adherence with the ground to steer the aircraft. The static load is computed with Equation 3.27.
- In the dynamic case, where it must be below the tire allowed dynamic load. The dynamic load is computed in Equation 3.28 from Torenbeek [12]. This is also the sizing case for nose gear shock absorber.

$$F_{\text{stat}} = m_{\text{AC,to}} \frac{l_{\text{m}}}{l_{\text{n}} + l_{\text{m}}}$$

$$F_{\text{dyn}} = m_{\text{AC,to}} \frac{l_{\text{m}} + 0.45h_{\text{cg}}}{l_{\text{n}} + l_{\text{m}}}$$
(3.27)

$$F_{\rm dyn} = m_{\rm AC,to} \frac{l_{\rm m} + 0.45 h_{\rm cg}}{l_{\rm n} + l_{\rm m}}$$
 (3.28)

with

$$l_{\rm m} = (x_{\rm mlg} - x_{\rm cg})\cos\theta_{\rm AC,rest} + z_{\rm mlg}\sin\theta_{\rm AC,rest} + l_{\rm mlg}\sin(\theta_{\rm mlg} - \theta_{\rm AC,rest})$$
 (3.29)

$$l_{\rm n} = (x_{\rm cg} - x_{\rm nlg})\cos\theta_{\rm AC,rest} - z_{\rm nlg}\sin\theta_{\rm AC,rest} - l_{\rm nlg}\sin(\theta_{\rm nlg} - \theta_{\rm AC,rest})$$
 (3.30)

with h_{cg} computed using Equation 3.49.

With a chosen nose tire and the main and nose gear positions, the nose gear loading only depends on centre of gravity position and aircraft weight. Therefore by sampling these over their respective range, a diagram can be plotted showing which weight + centre of gravity combinations lead to insufficient nose static load, or to nose dynamic overload, determining which are feasible.

3.10.3. Final gear position and length

The gear initial design has now been investigated for the aspects requiring interaction between the different initial designs. If the turnover angle is below the desired limit, and the achievable weight and centre of gravity combinations are satisfactory, the gear can be kept as it was at the end of the initial design.

If not, it needs to be adapted:

- If turnover angle limit is not satisfied, the main gear is moved outboard. Moving the main gear aft is also a solution, however it reduces the rotation ability (see 3.8.3). Moving the nose gear fwd is neglected as it is already close to airframe nose.
- If static nose load is insufficient, nose gear can be moved aft, taking care of not increasing lateral turnover angle above the limit. As for turnover, moving the main gear aft is a solution, with the same drawback.
- If dynamic nose load is too high, reducing static nose load or reducing centre of gravity height
 are possible. The former may bring static load too low while the latter requires to modify the
 airframe to allow for shorter gear, leading to quite heavy modifications equivalent to restart the
 gear design process.

The different length can now be recomputed at the new positions chosen, using Equation 3.15.

3.10.4. Final kinematics

With the gear position and length fully defined, the initial kinematic concept can be confronted with reality. The main objective is to fit as much as possible of the folded gear within the airframe. The nose gear has very little option: folding fwd below the cockpit is the only option to avoid a fairing. Concerning the main gear there is more freedom, since all the airframe space behind the cabin is available. The constraint on the outrigger will depend on where it is positioned: a fuel tank is planned just outboard of the cabin, but the outer wing is empty. The 3D user interface of ParaPy can allow to try folded positions to check their feasibility.

Folding axis

Once the folded position of each gear is chosen, the folding axis can be computed. Chai and Mason [17] provide a mathematical method to compute the axis orientation, assuming the kinematics used is that of Figure 3.7a, as shown in Figure 3.18. It also requires that the gear length does not change during the folding. It uses the gear root position O, its extended position A and a desired folded position A', both including a second point defining the bogie orientation, respectively B and B'. The different points can be seen on Figure 3.18.

From these points, the vectors

$$\mathbf{V}_1 = \overrightarrow{OA} \tag{3.31}$$

$$\mathbf{V}_2 = \overrightarrow{OB} \tag{3.32}$$

$$\mathbf{V}_3 = \overrightarrow{OA'} \tag{3.33}$$

$$\mathbf{V}_4 = \overline{OB'} \tag{3.34}$$

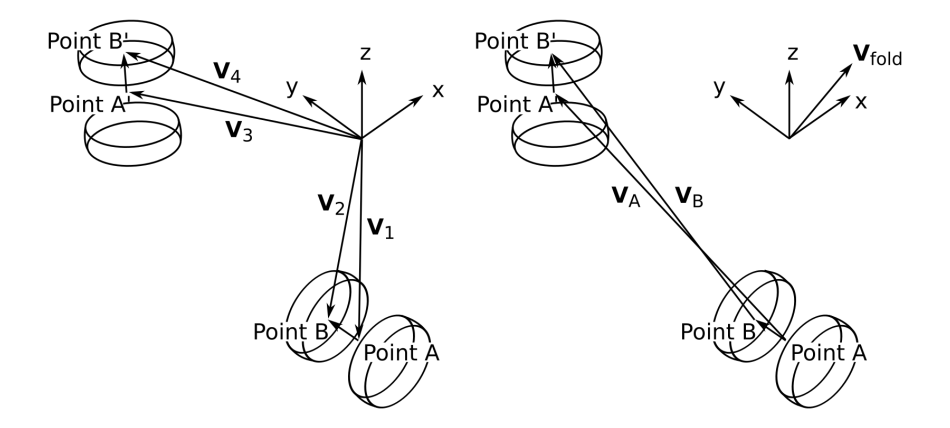


Figure 3.18: Mathematical method to compute folding axis of a gear for a desired folded position[17]

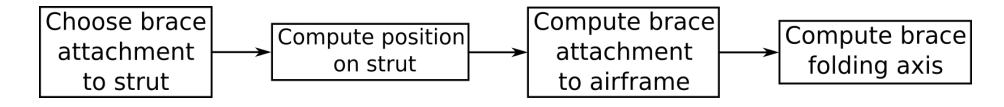


Figure 3.19: Mathematical method to compute folding axis of a gear for a desired folded position[17]

representing the points positions w.r.t. the gear root, and

$$\mathbf{V}_A = \overrightarrow{AA'} = \mathbf{V}_3 - \mathbf{V}_1 \tag{3.35}$$

$$\mathbf{V}_{B} = \overrightarrow{BB'} = \mathbf{V}_{4} - \mathbf{V}_{2} \tag{3.36}$$

representing the movement from A to A' and B to B', are defined. To bring A to A', the folding axis needs to be perpendicular to \mathbf{V}_A , and similarly for \mathbf{V}_B . Therefore the folding axis of the gear is obtained by the cross product of the two:

$$\mathbf{V}_{\text{fold}} = \mathbf{V}_A \times \mathbf{V}_B \tag{3.37}$$

Folding axis with different kinematic

If the strut is too long, it can fold itself in an upper and lower strut, requiring a brace for folding the lower strut at the same time as the upper strut. The kinematics are then different from those shown in [17], and no brace positioning method was found that could cope with the axis computed with the method detailed above. The folding is thus modified to planar along an axis perpendicular to extended and folded position:

$$\mathbf{V}_{\text{fold}} = \mathbf{V}_1 \times \mathbf{V}_3 \tag{3.38}$$

The brace is positioned with the steps shown in Figure 3.19, detailed below:

- 1. Choose the brace attachment point on the gear strut. It must be on the lower strut to allow for adequate kinematics.
- 2. Compute the position of this attachment point when the strut is extended, and when it is folded, based on the strut folding axis computed before.
- 3. Choose the vertical position of the brace airframe attachment point, then compute the brace airframe attachment position. The latter is the point equally distant from brace attachment points on folded and deployed strut, with the correct vertical position.
- 4. Compute the brace folding axis with the cross product of the vectors representing the brace in deployed and folded position (Equation 3.38).

The drawback of this option is that the bogie is not in the desired orientation once folded, since the points B and B' were not used. This can be solved by adding a pivot along the strut direction that can rotate the bogie to match the desired orientation. This however increase the complexity of the gear.

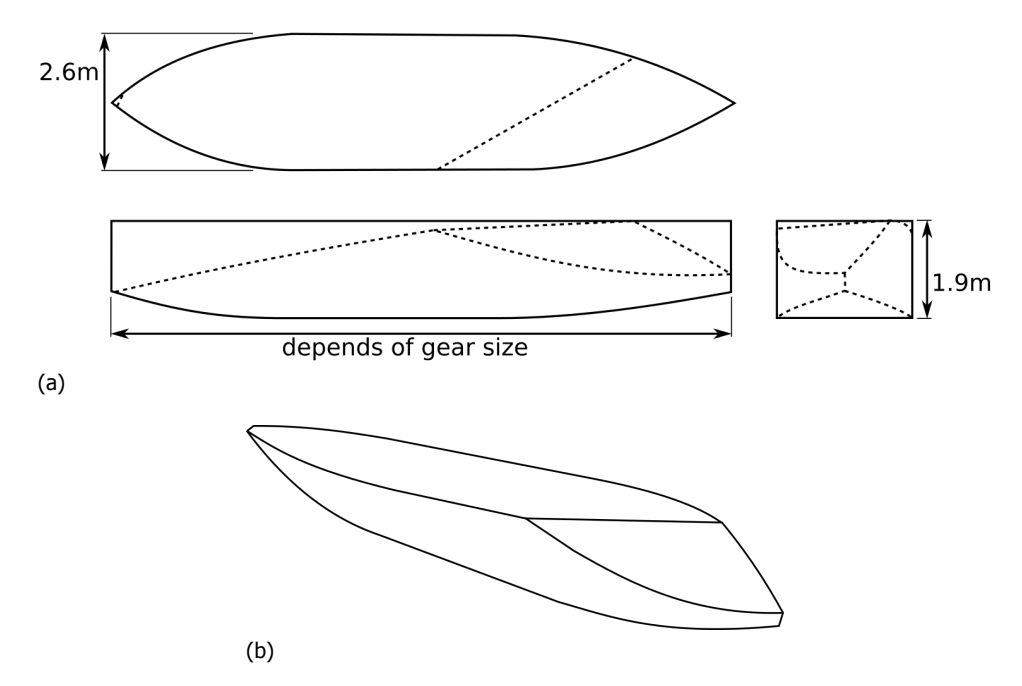


Figure 3.20: Fairing shape chosen, in (a) 3 views (final shape in dashed line), and (b) 3D view of final shape

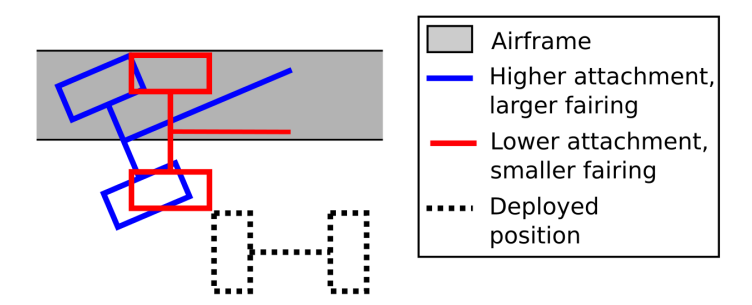


Figure 3.21: Influence of gear-airframe attachment vertical position on fairing size

3.10.5. Final fairing

Now that the gear folded position is determined, it is obvious if a fairing is needed or not. Among the three methods presented in 2.1, fairing design is only covered by Van Oene, however with the limitation of using only elliptical shapes. A more interesting fairing design was performed by Savoni and Rudnik [54], with a gear folding on the under side of a thin wing, with the engine on top as suggested by Rubio-Pascual [7]. To keep the fairing simple and close to axisymmetric bodies covered by the drag estimation formulas (see 3.11.4), it is decided to have a fairing shape as described by the continuous lines in Figure 3.20a. To fit better with the airframe, the volume is intersected with the airframe on the front part, and the aft part is trimmed to be aligned with the upper surface. The result is shown by the dashed lines of Figure 3.20a and in 3D on Figure 3.20b.

A smaller fairing is obviously desirable, which can be achieved by having as much as possible of the bogie and strut to fold within the airframe. This is influenced by the vertical position of the gear airframe attachment as shown on Figure 3.21, also changing the gear length. No other aspect previously checked will be changed as the bogie stays at the same position.

3.11. Figures of merit

With the gear fully defined, the different figures of merit to evaluate the design can be computed. The lateral stability derivatives have already been computed in 3.3, and the rotation ability in 3.8.3.

3.11.1. Gear weight

The landing gear weight can be estimated empirically or analytically. Among empirical methods, only accounting for aircraft take-off weight is insufficiently accurate [17], but accounting for other parameters such as gear length or wheel number improves the accuracy [11]. Raymer's formula [11] is used by Van Oene [18] on conventional aircraft gear design. Its main improvement is to account for gear length and wheel number. Assuming a non-kneeling gear with 2 main gear struts, the gear mass is $\lceil 11 \rceil$:

$$m_{\rm mlg} = 3.526 \cdot 10^{-2} \, m_{\rm AC,ldg}^{0.888} \, l_{\rm mlg}^{0.4} \, N_{\rm mlg}^{0.321} \, v_{\rm s1g,ldg}^{0.1} \tag{3.39}$$

$$m_{\text{nlg}} = 1.646 \cdot 10^{-1} \, m_{\text{ACIdg}}^{0.646} \, l_{\text{nlg}}^{0.5} \, N_{\text{nlg}}^{0.45} \tag{3.40}$$

with

$$v_{\rm s1g,ldg} = \sqrt{\frac{m_{\rm AC,ldg} g}{0.5 \rho_{\rm air,MSL} S_{\rm ref} C_{\rm L,ldg}}}$$
(3.41)

$$m_{\text{AC,ldg}} = 0.8 m_{\text{AC,to,max}} \tag{3.42}$$

It must be noted that $m_{\rm gear,main}$ account for both main gear struts.

Higher accuracy can be obtained through analytical methods [17, 19, 55] or finite elements methods [56, 57]. However these methods require a quite refined design, and are thus inadequate in this preliminary study.

3.11.2. Ground manoeuvring

In addition to being able to land, aircraft are required to manoeuvre on the airport. Computing the turning radii of the Flying V will allow to compare it to existing aircraft and thus determine if the gear position is good enough or if it needs some refinement. Using basic geometry it is possible to estimate the position of the axis around which the aircraft will rotate:

$$x_{\text{turn}} = x_{\text{lrp}} \tag{3.43}$$

$$y_{\text{turn}} = (l_{\text{m}} + l_{\text{n}}) \tan(90 - \beta)$$
 (3.44)

with $l_{\rm m}$ and $l_{\rm n}$ computed with Equations 3.29 and 3.30 respectively. The position of the turn pivot axis depends on the nose wheel steering angle, and since it is an axis there is no need for vertical position.

Based on this axis position it is possible to compute the turning radii of any point on the aircraft. The most relevant are:

- The nose gear and outer main wheel for margin with taxiways and runway edges during turns.
- The airframe nose and wing tip for margin with buildings.

On conventional aircraft and particularly the ones with very long fuselage such as A340-600, the tail turning radius is also of interest since it is different from the wing tip, and could hit a building cleared by the wing tip. On the Flying V this is not relevant since there is no tail, and the wing tip is both the most outboard and most aft point of the airframe.

The turning radii for the points selected above are computed as follows:

$$r_{\text{nlg wheel}} = \frac{l_{\text{m}} + l_{\text{n}}}{\cos(90 - \beta)}$$
(3.45)

$$r_{\text{outer main wheel}} = y_{\text{turn}} + y_{\text{mlg}}$$
 (3.46)

$$r_{\text{wing tip}} = \sqrt{(x_{\text{lrp}} - x_{\text{wing tip}})^2 + (y_{\text{turn}} + y_{\text{wing tip}})^2}$$

$$r_{\text{airframe nose}} = \sqrt{(x_{\text{lrp}} - x_{\text{airframe nose}})^2 + (y_{\text{turn}} + y_{\text{airframe nose}})^2}$$
(3.47)

$$r_{\text{airframe nose}} = \sqrt{(x_{\text{lrp}} - x_{\text{airframe nose}})^2 + (y_{\text{turn}} + y_{\text{airframe nose}})^2}$$
 (3.48)

3.11.3. Cabin floor height

To assess if the aircraft can be operated with existing ground handling equipment, the cabin floor height is computed when the aircraft is at rest on the ground. The ground height of any point in the airframe can be derived from the main gear position and the main gear strut length:

$$h(x, y, z) = l_{\text{mlg}} \cos \left(\theta_{\text{mlg}} - \theta_{\text{AC,rest}}\right) + R_{\text{tire}} + (z - z_{\text{mlg}}) \cos \theta_{\text{AC}} - (x - x_{\text{mlg}}) \sin \theta_{\text{AC}}$$
(3.49)

3.11.4. Fairing drag

The fairing drag can only be assessed simply through its zero-lift drag, as interference drag would need a CFD simulation. Raymer [11] provides the following formula, reused by Van Oene [18]:

$$C_{\rm D0,fairing} = C_{\rm f} \cdot FF \cdot Q \frac{S_{\rm wet}}{S_{\rm ref}}$$
 (3.50)

The different components are detailed below.

Flat plate skin friction coefficient

 C_f can be computed using the standard formulas for flat plate skin friction coefficient. Raymer however states that these formulas can overestimate the turbulent coefficient, and suggests to compute a cut-off Reynolds number that includes the surface roughness:

$$Re_{\text{cutoff,subsonic}} = 38.21 (l_{\text{fairing}}/k_{\text{roughness}})^{1.053}$$
 (3.51)

$$Re_{\text{cutoff,transonic}} = 44.62(l_{\text{fairing}}/k_{\text{roughness}})^{1.053}Ma^{1.16}$$
(3.52)

with $k_{\rm roughness}$ representing the surface finish roughness, for which Raymer provides generic values. If this Reynolds number is lower than the classical Reynolds number, it is to be used to compute the skin friction coefficient.

Form factor

The form factor FF depends on the slenderness ratio f of the fairing, which Van Oene considers to be low, thus advising to use the following formulas:

$$f = \frac{l_{\text{fairing}}}{\sqrt{(4/\pi)S_{\text{section,max}}}}$$
(3.53)

$$f = \frac{l_{\text{fairing}}}{\sqrt{(4/\pi)S_{\text{section,max}}}}$$

$$FF = 1 + \frac{0.35}{f}$$
(3.54)

with $S_{
m section,max}$ the maximal section of the fairing perpendicular to the flow direction.

Interference factor

It depends on the position of the fairing w.r.t. the wing and other close bodies, with Raymer providing values in several cases.

Wetted surface

The wetted surface S_{wet} is the surface of the fairing in contact with the external flow.

Process validation

4.1. Position and length

Since the gear design process detailed in 3.4 has been modified compared to the existing processes discussed in 2.1, it requires a validation. This section focus on position and length of the different gear, by applying the method to the A350-900 airframe, and comparing the result to the real A350-900 gear (available in [47]).

4.1.1. Assumptions made for the design

Due to insufficient data available for the A350-900, some assumptions had to be made to allow to apply the design method. They are the following:

- The centre of gravity vertical position is approximately at the middle of the fuselage, on the horizontal plane 3.4 m above the lowest point of the belly fairing.
- The lift curves of the A350-900 for take-off and landing are the same as those of the NASA High Lift Common Research Model (HL-CRM), available in [58, 59].
- The main gear attachment to the airframe is on the dashed line shown on Figure 4.1b.
- The A330 is used as reference aircraft for flotation and tire used.

The centre of gravity is likely lower, since cargo and fuel stored in the airframe lower part are heavier than passengers which occupy the airframe upper part. There is however no data to estimate this effect, and since a higher centre of gravity is unfavourable for gear design (see 3.8, 3.10.1, and 3.10.2 for example) the chosen position is preferred over a uncertain lower position that could be too favourable for the design.

The similarity between A350-900 and NASA CRM was already used by Faggiano [2, 3] when assessing the cruise performance of the Flying V, since the A350-900 cruise performance was not available. The CRM is a state-of-the-art concept airliner with a conventional configuration, thus very similar to existing state-of-the-art airliners. Since the high lift curves of the A350-900 are also unavailable, the same assumption is made, using the HL-CRM which accounts for flaps and slats to create a take-off and landing configuration.

The dashed line had to be chosen as the process of 3.4 (particularly 3.7) requires to assume a first vertical position for the gear, which is then updated if needed. This particular line was chosen because it is inside the wing inboard of engine nacelle (where the main gear is expected to be), and follows the wing lower surface dihedral, but higher. It thus seemed a good estimation to have the gear attachment inside the wing, but since 3D data was not available it could not be checked.

The A350-800 (cancelled project) was initially planned to replace the A330, thus following Currey suggestion to use an existing aircraft as reference for bogie and tire choice, the A330 is used for this. Since the A350-900 is about 30 t heavier, it is expected that the flotation will worsen, and that possibly larger tires will be needed. However this avoids a detailed flotation computation, as decided in 3.5.

Flight phase	Lift coefficient	Incidence (°)
Take-off	1.64	8.5
Landing	1.80	7.5

Table 4.1: Lift coefficient and incidence for A350-900 take-off and landing, from NASA HL-CRM

4.1.2. Design process

The A330 has two possible main gear tires (1400x530R23 and 54x21-23), however when placing 95% of the A350-900 maximum take-off mass of 280 t on 8 tires, only the 1400x530R23 is able to support the load. The A330 bogie is used.

With a much more conventional design than the Flying V, an outrigger does not seem needed on the A350-900. Since the outrigger position is left free to the designer (see 3.6) and its length is computed in the same way as the main gear, it does not need to be designed here to validate the process.

Using the NASA HL-CRM aerodynamic data [58, 59], the lift coefficients for take-off and landing are computed in Table 4.1, thus take-off is the limiting case.

The longitudinal aft centre of gravity position (visible on Figure 4.1a) is derived from the real A350-900 gear position and a 95 % load on main gear. The fwd position is derived from the aft position using a 20 % MAC centre of gravity range, with a 9.1 m MAC.

The take-off angle being lower than the 15° required for push-back inertia, the main gear position is determined by push-back inertia. Since gear length depends on lateral position, first the aircraft height from ground is determined such that 8.5° pitch can be reached with 0.5 m margin at the tail (materialised by the dashed line on Figure 4.1a). The shock absorber stroke is computed at 0.339 m.

The gear lateral position is then determined iteratively to find the position where the compressed gear touches the ground, and the gear with extended shock absorber can fold without colliding with the gear from the other side. The gear length is then measured. It can be checked on front view that the lateral position leaves a 9° roll angle with compressed gear before the nacelle touches the ground, higher than the 8° advised by [12].

The nose gear use the same tire and bogie as the A330, and is positioned such that is folds as far fwd as possible without colliding with the nose radome. Its length is such that the airframe stays horizontal. An insufficient nose wheel static loading with aft centre of gravity led to move the main gear aft by $0.6\,\mathrm{m}$.

4.1.3. Result and comparison with real A350-900

The gear obtained by applying the method presented in 3.4 is shown in red on Figure 4.1. The A350-900 and its gear, taken from [47] can be seen in background.

The designed gear has a lower track and very slightly longer wheelbase than the A350-900. The struts are 9 m apart laterally while they are $10.6 \, \text{m}$ apart on the real aircraft, a $15 \, \%$ decrease. The wheelbase is increased by $0.3 \, \text{m}$ to $29 \, \text{m}$, a $1 \, \%$ increase.

It can be noted that, according to the side view, the designed gear is shorter than on the aircraft by about 0.5 m, however the front view tells they are the same length. This is caused by the drawings from [47] in which the ground is closer to the airframe on front view compared to sideview. Comparing the height from ground shown with the specified ground clearances in [47], it seems that the front view matches with the maximum weight case, while the side view matches an empty aircraft weighing 140 t. Since the design method assumes that the shock absorber is fully compressed, it is closer to the maximum weight case, thus the designed gear has strut length similar to the real aircraft.

The wheelbase variation can be neglected, however the track variation cannot. One of the explanation for the track increase is that on the redesign performed here, the gear doors and their position were neglected. They are usually placed streamwise to minimize the effort they withstand, thus need to be placed in between the two gears folded position, on the aircraft midline. Moreover, as shown in 4.2 the shock absorber length is underestimated, leading to longer folded struts (since shock absorber is extended when folding), thus requiring larger track. Another possibility is that the larger track provided more clearance for engine or wingtip. A last possibility is that despite having a satisfactory turnover angle with the redesign (55°, quite below the 63° limit), the lateral stability was insufficient. These aspects were not considered in the design method because there is no data available on the Flying V to compute them. By neglecting them on the A350-900, the minimum track was considered.

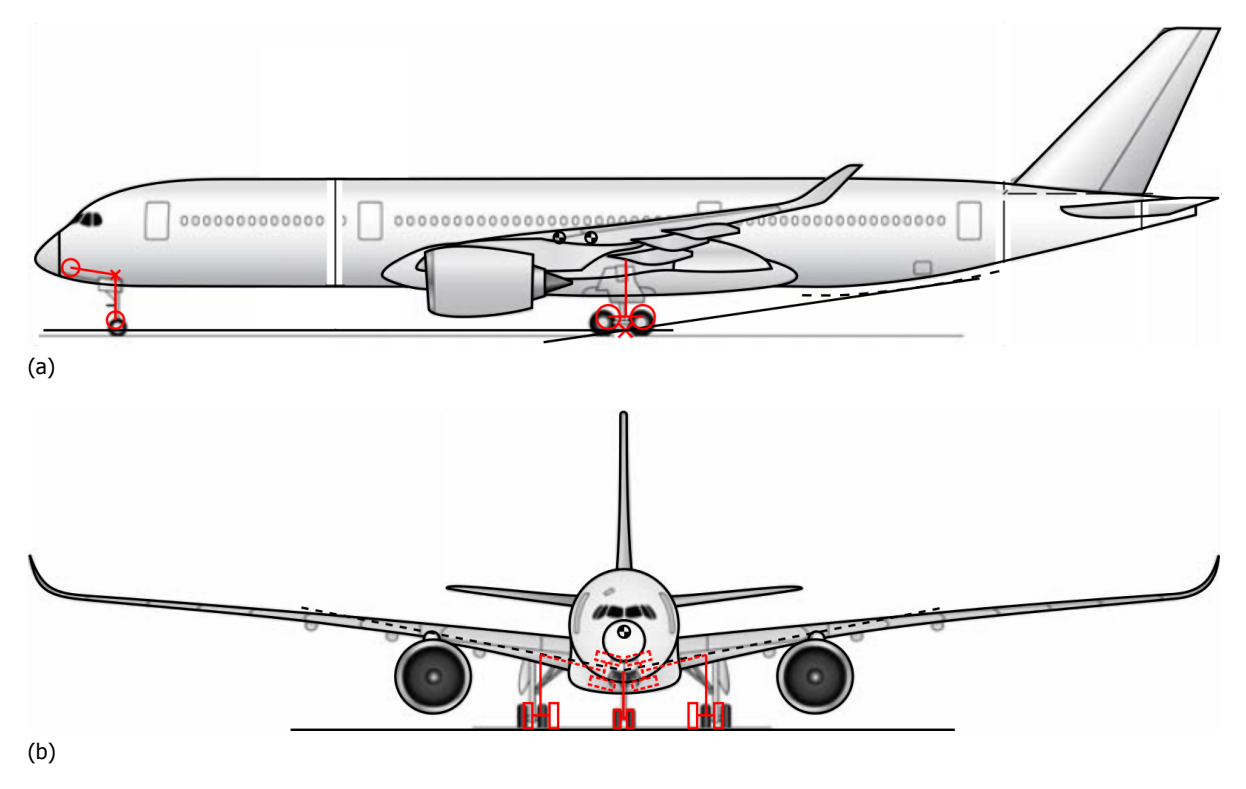


Figure 4.1: Validation of gear design method on A350-900, (a) side view and (b) front view

The bogie were chosen identical to those of the A330, thus are smaller than those of the A350-900. The flotation will thus be less favourable. The tires used by the A330 are the same as those of the A350-900 (except for the 54x21-23 since it cannot withstand the load). Computing the load per tire, it is visible that the tire is loaded almost at its maximum limit, thus an aircraft weight increase is hardly possible. This explains why the A350-1000 goes for 6 wheels bogie.

Except for the underestimated gear track, the gear design obtained by the method outlined in 3.4 is very close to that of the A350-900. The method is thus reliable for positioning the gear and computing its length. The outrigger length computation is then also reliable.

4.2. Shock absorber length

In the previous comparison with A350-900, the shock absorber is computed but cannot be validated as the A350-900 shock absorber stroke was not found. However according to Equation 3.14 the stroke is independent on the aircraft weight, and depends only on the tire and the vertical speed at impact, the latter being specified by regulation [26, 27].

The value found above is compared to other airliner shock absorber stroke in Table 4.2. All the aircraft presented are covered by CS-25 [26, 27] like the A350-900, thus should have a similar stroke to that computed above if the formula was valid. It can be seen that Currey's formula fits well for the smaller airliners like the Boeing 727 or 737, but does not fit for larger aircraft like the C-141, L-1011 or the DC-10 which all show shock absorber stroke about 2 times larger than the one computed above. The DC-10 has the closest maximum mass to the A350-900 of the aircraft shown, thus should be the closest, and it obviously is not.

The formula from Currey is thus significantly off for aircraft of size similar to the Flying V. Thus the shock absorber is not uniquely sized by the energy to absorb during landing impact. Detailed shock absorber design could be missing, but when detailing it, Currey aims for a final stroke similar to the initially computed stroke, thus the error size observed is too big to come from detailed design. The same formula is used by Torenbeek, Roskam and the three works used as reference to create the design method.

Since the total gear length is computed first to then obtain the strut length by subtracting the shock absorber length, underestimating the shock absorber length would only lower the aircraft at

Aircraft	Shock absorber total stroke (m)	Stroke from static to compressed (% of total)
DC-9	0.406	6
DC-10	0.660	10
C-141	0.711	11
L-1011	0.660	13
Boeing 707	0.559	14
Boeing 737-200	0.356	15
Boeing 727-200	0.356	18

Table 4.2: Shock absorber stroke validation [15]

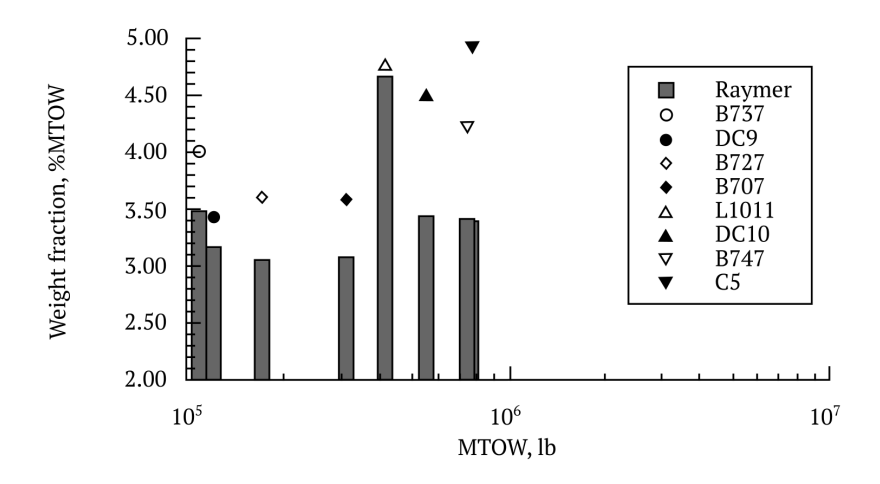


Figure 4.2: Validation of Raymer's weight estimation formula [17]

rest, without threatening the ground margin. Moreover, the method neglect the static to compressed shock absorber stroke, while Table 4.2 shows it is usually around 10%. Therefore for a total stroke twice the computed one, neglecting the static to compressed stroke cancel 20% of the error on the final aircraft position.

Another consequence of this error could be a folding problem: if on Figure 4.1 the main strut is 0.339 m longer when folding, the two gear would collide. However on the Flying V the gear are less likely to collide when folding due to the planform that makes it very unlikely to use the same folding as on A350-900.

Overall, the shock absorber stroke is underestimated, but partly cancelled by neglecting the static to compressed stroke, and would only bring an aircraft lower when at rest than expected. Therefore the method is used, and the aircraft height will be given with an uncertainty margin equal to the stroke.

4.3. Gear weight

The gear weight computation formula provided by Raymer is confronted with reality in Figure 4.2. It can be seen that like the shock absorber stroke formula, it is most accurate for relatively low aircraft weight. Here the reason is because it is a statistic formula, thus it is more accurate if more data is available to support it (like for low aircraft weights) and less accurate as aircraft weight increase.

The A350-900 (and the Flying V) have a maximum take-off mass close to that of the DC-10, which has a gear weight underestimated by about 1% of aircraft maximum take-off mass. Even if industrial and conception improvements made gear lighter compared to when the DC-10 was developed, it seems legitimate to assume a similar error on the result for the A350-900 or the Flying V.

4.4. Aerodynamic model extension

The aerodynamic model available for the sub-scale Flying V has been corrected for Reynolds number increase from sub-scale to full scale, and extended for control surface maximum deflection increase.

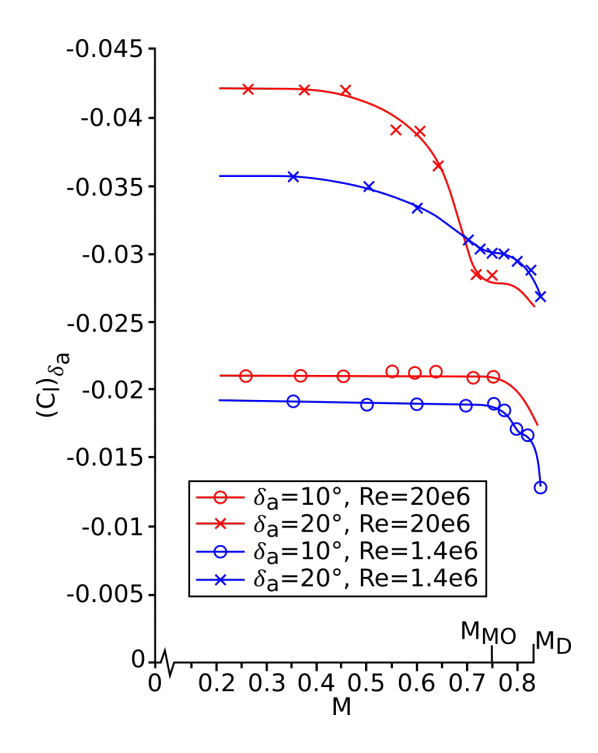


Figure 4.3: Increase of aileron efficiency with Reynolds number for Fokker F-28 Mk 1000 [60]

4.4.1. Revnolds effect

The Reynolds number correction of 20 % is based on experimental comparisons between wind tunnel test and full scale flight test found in literature. Obert [60] shows the improvement in rolling moment at given aileron deflection for the Fokker F-28 Mk 1000 in Figure 4.3. It can be seen that a 20 % increase is observed from wind tunnel to flight test at 20° deflection, due to the Reynolds number increase. The Reynolds number of the flight test, not provided by Obert was approximated by that of the Fokker 70 from [61], slightly larger than the F-28.

The increase is confirmed by Jiang [62] in Figure 4.4a, with however the limitation that much lower deflections could be tested. Conducting the simulation in transonic flow with a Mach number of 0.85 is the reason for the deflection limit: at higher deflection the flow separates at the rear of the airfoil. The effect is less pronounced at lower Reynolds number, but similar. The increase obtained here is higher: about 50% at 3° deflection.

An increase is also obtained for normal force (instead of moments until now) in [63], shown in Figure 4.4b. At 4°, the increase is about 20 % for the lower lift coefficient and 35 % for the higher lift coefficient, with still limited deflection for the same reason as for [62].

4.4.2. Deflection increase

Increasing the control surface deflection increase the force or moment generated, but only until a certain point where detached flow appears. The extension scheme detailed in 3.8.2 assumes that before a given limit, the behaviour is linear.

Linearity is shown to exist for normal force on 2D wing by Rennie [64] on Figure 4.5, with a linear behaviour until roughly 10° deflection in both directions (the airfoil used is symmetrical). Side force linearity for rudders is shown by Obert [60] on various aircraft on Figure 4.6, some having T-tails (in blue) and others having fuselage attached horizontal tail. Here the linear range spans until 15° in average, but up to 30° on the Fokker F-29 Model 1-1, thus quite more than in Rennie's results.

More interesting is that when comparing with Rennie, the normal force coefficient at which the linear range stops is approximately 0.4. The Flying V aerodynamic model however never approaches this value within 30° control surface deflection, as opposed to what is suggested by the curves shown here. Rennie considers a 2D wing with a control surface, thus has no part of span without control surface. Obert discuss only rudder in Figure 4.6, thus it would seem logical that the force coefficient is scaled just for the vertical tail, which full span is fitted with a control surface. On the other hand the

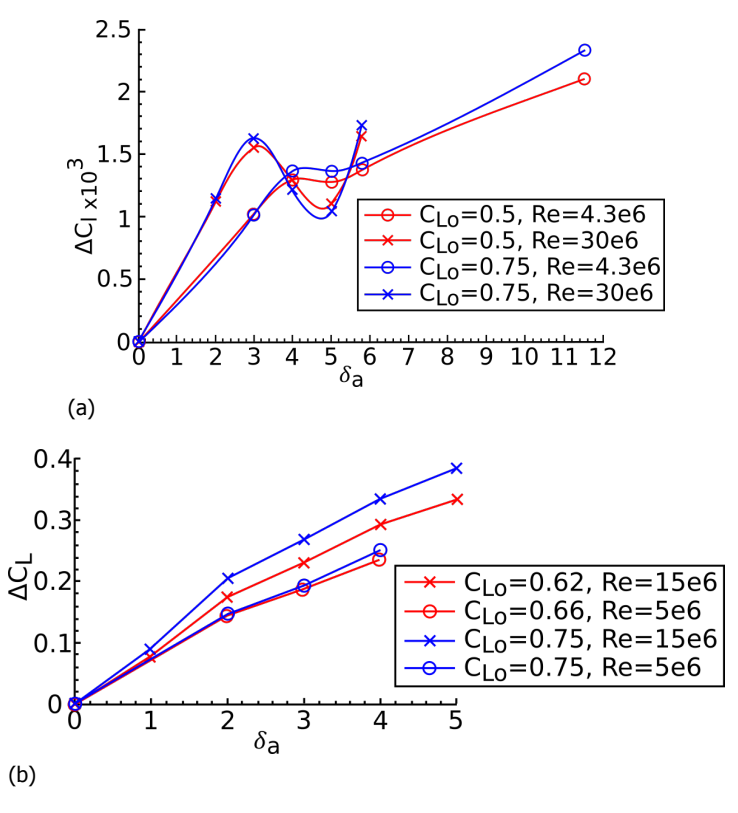


Figure 4.4: Increase of control surface efficiency with Reynolds number for (a) rolling moment on a half-wing [62], and for (b) normal force on a 2D wing [63]

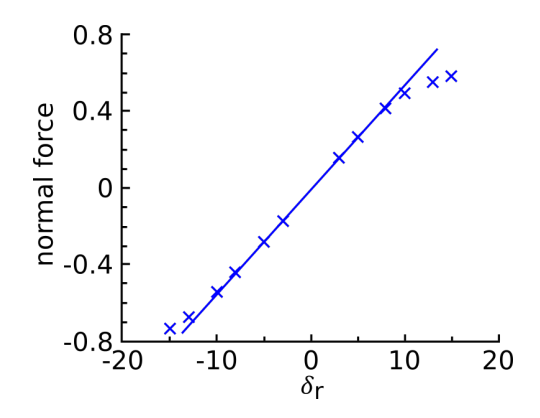


Figure 4.5: Variation of normal force with control surface deflection on a symmetric airfoil[64]

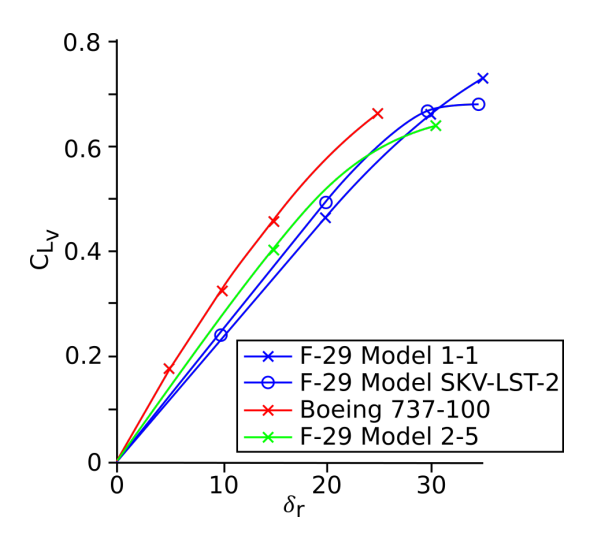


Figure 4.6: Increase of rudder efficiency with deflection for various aircraft [60]

Flying V has control surface only on part of the span.

The Flying V normal force coefficient is increased by a factor 2.65 if rescaled by the surface of the span fraction fitted with control surface instead of total wing surface. This brings the coefficient around the 0.4 limit of Obert and Rennie graphs, making its behaviour similar to that shown on the graphs. Instead of scaling up the coefficient for checking linearity, the linearity limit was scaled down, giving the 0.151 limit used in 3.8.2.

The main weakness of this is that Obert does not specify if the normal force coefficient displayed is computed using only the vertical tail surface. However applying this assumption to the Flying V gives similar force coefficient values to those displayed in Obert's graphs, thus the assumption seems more justified than considering linear behaviour until 30° deflection.

Linearity also exists for moments generated by the control surface [65], as shown on Figure 4.7 for pitch and roll moment. Unlike previously, this time a full aircraft is considered, removing any doubts on the scaling used for the coefficients. The graphs are roughly symmetrical, but slightly more linear with negative deflections. Since the deflection increase on the Flying V is toward negative deflection, only the left part of the graph is considered. It can be seen that linearity is a reasonable approximation until 0.11 for pitch moment, and until 0.08 for roll moment, and that the most inboard control surface is linear slightly longer than the most outboard. Therefore the 0.11 limit is used in the aerodynamic model.

It must be noted that the control surfaces are considered separately in Waters work, thus this raise the question of interaction between control surface. No literature was found addressing this, therefore instead of blindly extrapolating it, it was chosen to keep it to its value at the validity limit of the aerodynamic model.

4.5. Stability derivatives

4.5.1. Equivalent wing

The equivalent wing is used to compute the stability derivatives. According to [36] it is aerodynamically most accurate when used on a wing with constant leading edge sweep, or only minor changes, over the greatest part of the span, with fully attached flow. The Flying V has a 26.6° leading edge sweep change at 62% of span, and while the wind tunnel tests suggest a stall angle way beyond 30°, the flow is quite complex with several vortexes. It is thus unsure if the equivalent wing is accurate on the Flying V.

It should thus be validated for a configuration like the Flying V. However since such configuration does not match the statistical data used to derive the ESDU formulas, validating the equivalent wing for any of its aerodynamic properties computed with ESDU would combine errors of the equivalent wing and of the property computation. The ideal solution would be to simulate both wings in CFD and compare the aerodynamic properties. AVL offers a quick option for such simulation.

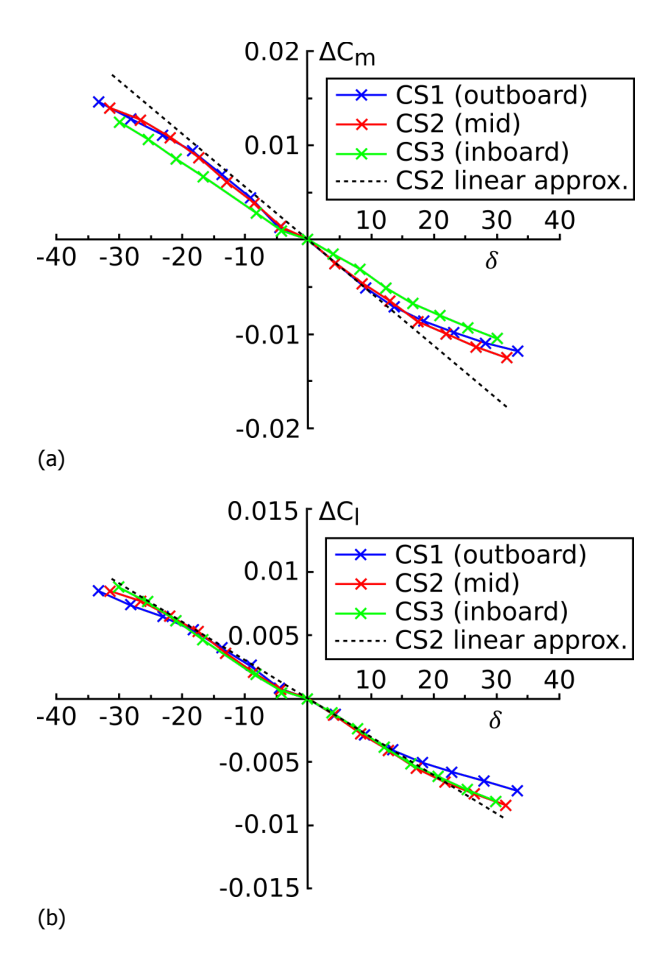


Figure 4.7: Variation with elevon deflection [65] of (a) pitch moment, and (b) roll moment

Root chord	24.0 m
Taper ratio	0.132
Aspect ratio	4.78
Surface (S_{ref})	883m^2
Mean Geometric Chord	13.6 m
Mean Aerodynamic Chord	16.3 m
Leading edge sweep	52.2°
Quarter chord sweep	48.5°
Half chord sweep	44.1°
Average dihedral	2.63°

Table 4.3: Flying V equivalent wing planform properties

The equivalent wing geometric properties are given in Table 4.3. This allows to implement the wing in an AVL file, which is then simulated for the same cases as the Flying V wing. The two wings incidence-lift and drag-lift polars are shown in Figure 4.8. It can be seen that both wings show similar behaviour in both case. The equivalent wing has on average $15\,\%$ lower incidence for the same lift coefficient, and on average $7\,\%$ higher drag coefficient at high lift coefficients and $20\,\%$ higher drag coefficient at low lift coefficients.

Since the two wings are quite swept back, vortexes can be expected in the flow, while AVL assumes irrotational flow leading to errors on the value computed. However it is believed that AVL will fail similarly on the two wings, providing a valid comparison, even if the actual values are wrong due to flow characteristics not modelled by AVL.

4.5.2. Stability derivatives computation

Using the equivalent wing, the stability derivatives are computed. Even when no modification was made in 3.3, since ESDU is based on conventional aircraft, the formulas are applied out of their validity range and needs to be validated.

This validation is performed on a set of blended wing body data described in [66], namely BWB4. According to De Castro, the BWB4 dataset is more reliable in terms of lateral stability derivatives, which is why it was chosen over the three other sets presented in De Castro's work. Figure 4.9 shows the configuration which, while different from the Flying V, has several features that match the main differences between the Flying V and the ESDU applicability domain:

- No clear fuselage defined.
- Double wing-tip fins.
- Engine nacelles above and aft of the wing.

This will allow to check if the changes made to the formulas are correct. It must be noted that the validation is done on the total derivative and not on each component detailed in 3.3. While such separation was available in the data on which ESDU is based, it was not on configurations similar to the Flying V.

There is however a limit to the data provided in [66]: it was obtained through low order methods. Therefore the accuracy of the experimental data might not be very high and suffer from similar shortcomings as the values obtained with ESDU or the values that could have been obtained with a 2D panel code (which were discarded in 3.3.1). However more reliable data could not be found with similar configurations where the stability derivatives due to sideslip were provided.

The results obtained from the formulas above are presented along the experimental results from [66] in Figure 4.10 for BWB4. The $J_{\rm W}$ parameter was set to 0.7 after varying it from 0.5 to 1.5 (range of value covered in ESDU). This value provides a better fit by allowing the fake-body Y_{v} to have a perfect fit with experiment, and the fake-body N_{v} to be equal to the experiment average value. Such situation could not be obtained with any of the other curves within the variation range of $J_{\rm W}$.

Overall the prediction is not very accurate, with errors often higher than $50\,\%$ as can be seen on the curves. This shows that ESDU is definitely not made for being used on such configuration. Therefore instead of aiming for accuracy it was chosen to look for trends and average values.

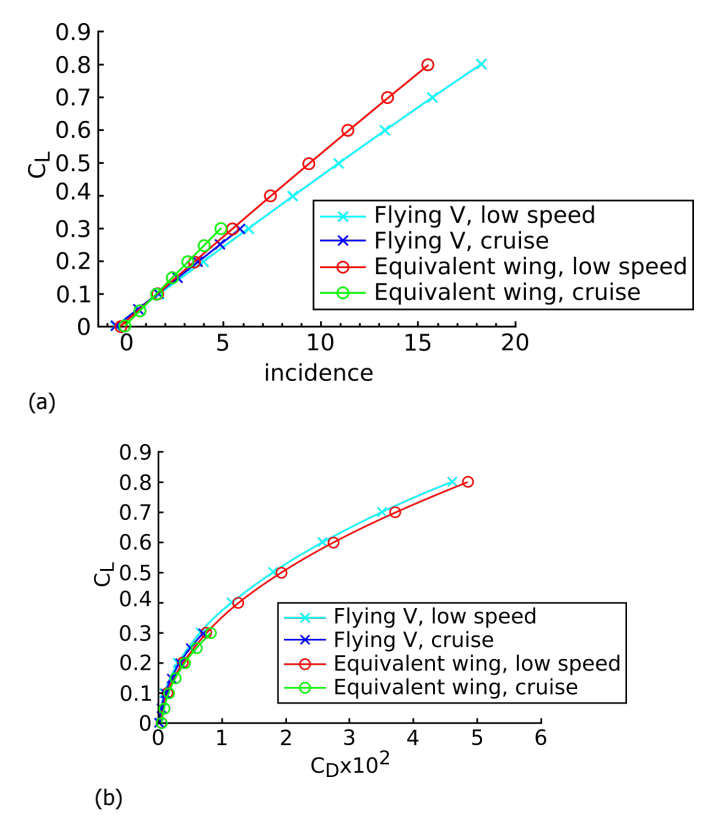


Figure 4.8: Comparison of Flying V and equivalent wing for (a) lift, and (b) lift-to-drag evolutions

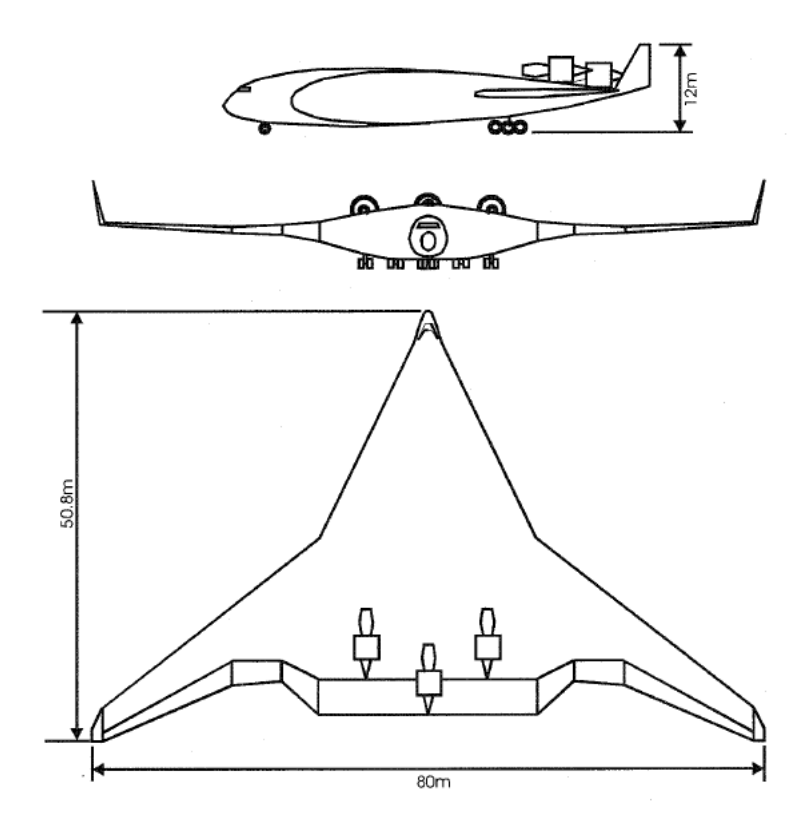
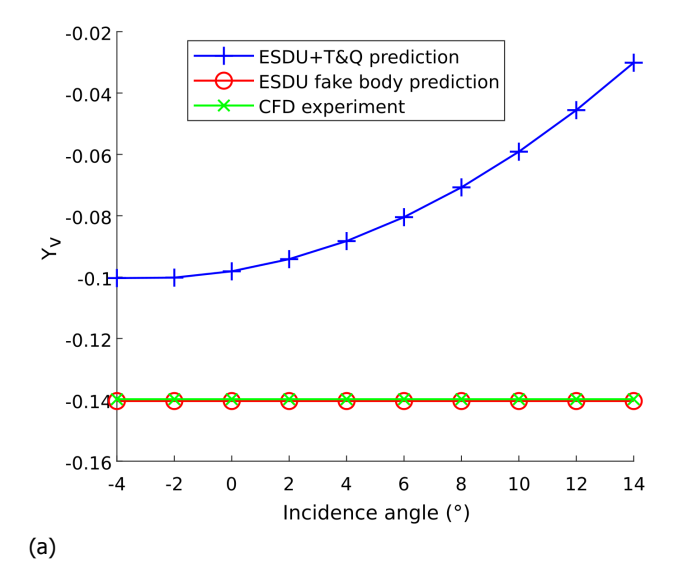
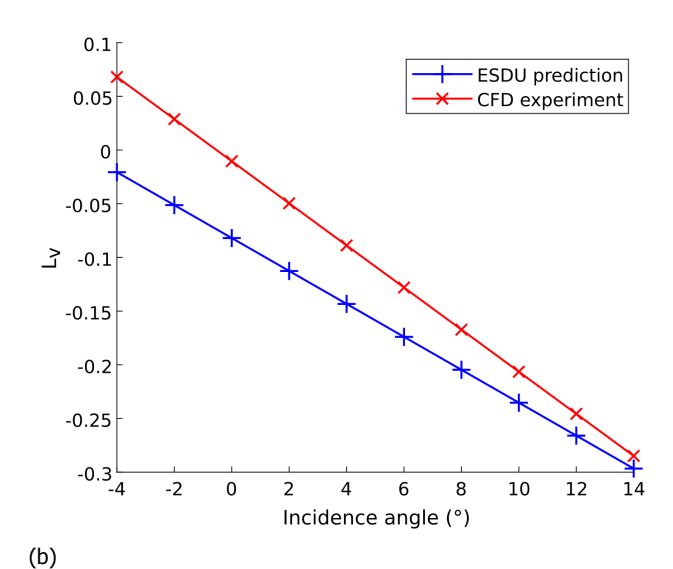


Figure 4.9: Blended wing body configuration used for stability derivatives validation [66]





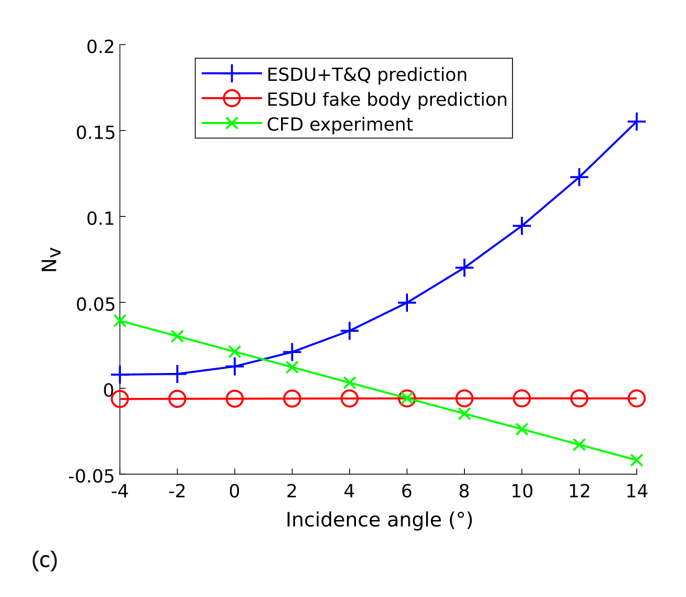


Figure 4.10: Validation with BWB4 data [66] of stability derivatives due to sideslip of (a) sideforce, (b) rolling moment, and (c) yawing moment

The low accuracy is particularly obvious for N_v , but can be explained by the fact that N_v is the sum of a destabilizing action from wing and body and a stabilizing action from the fin, leading to greater proportion of errors in its value.

The used value of $J_{\rm W}$ provides the best fit for the fake-body method: an exact fit for Y_v and N_v capturing the average value of the CFD experiment. On the other hand, the ESDU+T&Q method is unable of similar prediction, even for other values of $J_{\rm W}$. Therefore the fake body method is slightly better and is kept for computing the stability derivatives of the Flying V.

Concerning L_{ν} , it manages to capture the trend and gets closer to the experiment value when incidence increases. With an average error of 20 % for the part above 4° it is significantly more accurate than the others. The part below 4° is not considered for error percentage computation since the values are very close to zero, thus percentages get high very quickly for very small absolute errors. This increased accuracy can be because it did not need any modifications to the formulas used.

The dataset covers low speed, thus can be used to predict the accuracy for the Flying V low speed phases. These phases will happen at high incidence considering the lift curves. Therefore a quite accurate Y_v can be expected due to the exact fit, and similarly for L_v with an error dropping to 5% at high incidences. However since the N_v computation only captured the average value, with the experiment showing a decreasing trend it can be expected than N_v will be overestimated. Providing a percentage would make little sense as the average value is close to zero, making the distance to the real value much larger than the value itself. With the scaling of this configuration, the experiment N_v is about 0.05 lower than the obtained value.

A worrying aspect concerning N_v is that positive values are wanted for acceptable flight dynamics [67], while BWB4 shows a decreasing N_v with incidence, dropping below zero around 5°. This does not suggest interesting flight dynamics.

4.6. Ground manoeuvring

There is a significant approximation made in the formulas of 3.11.2: each gear is assumed to behave as if there was only one wheel at the center point of the bogie. This allows to place easily the turn axis by intersecting the perpendicular to each wheel, but in reality the wheels are not at the center point, thus resists the turn and increase the radii.

Thus the geometrically computed turning radii need to be checked against real turning radii to evaluate how much the friction changes the radii. Existing aircraft have a set of turning radii for different airframe points provided in their technical documentation [45–49]. The computed and real turning radii are compared in Annex A for the Airbus A350-900 (Tables A.1 and A.2) and the Boeing 777-200 (Tables A.3 and A.4). The A350-900 is chosen because the Flying V is designed for the same mission and the Boeing 777-200 because it is the closest Boeing in terms of mass range to the A350-900.

It can be seen that the geometrical computation is in general below the real value. The worst case is the A350-900 outer main wheel with up to 17.6% lower prediction than reality. The other turning radii on the A350-900 are all predicted within 7%. The Boeing 777 is the closest in average with a maximum under-prediction of 4.5%. The fact that the Boeing 777 is closer to the geometrically computed value while using a 6 wheels bogie is due to the steering system implemented in the bogie according to Chai and Mason [17].

In general the outer main wheel is the worst predicted of the computed radii, with a large increase in error for the highest steering angles. Until 60° steering angle, the A350-900 outer main wheel is predicted within 7% similarly to the other radii. The limited error leads to consider the computation accurate and not needing a correction at this point.

5

Results

5.1. Exploratory study outcome

The exploratory study allowed to get some basic feeling of gear position and length. It confirms that the wing tip is the limiting point that defines the airframe position w.r.t. ground, thus that defines the gear length at a given position. Moving the gear forward increase the required length, while moving it aft make it shorter. If the gear is positioned just aft of the centre of gravity as specified in 3.2, the airframe height required to avoid tail strike is about 7 m. This height led to implement the actuated tilting bogie (see 3.7.3) and to use the outrigger to shorten the gear strut.

Dihedral angle variation also confirmed its influence on airframe required height, thus on gear length, with about 0.25 m required height reduction per degree increase. The influence is slightly larger on the outerwing (see Figure 3.4) since its span is larger, thus moves more the wing tip for the same dihedral increase.

5.2. Three airframe configurations

With the exploratory study pointing towards long gear, dihedral is used to shorten the gear and define three airframe configurations as follows:

- The "default" configuration, which is the unmodified airframe. This configuration is used as reference in comparisons.
- The "floor 5.5" configuration, with dihedral values that bring the cabin floor at 5.5 m from the ground for ground handling.
- The "max dihedral" configuration, with dihedral values such that the gear is the shortest possible.

The left halves of the configurations front view are shown in Figure 5.1 and their dihedral values are provided in Table 5.1. All configurations will be analysed and compared, to allow a future decision on which configuration is the best for the Flying V. No choice is made in this work.

5.3. Gear design

5.3.1. Take-off and landing angles

The sub-scale free air lift curves are available from a RANS simulation [8] and wind tunnel tests [8-10], but are not satisfactory for full-scale because of a too low maximum lift coefficient. An aerodynamic adjustment is assumed:

	Default	Floor 5.5	Max dihedral
Inner dihedral (°)	0.0	1.0	4.4
Outer dihedral (°)	7.0	9.0	16.3

Table 5.1: Dihedral angles for the different configurations defined for analysis

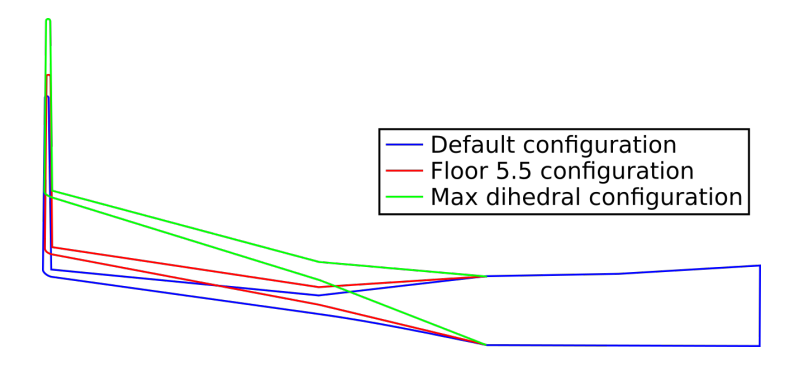


Figure 5.1: Front view of the three configurations defined, showing dihedral change

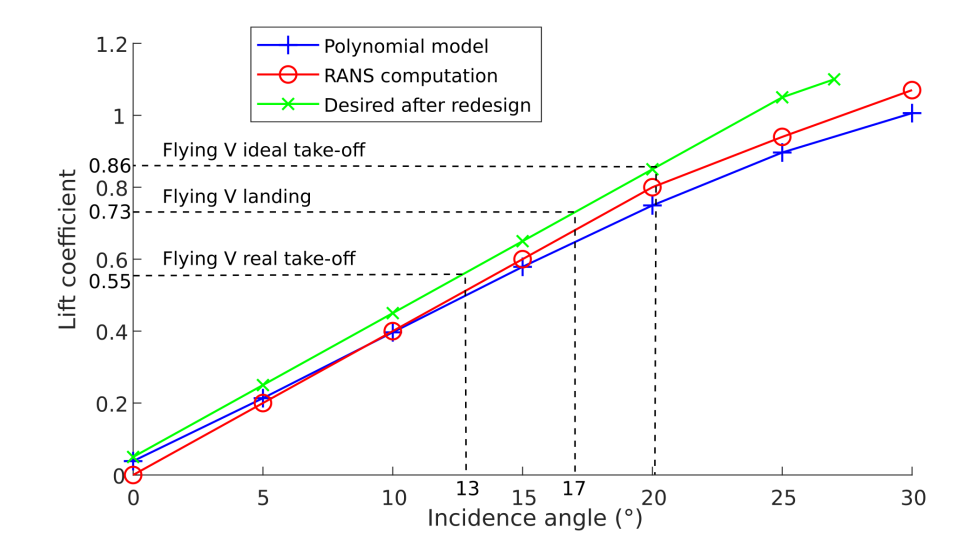


Figure 5.2: Experimental lift curves of the Flying V sub-scaled model [8, 10] superimposed with desired lift curve, out of ground effect

- No pitch break until at least 25°.
- The lift curve is linear until 25°.
- A maximum untrimmed lift coefficient of 1.1 is available at 27°.

All curves are shown in Fig. 5.2, with the wind tunnel results approximated by the easier-to-use polynomial model of Ruiz-Garcia [10].

The Flying V maximum lift coefficient is unchanged for take-off or landing since no high-lift devices are available. From Equations 3.1 and 3.2, the maximum lift coefficients for take-off and landing are respectively 0.86 and 0.73 providing take-off and landing incidences of respectively 20° and 17°.

Using Rolls-Royce Trent XWB-75 engines [68], the Flying V OEI thrust-to-weight ratio is about 0.125. Regulation requires a minimal 2.4 % climb gradient [26], i.e. approximately $\gamma > 0.024\,\mathrm{rad}$. According to the Flying V lift-to-drag ratio in ground effect from [69], the required lift-to-drag ratio for such climb gradient is obtained at most at 13° incidence, limiting the take-off incidence. Landing is thus the highest incidence.

The roll angle to achieve is chosen as 8° from Van Oene[18] and Torenbeek[12].

The take-off and landing speeds are respectively $93\,\text{m/s}$ and $72\,\text{m/s}$ (resp. $190\,\text{kn}$ and $140\,\text{kn}$). The landing speed is identical to A350-900 [47]. The take-off speed is $20\,\%$ higher than A350-900 ($78\,\text{m/s}$, based on similarity with NASA HL-CRM) but acceptable as the Concorde was around $110\,\text{m/s}$ at take-off. Since the landing is the limiting case for incidence, it could be interesting to limit the

¹According to Wikipedia, en.wikipedia.org/wiki/Concorde#Brakes and undercarriage

	Default	Floor 5.5	Max dihedral
	(42.7)	(42.8)	(42.8)
Position, option 1 (m)	{ 13.4 }	{ 13.4 }	{ 13.4 }
	(-0.70)	(-0.60)	(-0.50)
Length, option 1 (m)	4.54	3.87	1.26
	(46.7)	(46.7)	(46.7)
Position, option 2 (m)	{20.3}	{20.3}	{20.3}
	(0.10)	(0.46)	(1.66)
Length, option 2 (m)	3.21	2.79	1.22

Table 5.2: Outrigger characteristics for the different configurations

pitch angle to reduce the gear length required. Incidence can be reduced by increasing speed, but that means longer landing distance, usually considered undesirable by airlines. Ground effect and the negative flight path could also reduce the required pitch, however since the lift performance is based on an assumption (see 3.2.2), these aspects are neglected to not provide a too optimistic environment. Thus the required pitch angle is kept at 17°.

5.3.2. Bogie and tire choice

Since Figure 3.9 wheels and strut number was shown to be out of date (see 3.5.2), they are decided based on existing airliners of similar weight (260 t [4]). Using the A350-900 as reference (like the A330 was used in 4.1), a gear with two main struts and four wheels should be sufficient. With a maximum take-off mass inferior to that of the A350-900, the same bogies and tires are used (1400x530R23 on main gear, 1050x395R16 for nose gear, bogie dimensions in [47]) and ensure similar or better flotation for the Flying V.

Accounting for margins around the tires, the folding space required are:

- For the main gear: 3.60 m along x-axis, 2.34 m along y-axis, 1.56 along z-axis.
- For the nose gear: 1.16 m along x-axis, 1.21 m along y-axis, 1.16 along z-axis.

5.3.3. Outrigger initial design

The outrigger aims to ensure a 0.5 m ground clearance of wing tip in all combination of pitch and roll below respectively 17° and 8°.

To be able to deal more easily with overrotation, the outrigger is tilted 17° backward, such that it is perpendicular to the ground when touching it at the maximum pitch angle the aircraft is supposed to reach.

Ideally the outrigger should always touch the ground on the runway, constraining its lateral position to $y_{\rm outrig} = 13.4\,\mathrm{m}$ (see 3.6.2). As this is outboard of trailing edge kink, the outrigger cannot be more aft than the aft spar to not interfere with the control surface, however the most aft it is, the shortest it will be. It is thus placed slightly in front of the aft spar, at the position given in first line of Table 5.2. The associated length is given on the second line. While the outrigger will always touch the ground on the runway, it is quite long.

This led to consider a more outboard position for the outrigger, bringing it closer to the wing tip, which makes it shorter thus lighter. The position considered is given on third line of Table 5.2, and is at the leading edge kink, with $y_{\rm outrig}=20.3\,\rm m$, still very close to the aft spar. In this position, if the aircraft is misaligned by more than 2 m on a 45 m runway, one of the outrigger will touch ground outside of the runway. However the decrease of outrigger length is significant, with more than 1 m decrease for Default and Floor 5.5 configurations. The length does not vary much for Max Dihedral since it has a shape minimising gear length, thus the span fraction on which dihedral is applied ends at a constant height from the ground.

The lengths presented in Table 5.2 do not account for tire or shock absorber compression. Instead they are the required lengths such that if a rigid beam of that length is placed at that location, the wing tip ground margin will be satisfied. Tires were not chosen because there are too many unknowns about the load to be supported. This leads to no shock absorber sizing on the outrigger since the formula given in 3.7.2 is unusable without a strut loading.

Position	Fwd CG	Aft CG
w.r.t. nose (m)	30.7	32.1
w.r.t. MAC (%)	41.4	49.2

Table 5.3: Centre of gravity range for the Flying V

With the outrigger ensuring the wing tip ground margin, the main gear can be shorter. However reaching take-off incidence should still be possible, and an outrigger failure should not reduce the achievable roll angle too much to still allow for cross-wind landing. Therefore it is chosen that the main gear should allow for 0 m wing tip ground margin at 17° pitch and 7° roll if considered alone.

5.3.4. Main gear initial design

A 2 % stability margin is used for the Flying V, ensuring static stability while reducing trimming penalty. The centre of gravity positions are given in Table 5.3, derived from the aerodynamic centre of Faggiano and assuming a 1.4 m range. The range was chosen from the A330, instead of the range computed in 4.1 for the A350-900 for which the most fwd position led to nose overload at maximum weight, and would possibly impede rotation due to the smaller moment arm of control surfaces on the Flying V.

With the constants in Equation 3.14 replaced by their numeric values given by Roskam [13] and accounting for a 1 inch (2.54 cm) margin [12, 13, 15], the shock absorber stroke is:

$$s = \frac{v_z^2}{2.4g} - 0.5875s_t + 0.0254 \tag{5.1}$$

Since an achievable $v_{\rm z,ldg}$ of 3.05 m/s is required by CS-25 and with the tires chosen in 5.3.2, the shock absorber length computed is 0.339 m, the same as in 4.1 since the formula to compute it is independent of aircraft weight.

An initial gear position and length is not provided since it will be updated immediately, thus is of little interest. It is however decided to tilt the gear strut aft by 10° such that it is more vertical during impact, as observed on existing airliners. 17° would make it exactly vertical according to the lift curves chosen, however it is unknown if the approximately 10° value observed on airliners is to match landing pitch angle, or because increasing it further was detrimental, thus 10° is kept. In a similar way, the bogie tilting angle used to shorten the main gear length is chosen at 35° from the A330.

5.3.5. Main gear refinement

As for the A350-900 in 4.1, the main gear position is modified by push-back and rotated tipover. As mentioned in 3.8.1 and 3.8.4 the longer the gear, the more aft it will have to move to satisfy these criteria. With gears length around 7 m according to the exploratory study, the movement aft is around 2 m. This greatly increases the moment arm in Equation 3.18, making rotation harder.

Therefore the bogie locking option of 3.8.1 is used, moving the push-back tipover limit fwd by 1.02 m. The option to stabilise rotated aircraft through control surfaces (mentioned in 3.8.4) is investigated at the same time as rotation ability is checked. The control surface deflection (all surfaces deflected at the same angle) required to reach zero pitching moment are shown in Figure 5.3, for three different longitudinal gear position. The "cg fwd" curves follow the case described in 3.8.3 for ability to pitch up the aircraft, while the "cg aft" curves follow the case described in 3.8.4 for ability to counter weight induced pitch-up at high incidence.

The "cg fwd" curves are all far from saturation at high incidence, with at most 50 % of maximum pitch-up deflection. At low incidence, they reach up to 66 % of maximum pitch-up deflection, for the most aft gear position checked. This gear position satisfies both rotated and push-back tipover without the improvements suggested, showing that rotation is indeed hard with such aft gear. For more fwd gear however the aircraft should be able to pitch up, but with an unknown pitch rate since aircraft dynamics and inertia are not available and would require a separate study.

The "cg aft" curves do not exceed 10% of maximum pitch-down deflection, proving that counteracting the weight pitch-down moment with control surfaces is not an issue at high incidence. This allows to loosen the constraint on rotated tipover, thus the problematic most aft gear position mentioned in previous paragraph will not be used, making rotation easier.

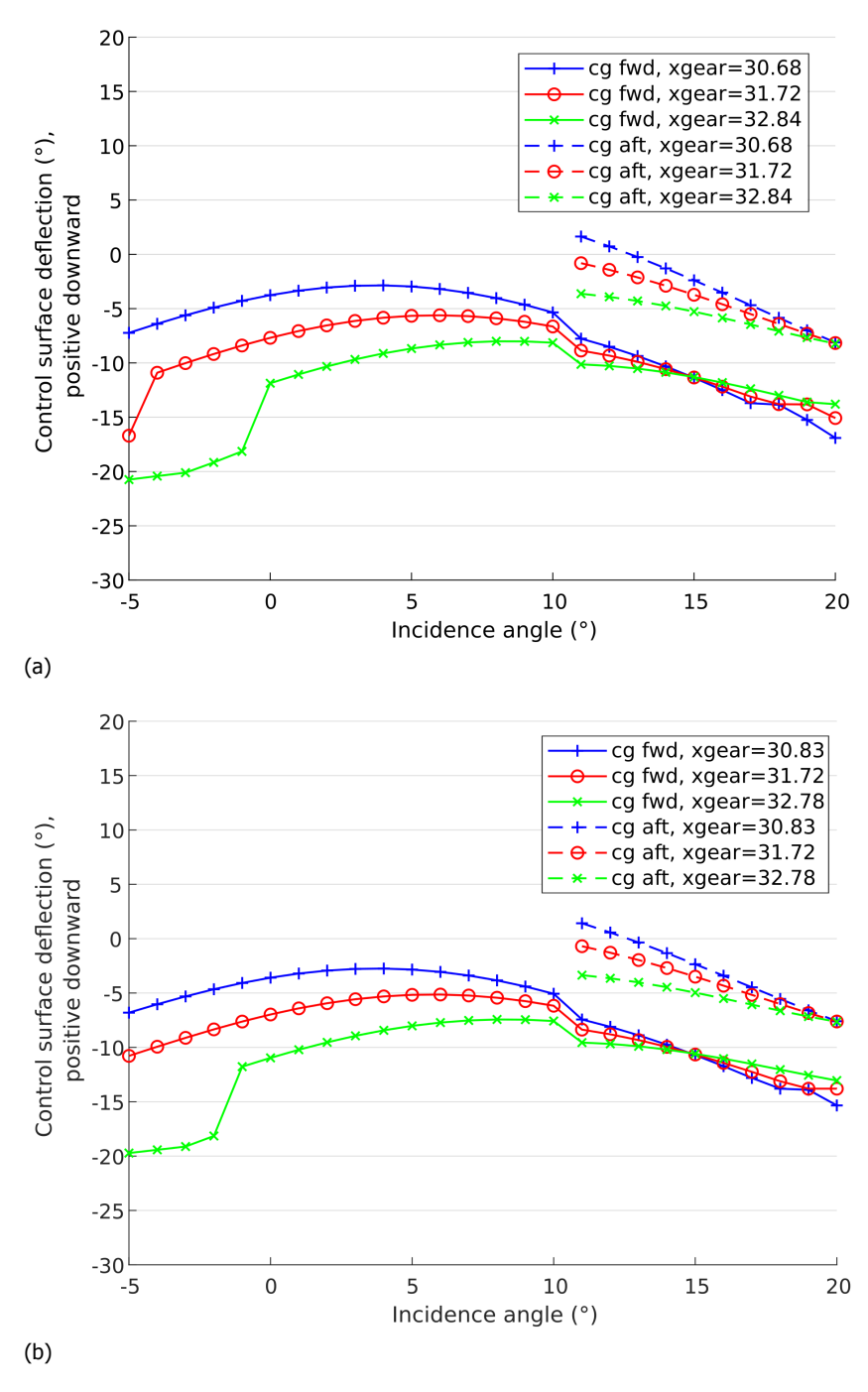


Figure 5.3: Control surface deflection required for zero total pitching moment at different incidence for (a) default configuration, and (b) floor 5.5 configuration

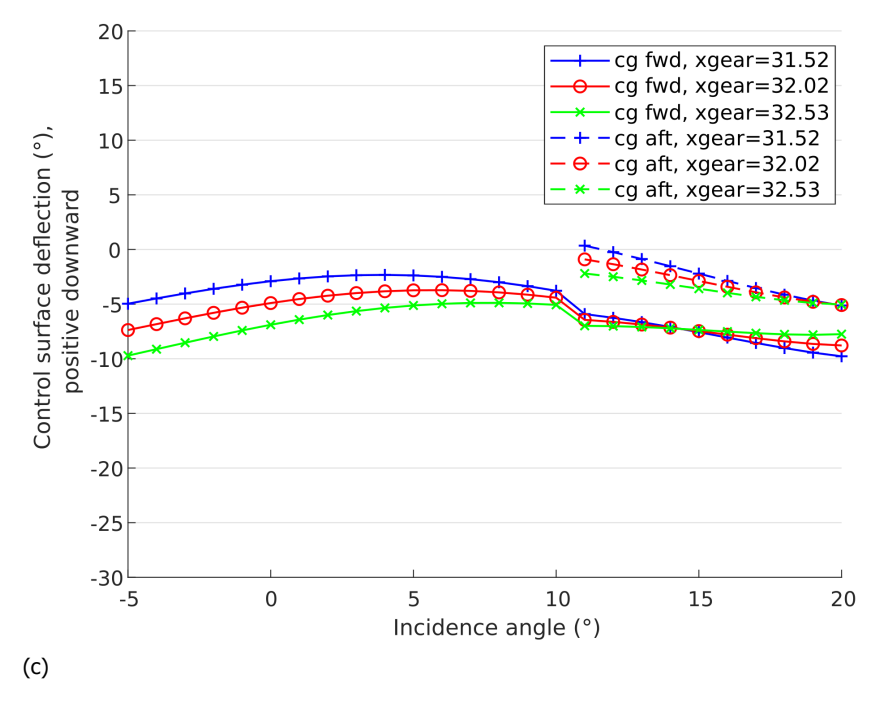


Figure 5.3: (continued) Control surface deflection required for zero total pitching moment at different incidence for (c) max dihedral configuration

	Default	Floor 5.5	Max dihedral
	(31.8)	(31.8)	(31.5)
Main gear position (m)	{ 6.1 }	{ 6.1 }	{ 6.1 }
	(-0.658)	(-0.658)	(-0.658)
Strut length (m)	6.03	5.30	2.65 ´

Table 5.4: Final main gear position and strut length

The gear position is updated, and its final value for each configuration is provided in Table 5.4. The vertical position is chosen due to kinematics in 5.3.7. Due to the strut tilting, the longitudinal position was adjusted such that the gear contact the ground at the same point (since it is that ground contact point that determines longitudinal tipover). Strut tilting also makes the gear attachment to be in front of the aft centre of gravity, while the bogie is behind as required by static tipover.

The lateral position is an example of a value that was chosen early, then kept because it was not causing any problem. Before implementing the bogie locking and checking rotated stability through control surfaces, the gear concept was more aft, making rotation harder. Thus it was moved outboard to bring it closer to the wingtip and make it shorter, thus slightly improving rotation capability. To be able to attach it to the cabin constant frames for better structure integration, and to allow stretching possibility, it was moved inboard as little as possible, bringing it to $y_{\rm mlg} = 6.1\,{\rm m}$. Modifications in aerodynamic model (see 3.8.2) moved the gear forward, but the lateral position never raised an issue, thus was kept.

5.3.6. Nose gear design

With the cabin occupying most of the space in the forward part of the Flying V, the only option to have a forward folding nose gear without a fairing is to use the space below the cockpit as shown on Figure 5.4 derived from an unpublished work on the Flying V. This option is chosen as a fairing would reduce the aerodynamic performance of the aircraft.

Thus the nose wheel is constrained to fold at $x=2.33\,\mathrm{m}$ if shock absorber extension is not counted. This folded position is chosen to allow shock absorber extension within the airframe and without interfering with the radome (which was assumed the same size as on the A350. The gear strut attachment to the airframe is positioned to fit between the cabin floor and the airframe lowest point, at $z_{\rm nlg}=-1.05\,\mathrm{m}$.

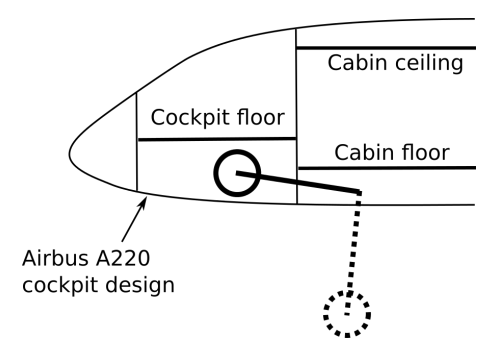


Figure 5.4: Option considered to fit the nose gear

	Default	Floor 5.5	Max dihedral
Nose gear position (m)	$ \begin{cases} 7.11 \\ 0.0 \\ -1.05 \end{cases} $	$ \begin{cases} 6.47 \\ 0.0 \\ -1.05 \end{cases} $	$ \left\{ \begin{array}{c} 3.64 \\ 0.0 \\ -1.05 \end{array} \right\} $
Nose gear strut length (m)	4.34	3.70	0.88
Turnover angle (°)	54	51	35

Table 5.5: Final nose gear position and strut length

Having a large wing surface, the Flying V can easily generate undesired lift while taxiing or when parked. Therefore looking at the lift curve it was decided to place it at -3° incidence at rest to be close to the zero-lift incidence of the desired lift curve slope on Figure 5.2. For best load reception, the nose gear will be pitched such that it is perpendicular to the ground.

This determines the nose gear positions and length for the different configurations, given in Table 5.5.

5.3.7. Final gear design

Lateral turnover

The lateral turnover angle is computed with the gear positions from Tables 5.4 and 5.5, and given on third line of Table 5.5. It is comfortably below the 63° limit value suggested in [12, 13, 15], thus does not lead to any modification on the gear position.

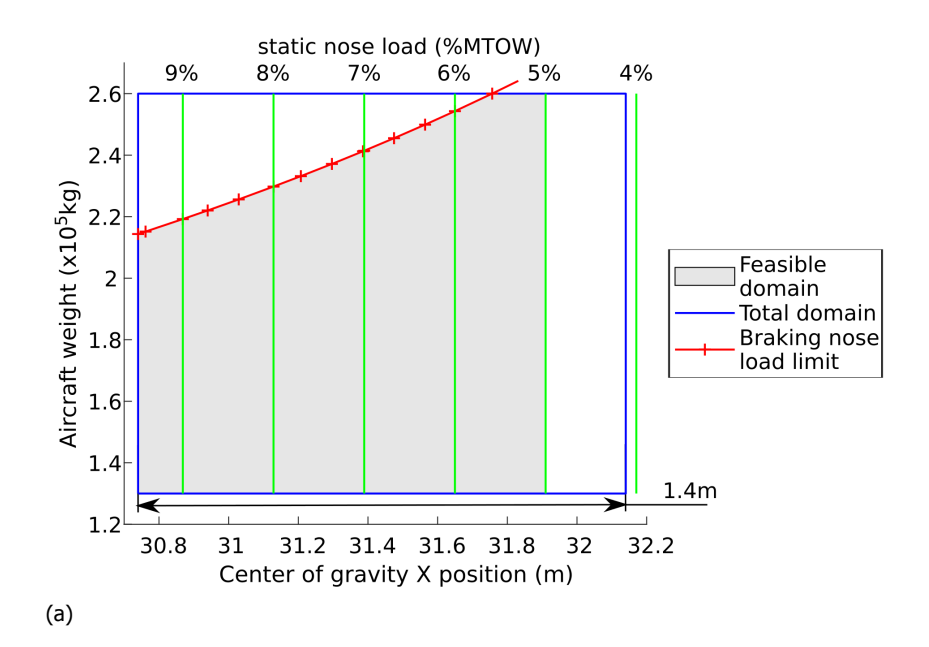
Nose gear loading

As discussed in 3.10.2, nose gear loading is investigated through weight vs. centre of gravity diagram showing the feasible combinations. For these diagrams, it is assumed that:

- The limit masses are $m_{\rm AC,to,max} = 260\,\rm t$ and operating empty mass of 130 t, taken from [4].
- The limit centres of gravity are the ones given in Table 5.3.
- The nose gear strut tilt angle $\theta_{nlg} = -3^{\circ}$, making it perpendicular to ground for the aircraft at rest.
- A design is feasible if the nose gear load is higher than 5 % and the braking load is within tire limits.

The static load limit is chosen from recent airliners technical data [47-49] which is deemed more relevant than Torenbeek [12] suggested value. Concerning braking load, tire maximum dynamic load is assumed to be 50% higher than maximum static load, following the trend shown in [51]. The diagrams obtained with the gear positions of Tables 5.4 and 5.5 are shown in Figure 5.5.

It can be noted that all configurations have some of the most aft centre of gravity positions unavailable due to insufficient loading. This can be solved as was done on the A350-900 in 4.1 by moving the main gear aft. Checking the nose gear load was forgotten when designing the gear, and realised too late to change it, hence the current state of the diagrams, with the max dihedral configuration on Figure 5.5c having no feasible centre of gravity position because of insufficient loading.



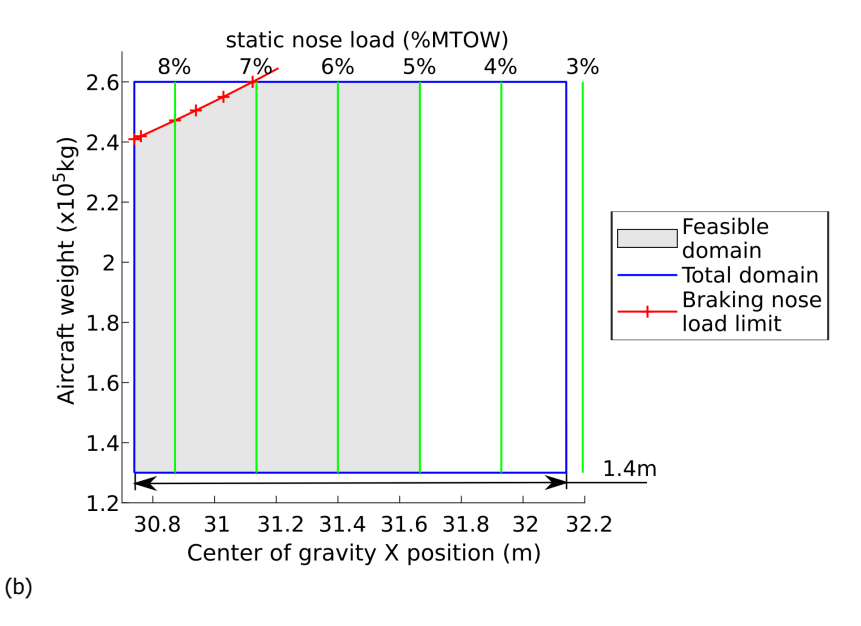


Figure 5.5: Weight-cg diagram focused on nose load limits for (a) default configuration, and (b) floor 5.5 configuration

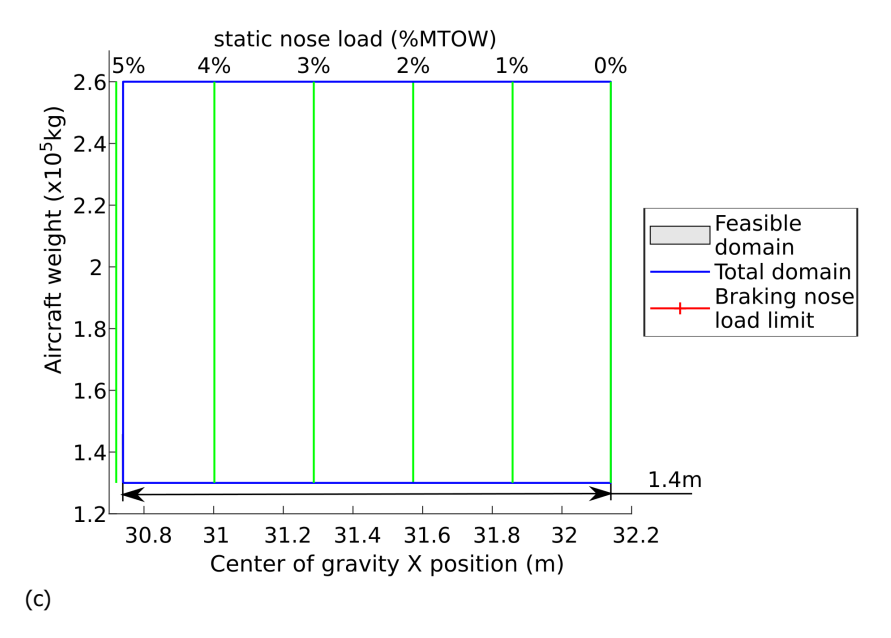


Figure 5.5: (continued) Weight-cg diagram focused on nose load limits for (c) max dihedral configuration

	Default	Floor 5.5	Max dihedral
Brace airframe attachment (m)	$ \begin{cases} 30.4 \\ 5.73 \\ -0.658 \end{cases} $	$ \begin{cases} 30.2 \\ 5.65 \\ -0.658 \end{cases} $	N/A
Brace length (m)	2.72	2.58	N/A

Table 5.6: Main gear braces position and length

Final gear positions

The main and nose gear are kept at the positions given in Tables 5.4 and 5.5, and the outrigger can be chosen between the two options in Table 5.2. The gear and both outrigger options are shown with the Flying V airframe in Figure 5.6.

The second outrigger option seems better despite touching the ground outside of runway in case of lateral deviation, because it allows to reach the landing incidence of 17° without having the outrigger touching the ground (see longitudinal cut on Figure 5.6). This would allow limited cross-wind landing without the outrigger contacting the ground, thus reducing stresses and maintenance on the outrigger.

Final kinematics

The required folded volume for main gear determined in 5.3.2 cannot fit within the airframe while outside of passenger cabin, thus a fairing is needed. To minimize the fairing size, the folded bogie is aligned with the fuselage direction with vertical wheel axes, and placed as close as possible to the passenger cabin to use the thicker airframe part. This leads to making a cut in the oval fuselage (see bottom view of Figure 5.6) to use the space between passenger cabin and the oval fuselage. To obtain vertical wheel axles without adding a pivot point to the strut, the main gear vertical position is lowered such that when folded, the strut is horizontal. This gives the vertical gear position used in Table 5.4.

With the vertical position chosen above, the main gear strut is outside of the airframe, thus needs to be covered by a fairing. Considering the length of main gear strut of default and floor 5.5 configurations (see Table 5.4), the alternative kinematics discussed in 3.10.4 are used to minimize the fairing width. It is chosen to bring the folded bogie of these configurations at the same location as the max dihedral configuration, giving upper strut length of 1.69 m and 1.33 m respectively for default and floor 5.5 configurations.

The axes are computed and the braces are positioned as in Table 5.6, using a brace attached along the strut 0.4 m below the strut folding point. No brace is computed for the max dihedral configuration since it is only needed for the alternative kinematics.

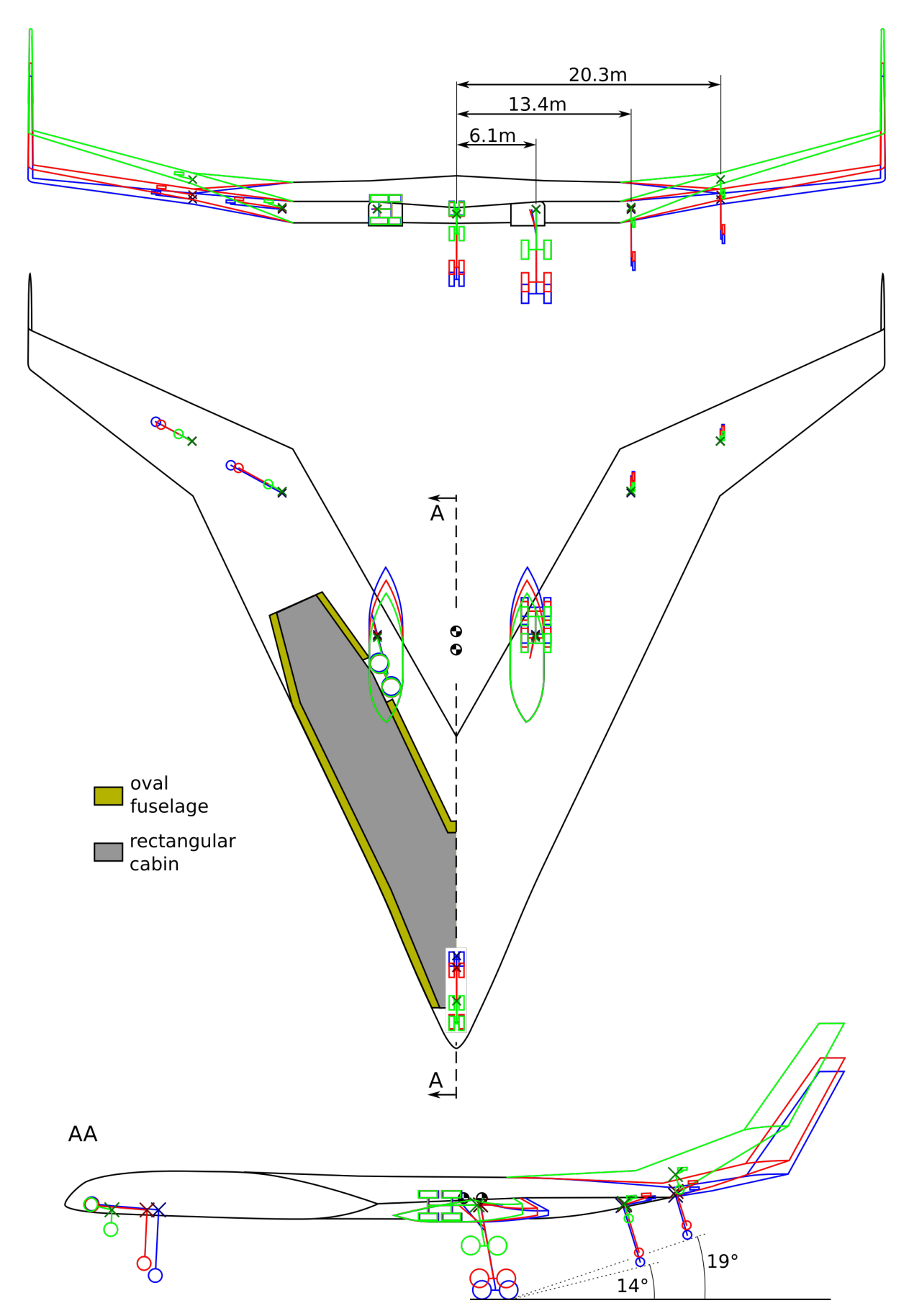


Figure 5.6: Flying V landing gear along with airframe from rear view, bottom view, and longitudinal cut view (default configuration in blue, floor 5.5 in red, max dihedral in green)

The folded and deployed gear positions are shown on Figure 5.6, respectively on the left and right parts for improved readability. Both are superimposed on the longitudinal cut as it shows only half of the airframe. Figure 5.7 provides a 3D view with a partially folded position, outlining the different kinematics concepts used.

The nose gear axis is the y-axis, giving the kinematics shown in Figure 5.6. The nose shape is absent from the ParaPy model, and was assumed from Figure 5.4 to have its nose at x = 0 m.

Final fairing

With the defined kinematics, a fairing can be added on each configuration, with a design similar to that of Savoni and Rudnik [54]. The fairings are also shown in Figure 5.6, where the alternate kinematics allow to keep the fairing width similar for all configuration, despite the vast change in strut length.

5.4. Evaluation of the figures of merit

The gear is now designed and can be used to compute the figure of merits.

5.4.1. Gear weight

The gear weight is computed with Equations 3.39 and 3.40, providing the values in Table 5.7. Using Equations 3.41 and 3.42 the stall speed and maximum landing weight are respectively $58.6 \,\text{m/s}$ and $208 \,\text{t}$.

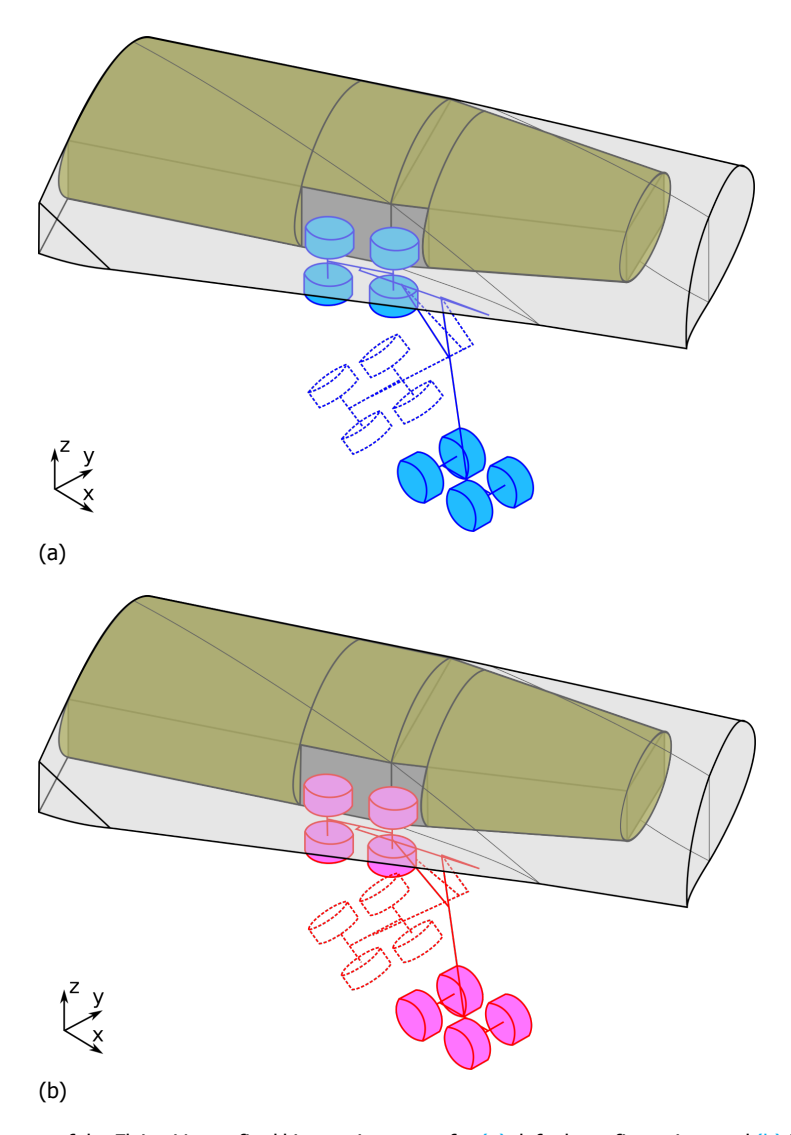


Figure 5.7: Folding process of the Flying V gear final kinematics setup, for (a) default configuration, and (b) floor 5.5 configuration

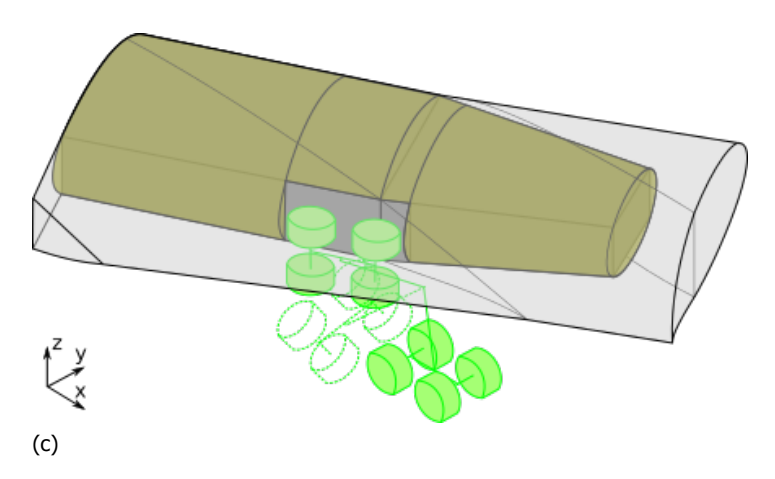


Figure 5.7: (continued) Isometric view of Flying V gear folding process, for (c) max dihedral configuration

	Default	Floor 5.5	Max dihedral
Main gear weight (t)	8.95	8.50	6.44
Nose gear weight (t)	1.28	1.16	0.58
Total gear weight (t)	10.2	9.66	7.02

Table 5.7: Gear weight estimation for the different configurations

The underestimation pointed in 4.3 leads to add about $2.6\,t$ to the total weight ($1\,\%$ of $260\,t$ maximum take-off weight). With no indication if a gear is more underestimated than another, this increase is distributed on main and nose gear while keeping the weight ratio between the two constant. The corrected weights are in Table 5.8.

Since the gear struts are quite long, they end up being heavy. When validating the gear weight estimation method, Heerens [19] uses the DC10-10 gear weight, given to be 9.6 t. The gear designed for the A350-900 in 4.1 has a corrected weight of 10.8 t using Raymers formulas (see 3.11.1) and the correction determined in 4.3. While the DC10-10 is lighter than the Flying V, the A350-900 is heavier and lands at the same speed thus gear length is the main reason for the 20 % heavier gear on the Flying V compared to similar size airliners.

5.4.2. Ground manoeuvring

The track and the wheelbase of each configuration are listed in Table 5.9 and compared with the A350-900. All Flying V configurations have lower or equal values of these parameters than the A350-900. Thus at constant steering angle, the nose gear and outer main wheel turning radii are expected to be smaller. However the differences in airframe geometry, particularly a wing tip further away from the gear, lead to expect a larger wing tip turning radius. The same turning radii as computed in Annex A are computed for the Flying V and are given in Tables B.1 and B.2 in Annex B.

A more interesting aspect than the raw data in Tables B.1 and B.2 is to compare with existing aircraft of similar gear characteristics. The A350-900 is closest to the max dihedral configuration, while the Boeing 777-200 is closest to the default dihedral. The comparisons are provided in Annex B, in Tables B.3 and B.4 for the default configuration, and in Tables B.5 and B.6 for the max dihedral configuration.

Nose wheel and outer main wheel turning radii computed for the Flying V decrease quicker with increasing steering angle than the turning radii of the existing aircraft used as reference. This trend is

	Default	Floor 5.5	Max dihedral
Main gear weight (t)	11.2	10.8	8.83
Nose gear weight (t)	1.61	1.47	0.79
Total gear weight (t)	12.8	12.3	9.62

Table 5.8: Corrected gear weight estimation for the different configurations

	Default	Floor 5.5	Max dihedral	A350-900
Gear track (m)	12.2	12.2	12.2	10.6
Gear wheelbase (m)	26.0	26.5	28.4	28.7

Table 5.9: Gear characteristics relevant for ground manoeuvring for Flying V along with A350-900 data

Cabin floor height	Default	Floor 5.5	Max dihedral
Fwd cabin (m)	4.69-5.03	3.80-4.14	1.34-1.68
Aft cabin (m)	6.05-6.39	5.17-5.50	2.71-3.04

Table 5.10: Cabin floor height for the different configurations

similar to what was observed in 4.6 when validating the turning radii, and of similar variation range. Thus it can be considered that these radii vary in reality like those of the reference aircraft. Since the gear track and wheelbase are close to those of the reference aircraft (777-200 for default dihedral, A350-900 for max dihedral), similar ability to manoeuvre on taxiways and parking can be expected from the Flying V.

The variation is different for the airframe, particularly for the wing tip which turning radii decrease slower than those of the reference aircraft: from 7.6 % higher at smallest steering angle to 15.8 % higher at largest steering angle. For the airframe nose, the variation is more limited, and almost similar to the Boeing 777-200 for the default configuration. This means that the Flying V airframe will have consistently larger turning radii than A350-900 or Boeing 777-200, not reducing as fast when increasing steering angle. This was to be expected since the airframe is different, with wing tip further away from the gear, and may raise issues with airport buildings.

5.4.3. Cabin floor height

The cabin floor height is computed in Table 5.10. Two values are given since the -3° pitch angle at rest leads to the fwd cabin being lower than the aft cabin. The uncertainty given on each is due to the lack of precision on shock absorber stroke computation, as discussed in 4.2.

It can be noted that the negative pitch angle at rest makes all configuration have the front doors below the 5.5 m limit that was chosen to define the floor 5.5 configuration for ground handling compatibility. However this does not mean that ground handling issue will not occur with the default configuration. The aft part of the cabin is higher than this limit, while it is often used to access the cabin without conflicting with the passengers leaving or entering from the front doors. The aft part of the cabin is also considered for placing the cargo or the passengers luggage, thus will require to be accessed. Such issue is solved on the floor 5.5 configuration with the aft part of the cabin being at most at 5.5 m from the ground.

While cabin will be accessible, the lower part of the airframe will still be far from the ground. This makes fuel loading less practical, and external power supply or external air conditioning harder to connect, while the latter are now common practice for most aircraft to avoid using engine power.

5.4.4. Rotation ability

Rotation ability was computed in 5.3.5, with Figure 5.3. The final gear position used is in between the two most forward position tested on the curves. Thus zero pitching moment can be reached without approaching control surface saturation both during take-off for pitch-up, and during landing to counter the weight induced pitch-up moment.

5.4.5. Fairing drag

The formulas from 3.11.4 are applied to the fairing designed. The following constants are used:

- $k_{\rm roughness}=6.248\times 10^{-6}\,{\rm m}$ for smooth paint [11] which is the expected surface finish for the Flying V.
- 0 = 1.5 as the fairing is mounted directly on the wing [11].

The zero-lift drag characteristics of the fairing presented in 5.3.7 and in Figure 5.6 are evaluated

	Default	Floor 5.5	Max dihedral
Wetted surface (m ²)	55.8	48.6	41.9
Characteristic length (m)	11.9	10.8	9.8
Maximal frontal area (m ²)	4.22	3.99	3.67
Zero-lift drag coefficient($\times 10^{-4}$)	2 (max. 3)	1.5 (max. 2.5)	1 (max. 2)

Table 5.11: Zero-lift drag of the fairing for each configuration

	Default	Floor 5.5	Max dihedral
Y_v airliner	-0.688	-0.688	-0.688
Y_v Flying V, landing	-0.240	-0.246	-0.267
Y_{ν} Flying V, landing, corrected	-0.660	-0.676	-0.734
delta w.r.t. airliner	4.1 %	1.7 %	6.8 %

Table 5.12: Comparison of sideforce derivative due to sideslip with a conventional airliner [70]

in Table 5.11. The flow is assumed to be fully turbulent, based on the aft position of the fairing and the high Reynolds number of the flow over the Flying V. The values presented are for one fairing, and thus should be doubled for the full influence on aircraft drag. The overestimating value according to Raymer (computed with classical Reynolds number, see 3.11.4) is kept to provide an upper limit as no validation was performed on this formula.

The high strut length of default and floor 5.5 configurations requires longer fairings (21% longer for default than for max dihedral), thus with larger wetted surface (15% larger for default than for max dihedral). This explains the larger zero-lift drag coefficient observed. It is reminded that interference drag is not included as it would require a CFD simulation of the full aircraft.

5.4.6. Stability derivatives

To compute the stability derivatives for the Flying V the following assumptions are made:

- The nacelle leading edge has the same longitudinal and lateral position as the gear root, and its dimensions are taken from [7].
- The fake body required for Y_v and N_v spans until trailing edge kink, and has the root profile as side view shape.
- The centre of gravity is at the middle of its range, at $x_{cg} = 31.4 \,\mathrm{m}$.

Derivatives are computed for take-off, landing and cruise phase, but except for L_v the take-off phase is neglected because too close to the landing phase. The evolution of each derivative with dihedral increase is presented graphically, then the low speed phases are compared to conventional airliner data from Morgan and Paulson [70]. The comparison requires to rescale the Flying V coefficients that are 2.75 times too small due to the much larger reference area of the Flying V compared to the airliner used for the comparison.

Morgan and Paulson is exclusively for low speed phases leaving high speed phases without a reference. It was not considered to check the high speed phases since there are already issues to point with the low speed phases as shown below.

Sideforce derivative due to sideslip, Y_{ν}

Figure 5.8a shows that Y_{ν} increases with dihedral increase, but proportionally less in cruise than at landing. Increasing Y_{ν} improves Dutch-roll damping, but reduces aircraft manoeuvrability [67]. Therefore usually a compromise between the two is chosen, with moderate values of Y_{ν} . Compared with reference airliner in Table 5.12, the Flying V has similar stability derivatives. The variations due to dihedral change are small with at most 6.8 % deviation compared to airliner.

Rolling moment derivative due to sideslip, L_v

Figure 5.8b shows that L_v increases as well with increasing dihedral, with the largest increase for cruise phase. Such variation was expected as L_v is often called dihedral effect, thus expected to vary

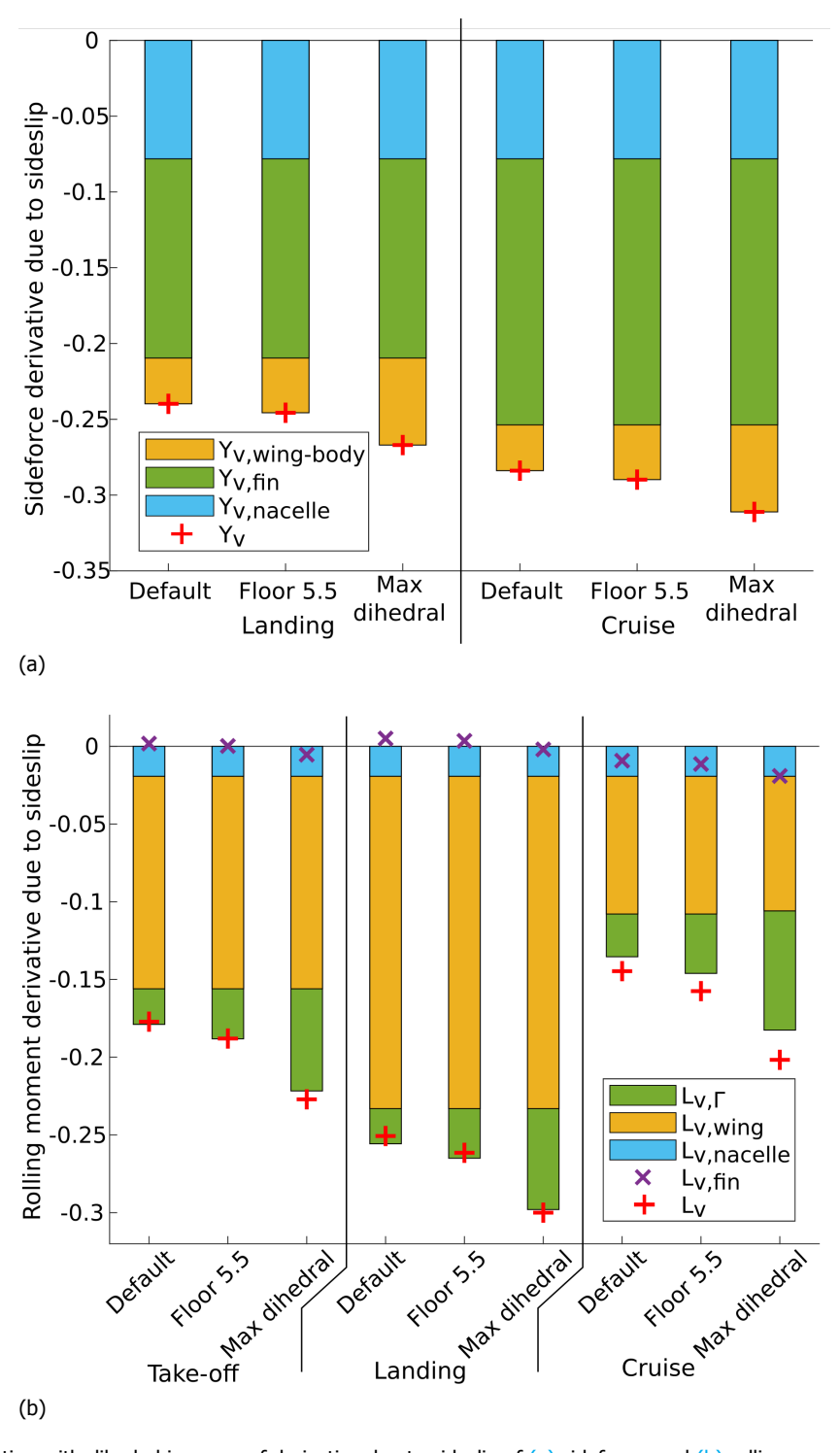


Figure 5.8: Evolution with dihedral increase of derivative due to sideslip of (a) sideforce, and (b) rolling moment

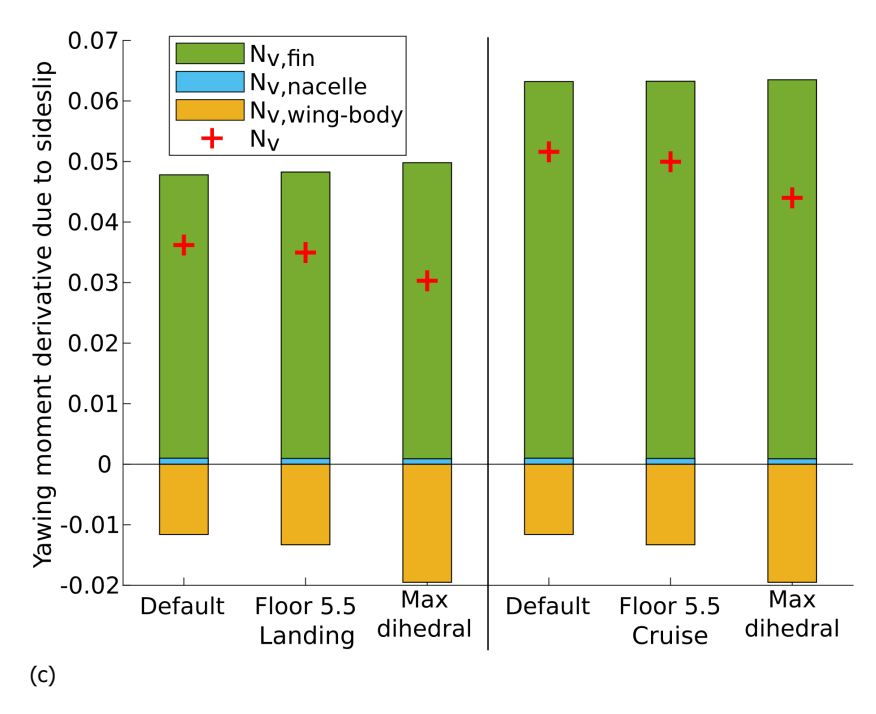


Figure 5.8: (continued) Evolution with dihedral increase of derivative due to sideslip of (c) yawing moment

	Default	Floor 5.5	Max dihedral
L_v airliner	-0.229	-0.229	-0.229
L_v Flying V, take-off	-0.177	-0.188	-0.227
L_v Flying V, take-off, corrected	-0.487	-0.517	-0.625
delta w.r.t. airliner	113 %	126 %	173 %
L_v Flying V, landing	-0.251	-0.262	-0.300
L_{v} Flying V, landing, corrected	-0.689	-0.719	-0.825
delta w.r.t. airliner	201 %	214 %	260 %

Table 5.13: Comparison of rolling moment derivative due to sideslip with a conventional airliner [70]

almost directly with dihedral angle. Large negative values of L_v are beneficial for spiral stability, but detrimental to Dutch-roll damping [67]. Compared to the airliner in Table 5.13, the Flying V has large negative values of L_v , up to 3.6 times larger than the airliner. However most often Dutch-roll damping is prioritized over spiral stability, thus the increase observed seems detrimental for the Flying V.

Yawing moment derivative due to sideslip, N_v

Figure 5.8c shows that increasing dihedral brings smaller positive N_v values. N_v affects Dutch-roll natural frequency and spiral stability, and large positive values are wanted [67]. The decrease observed is thus not very interesting, even if the larger errors on N_v computation (see 4.5.2) could also be responsible for this decrease. The Flying V is at best at 72.4% of the reference airliner, decreasing with dihedral increase. According to Figure 5.8c, the decrease is due to the wing-body component, while increasing the dihedral increases the equivalent vertical surface aft of the centre of gravity (see Figure 5.6), thus should increase N_v instead of decreasing it. The decrease is however coherent with the ESDU statement [37] that the wing-body component is destabilising.

Considering that in 4.5.2, ESDU formula were only able to capture the value of N_{ν} around 6° incidence, it can be expected that values in cruise will be more positive than what is shown in Figure 5.8c. On the other hand, take-off at 13° and even more landing at 17° will be less positive, which is undesirable.

	Default	Floor 5.5	Max dihedral
N_v airliner	0.138	0.138	0.138
N_v Flying V, landing	0.0362	0.0350	0.0303
N_{ν} Flying V, landing, corrected	0.0996	0.0963	0.0833
delta w.r.t. airliner	27.6 %	30 %	39.4 %

Table 5.14: Comparison of yawing moment derivative due to sideslip with a conventional airliner [70]

5.5. Discussion

The gear that can be fitted on the initial Flying V configuration is longer, thus heavier than similarly sized aircraft (about 20% more than the A350-900). If the initial weight estimation used (taken from [4]) was based on the same gear weight fraction as on similarly sized aircraft, then either the payload will decrease to keep the same maximum weight, or the overall weight will increase with an influence on gear itself. In addition to requiring different ground handling due to the V-shaped fuselage that constrains access to only one side of each fuselage, the initial Flying V would also be higher from the ground than any existing aircraft. Moreover the height is derived from ideal lift curves, which may prove to be unreachable, thus the situation described may be optimistic.

Being able to bring shorter thus lighter gear, requiring smaller fairing to fit, and making the aircraft closer to the ground, the dihedral increase could have been the ideal solution. Despite a slightly larger ground turning radii that makes max dihedral configuration similar to the A350-900 (except for wing tip), gear weight is decreased by 25 %, cabin floor height by 52 to 67 % and fairing zero-lift drag by about 33 %. The gear kinematics are also much simpler due to the lower length, and maintenance is made easier due to lower height from ground. However there is a major issue: the stability derivatives were already not very good on the initial Flying V, and increasing dihedral only worsened the problem, particularly on Dutch-roll. The large increase of rolling moment due to sideslip, known for its influence on Dutch-roll stability, could bring unstable Dutch-roll, meaning either discarding the configuration, or having to create an artificial stability system with sufficient reliability to satisfy certification authorities.

There is therefore a trade-off to make between on one side gear weight and easiness to operate and maintain due to low height from ground, and on the other side acceptable flying qualities.

6

Synthesis

6.1. Conclusion

Landing gear design methods are available from the literature, and need to be adapted to the requirements of the Flying V. Since they offer a sequential organisation in which dependencies between the different design disciplines have been accounted for, automatic gear design procedures are a good starting point. However the Flying V is a different configuration from those covered in literature in which the dependencies between disciplines are not fully known, therefore using an optimiser risks overlooking some interactions. Literature also points that including some low level verifications (such as tipover, or gear loading) within the design methods reduces the amount of iterations and improves the output.

Automatic design procedures relying on optimisers set quantifiable figures of merit to evaluate the design produced. Some of these figures of merit are also relevant if no optimiser is used. The following set is chosen for the Flying V: the gear weight, the ground manoeuvring capability, the fairing zero-lift drag, the cabin floor height from ground, the rotation ability and lateral stability derivatives. The first three come directly from existing design methods, while the last three are added after an exploratory study is conducted before designing the gear to understand some disciplines interactions specific to the Flying V. This study pointed the need of a long gear, making the aircraft high from the ground thus hard to reach for airline operation or maintenance, hence checking cabin floor height. To shorten the gear, this study suggested moving the gear aft or increasing dihedral. The former lowers pitch control moment arm thus impairs rotation ability, and the latter modifies the aircraft reaction to external disturbances, i.e. its stability derivatives. While used for evaluation in some sources, flotation was neglected since other sources offered a method to chose the bogie and tires beforehand, quaranteeing acceptable flotation without the need to evaluate it.

These figures of merit are computed using empirical methods, or geometry when computing distances, angles or surfaces. These methods were chosen because they are simple to implement and quick to perform. This allows easier iterations when the design method requires it, or if there are changes in the configuration or the requirements. In addition, only sideslip induced stability derivatives are computed as the literature supporting their computation stated they were the most important to know. The price to pay for simple and quick methods is the lower precision compared to higher order methods, particularly obvious on the sideslip induced stability derivatives evaluation. Validation shows that only the sideforce derivative is accurate, while rolling and yawing moments display errors higher than 50 % in the range of interest. For the other figures of merit, validation provided corrections which brings the figures of merit to an acceptable precision considering that the gear design is still in a preliminary phase.

By showing the influence of dihedral, the exploratory study led to design three different gear, for three different airframes with different dihedral angles: the initial airframe, another with dihedral such that cabin floor is at 5.5 m from ground ("floor 5.5"), and the last with dihedral such that the gear is the shortest ("max dihedral"). Tricycle gear was chosen for its superior ground handling capabilities, and the A350-900 bogies and tires were reused to guarantee a similar flotation due to the Flying V lower estimated weight. Their large size however prevents them from fitting in the Flying V thin airframe,

requiring a fairing which size is minimised by bringing the folded bogie as close as possible to the cabin through a cut in the oval fuselage. A more compact folded gear also reduces fairing size, which was achieved by two means: modifying the kinematics and shortening the gear. The kinematics are modified by folding the main strut in an upper and lower strut, increasing its compactness when folded. The gear is shortened through an actuated tilting bogie and using an outrigger. The former raises the aircraft from the ground at high incidence thus allowing a shorter gear for the same ground margin, while the latter alleviates the length constraint on main gear by guaranteeing the wing tip ground margin (critical as it holds the vertical surface). The bogie-tilting actuator proved also useful to lock the bogie during push-back, improving stability w.r.t. inertia effects thus allowing to move the gear forward to increase pitch control moment arm.

The gear of the default configuration places the cabin between 5 and 6 m for an estimated weight of $12.8\,t$. Ground manoeuvring and rotation ability are acceptable, and fairing zero-lift drag is low. The stability derivatives are acceptable except for roll moment derivative due to sideslip which is quite high. Increasing dihedral to obtain "floor 5.5" (resp. "max dihedral") configuration reduces the cabin height by $12\,\%$ (resp. $56\,\%$), reduces gear weight by $4\,\%$ (resp. $25\,\%$) and reduces fairing drag by $25\,\%$ (resp. $50\,\%$). Ground manoeuvring and rotation ability are negligibly modified by dihedral increase. However roll moment derivative due to sideslip increases further, sideforce derivative stays constant while yaw moment derivative decreases. The latter is surprising since dihedral variation increase the vertical surface aft of the centre of gravity, thus should increase the yawing moment. However the literature supporting the formulas states that wing and body have a destabilising effect, thus should make it decrease. This phenomena could not be investigated further.

In the initial configuration, the aircraft is higher than existing aircraft of similar size by about $10\,\%$, with a gear $20\,\%$ heavier, and possibly more since the outrigger could not be included in the weight estimation. The dihedral increase brings the Flying V closer to existing aircraft of similar size, with still a heavier gear since the thinner airframe means a longer gear for the same cabin floor height. Ground manoeuvring is very close to that of the A350-900 except for a significantly larger wing tip turning radius due to the airframe difference. The rotation ability used could not be compared to existing aircraft for lack of data. Comparing stability derivatives with an existing airliner confirmed that rolling moment derivative due to sideslip is very high with up to 3.5 times the existing airliner value. The two other stability derivatives are closer to the reference airliner values.

This allows to answer the research question. On the original Flying V configuration, adding a landing gear makes operation and maintenance harder by raising the aircraft from the ground, and reduces the available payload at constant maximum weight because of the high gear weight. Changing the airframe dihedral to reduce gear length and weight leads to a large modification of the stability derivatives that brings the aircraft away from desired flight dynamics. The other figures of merit that were observed to investigate the gear influence on the Flying V are only slightly modified by the dihedral change and are acceptable for all dihedral values.

6.2. Limitations and future work suggestion

There are however aspects that could not be covered, or that were covered insufficiently in this work, thus limiting it and pointing directions in which it could be improved.

In this study, gear weight is empirically computed and neglects the outrigger. The former comes from the simplicity of empirical formulas, and the latter from finding no empirical formula for outrigger weight. However as it was shown when validating the formula, empirical methods are not very accurate. In addition the gear seems to be significantly heavier than similarly sized aircraft, thus a more accurate estimation of gear weight would allow to determine more precisely by how much the payload would be reduced by the increased gear weight. This could be obtained with an analytical weight estimation, coupled with a new structure sizing study to investigate as well the influence of a heavy gear on structure. This structure study would also allow to investigate the option suggested by Rubio-Pascual and reused here of having the engine placed atop the gear to share structures and possibly gain weight.

Stability derivatives are also computed with empirical relations and proved to not be very precise, however they are the main reason why increasing the dihedral on the Flying V seems not very interesting. While it is not expected that a more accurate study would show that increasing dihedral leads to improved stability derivatives, it could evaluate more precisely the penalty obtained by increasing the dihedral. This would allow for a better supported choice concerning the dihedral used on the Flying V

in the future.

Finally, rotation ability was one of the key factors in placing the gear as fwd as it has been positioned here. Such position led to having insufficient nose gear loading over the whole centre of gravity range on the max dihedral configuration. A dynamic study determining the pitch rate achievable by the Flying V in a given configuration, and comparing it with regulation or general operation requirements, would determine if the gear really needs to be this much fwd, or if it can be moved aft, increasing nose gear loading. Such study could also investigate the aerodynamic effect of nacelle on pitch rate, neglected in this work.



Turning radius validation data

A.1. A350-900

steering		Nose wheel		Outer main wheel		
angle (°)	real (m)	computed (m)	delta	real (m)	computed (m)	delta
20	86	83.8	-2.56%	86.9	85.2	-1.99%
25	69.6	67.8	-2.56%	69.3	67.9	-2.03%
30	58.9	57.3	-2.68%	57.3	56.1	-2.15%
35	51.5	50.0	-2.98%	48.6	47.4	-2.55%
40	45.9	44.6	-2.86%	41.7	40.6	-2.67%
45	41.8	40.5	-3.04%	36.3	35.1	-3.33%
50	38.6	37.4	-3.08%	31.7	30.5	-3.85%
55	36.2	35.0	-3.35%	28	26.5	-5.36%
60	34.3	33.1	-3.52%	24.7	23.0	-6.98%
65	32.9	31.6	-3.88%	22	19.8	-10.0%
70	31.9	30.5	-4.39%	19.8	16.9	-14.8%
72	31.6	30.1	-4.64%	19.1	15.7	-17.6%

Table A.1: Comparison of computed and real turning radii on A350-900, part 1 (real values from [47])

steering		Wing tip			Airframe nose	
angle (°)	real (m)	computed (m)	delta	real (m)	computed (m)	delta
20	113.6	112	-1.48%	87.1	85.5	-1.85%
25	96.2	94.8	-1.47%	71.2	69.9	-1.83%
30	84.3	83.1	-1.42%	60.8	59.8	-1.69%
35	75.7	74.5	-1.56%	53.7	52.8	-1.75%
40	68.9	67.9	-1.50%	48.5	47.7	-1.66%
45	63.7	62.5	-1.91%	44.7	43.9	-1.73%
50	59.2	58.0	-2.04%	41.8	41.1	-1.75%
55	55.5	54.1	-2.48%	39.6	38.9	-1.84%
60	52.4	50.7	-3.20%	38	37.2	-2.17%
65	49.8	47.7	-4.30%	36.7	35.9	-2.25%
70	47.7	44.9	-5.97%	35.9	34.9	-2.82%
72	47	43.8	-6.84%	35.6	34.6	-2.90%

Table A.2: Comparison of computed and real turning radii on A350-900, part 2 (real values from [47])

A.2. B777-200

steering		Nose wheel			Outer main wheel		
angle (°)	real (m)	computed (m)	delta	real (m)	computed (m)	delta	
30	51.3	51.7	0.90%	50.3	50.3	0.02%	
35	44.8	45.1	0.72%	42.6	42.5	-0.36%	
40	40	40.3	0.66%	36.6	36.3	-0.74%	
45	36.4	36.6	0.55%	31.7	31.4	-1.06%	
50	33.7	33.8	0.25%	27.7	27.2	-1.80%	
55	31.5	31.6	0.30%	24.1	23.6	-2.05%	
60	29.9	29.9	-0.05%	21	20.4	-2.73%	
65	28.6	28.6	-0.16%	18.2	17.6	-3.55%	
70	27.6	27.5	-0.21%	15.6	14.9	-4.46%	

Table A.3: Comparison of computed and real turning radii on B777-200, part 1 (real values from [48])

steering		Wing tip			Airframe nose	
angle (°)	real (m)	computed (m)	delta	real (m)	computed (m)	delta
30	75.3	76.0	0.92%	53.8	54.9	2.12%
35	67.6	68.2	0.90%	47.8	48.7	1.96%
40	61.7	62.2	0.75%	43.4	44.3	2.02%
45	56.9	57.3	0.66%	40.2	41.0	1.93%
50	52.9	53.2	0.54%	37.7	38.5	2.08%
55	49.5	49.7	0.33%	35.8	36.6	2.16%
60	46.5	46.6	0.13%	34.4	35.1	2.06%
65	43.7	43.8	0.14%	33.3	34.0	2.06%
70	41.2	41.2	-0.02%	32.5	33.1	1.96%

Table A.4: Comparison of computed and real turning radii on B777-200, part 2 (real values from [48])

B

Flying V turning radii

B.1. Turning radii raw data

steering	Nose wheel			Outer main wheel		
angle (°)	Default (m)	Floor 5.5 (m)	Max dihedral (m)	Default (m)	Floor 5.5 (m)	Max dihedral (m)
20	76.4	77.9	83.4	77.9	79.3	84.5
25	61.8	63.1	67.5	62.1	63.3	67.3
30	52.2	53.3	57.0	51.3	52.3	55.5
35	45.5	46.5	49.7	43.4	44.2	46.8
40	40.6	41.5	44.4	37.2	37.9	40.1
45	36.9	37.7	40.3	32.2	32.8	34.6
50	34.1	34.8	37.2	28.0	28.5	30.0
55	31.9	32.5	34.8	24.4	24.8	26.1
60	30.2	30.8	32.9	21.2	21.5	22.6
65	28.8	29.4	31.5	18.3	18.5	19.4
70	27.8	28.4	30.4	15.6	15.8	16.5
72	27.5	28.0	30.0	14.6	14.8	15.4

Table B.1: Turning radii of the Flying V, part 1

steering		Wing tip			Airframe nose		
angle (°)	Default (m)	Floor 5.5 (m)	Max dihedral (m)	Default (m)	Floor 5.5 (m)	Max dihedral (m)	
20	107	108	114	79.1	80.3	84.7	
25	91.5	92.7	96.8	65.1	66.0	69.1	
30	81.1	82.0	85.4	56.1	56.7	58.9	
35	73.5	74.3	77.1	49.9	50.4	51.9	
40	67.6	68.3	70.7	45.5	45.8	46.8	
45	62.9	63.5	65.5	42.2	42.4	43.0	
50	59.0	59.5	61.3	39.8	39.9	40.1	
55	55.7	56.1	57.6	37.9	37.9	37.8	
60	52.7	53.1	54.4	36.5	36.4	36.1	
65	50.1	50.4	51.6	35.4	35.2	34.8	
70	47.7	48.0	49.0	34.5	34.4	33.8	
72	46.8	47.1	48.0	34.3	34.1	33.5	

Table B.2: Turning radii of the Flying V, part 2

B.2. Comparison with existing aircraft

B.2.1. Default configuration vs. Boeing 777-200

steering	Nose wheel			Outer main wheel		
angle (°)	B777-200 (m)	Default (m)	delta	B777-200 (m)	Default (m)	delta
30	51.3	52.2	1.83 %	50.3	51.3	2.06 %
35	44.8	45.5	1.64 %	42.6	43.4	1.88 %
40	40	40.6	1.58 %	36.6	37.2	1.71 %
45	36.4	36.9	1.48 %	31.7	32.2	1.64 %
50	33.7	34.1	1.17 %	27.7	28.0	1.14 %
55	31.5	31.9	1.22 %	24.1	24.4	1.20 %
60	29.9	30.2	0.87 %	21	21.2	0.85 %
65	28.6	28.8	0.76 %	18.2	18.3	0.44 %
70	27.6	27.8	0.71 %	15.6	15.6	0.04 %

Table B.3: Comparison of Flying V default configuration turning radii with Boeing 777-200

steering	Wing tip		Airframe nose			
angle (°)	B777-200 (m)	Default (m)	delta	B777-200 (m)	Default (m)	delta
30	75.3	81.1	7.69 %	53.8	56.1	4.31 %
35	67.6	73.5	8.71 %	47.8	49.9	4.48 %
40	61.7	67.6	9.61 %	43.4	45.5	4.87 %
45	56.9	62.9	10.6 %	40.2	42.3	5.09 %
50	52.9	59.0	11.5 %	37.7	39.8	5.54 %
55	49.5	55.7	12.4 %	35.8	37.9	5.89 %
60	46.5	52.7	13.4 %	34.4	36.5	6.02 %
65	43.7	50.1	14.7 %	33.3	35.4	6.22 %
70	41.2	47.7	15.9 %	32.5	34.5	6.28 %

Table B.4: Comparison of Flying V default configuration turning radii with Boeing 777-200, part 2

B.2.2. Max dihedral configuration vs. Airbus A350-900

steering		Nose wheel		Λ	uter main wheel	
_	13E0 000 (m)		dolta			dolta
angle (°)	A350-900 (m)	Max dihedral (m)	delta	A350-900 (m)	Max dihedral (m)	delta
20	86	83.4	-3.03 %	86.9	84.5	-2.80 %
25	69.6	67.5	-3.03 %	69.3	67.3	-2.93 %
30	58.9	57.1	-3.15%	57.3	55.5	-3.13%
35	51.5	49.7	-3.44 %	48.6	46.8	-3.63 %
40	45.9	44.4	-3.32%	41.7	40.1	-3.85%
45	41.8	40.3	-3.50 %	36.3	34.6	-4.62 %
50	38.6	37.2	-3.54%	31.7	30.0	-5.25%
55	36.2	34.8	-3.81%	28	26.1	-6.88%
60	34.3	32.9	-3.98%	24.7	22.6	-8.63 %
65	32.9	31.5	-4.34 %	22	19.4	-11.8%
70	31.9	30.4	-4.85%	19.8	16.5	-16.8%
72	31.6	30.0	-5.09 %	19.1	15.4	−19.5 %

 $\label{thm:comparison} \textbf{Table B.5: Comparison of Flying V max dihedral configuration turning radii with Airbus A350-900 } \\$

steering		Wing tip			Airframe nose	
angle (°)	A350-900 (m)	Max dihedral (m)	delta	A350-900 (m)	Max dihedral (m)	delta
20	114	114	0 %	87.1	84.7	-2.75 %
25	96.2	96.8	0.58 %	71.2	69.1	-2.95 %
30	84.3	85.4	1.29 %	60.8	58.9	-3.05%
35	75.7	77.1	1.83 %	53.7	51.9	-3.37%
40	68.9	70.7	2.59 %	48.5	46.8	-3.53%
45	63.7	65.5	2.89 %	44.7	43.0	-3.85%
50	59.2	61.3	3.50 %	41.8	40.1	-4.12%
55	55.5	57.6	3.83 %	39.6	37.9	-4.43 %
60	52.4	54.4	3.89 %	38	36.1	-4.95 %
65	49.8	51.6	3.60 %	36.7	34.8	-5.20%
70	47.7	49.0	2.73 %	35.9	33.8	-5.90 %
72	47	48.0	2.18 %	35.6	33.5	−6.02 %

Table B.6: Comparison of Flying V max dihedral configuration turning radii with Airbus A350-900, part 2

Bibliography

- [1] J. Benad, *The Flying V A new Aircraft Configuration for Commercial Passenger Transport*, Tech. Rep. (Deutsche Gesellschaft für Luft- und Raumfahrt Lilienthal-Oberth e.V., Bonn, 2015).
- [2] F. Faggiano, Aerodynamic Design Optimization of a Flying V Aircraft, Msc thesis, Delft University of Technology, Delft (2016).
- [3] F. Faggiano, R. Vos, M. Baan, and R. Van Dijk, *Aerodynamic Design of a Flying V Aircraft*, in *17th AIAA Aviation Technology, Integration, and Operations Conference* (American Institute of Aeronautics and Astronautics, 2017).
- [4] L. van der Schaft, *Development, Model Generation and Analysis of a Flying V Structure Concept,* Msc thesis, Delft University of Technology (2017).
- [5] M. Hoogreef, *The Oval Fuselage: A New Structural Design Concept for Blended Wing Body Cabins*, (2012).
- [6] ParaPy B.V., ParaPy Knowledge Based Engineering Platform, (2017).
- [7] B. Rubio Pascual, *Engine-Airframe Integration for the Flying V*, Msc thesis, Delft University of Technology (2018).
- [8] M. Palermo, *The Longitudinal Static Stability and Control Characteristics of a Flying V Scaled Model*, Msc thesis, Delft University of Technology (2019).
- [9] R. Viet, Analysis of the flight characteristics of a highly swept cranked flying wing by means of an experimental test, Msc thesis, Delft University of Technology (2019).
- [10] A. Ruiz Garcia, Aerodynamic Model Identification of the Flying V using Wind Tunnel Data, Msc thesis, Delft University of Technology (2019).
- [11] D. P. Raymer, *Aircraft design: a conceptual approach* (American Institute of Aeronautics and Astronautics, Reston, VA:, 2012) p. 1044.
- [12] E. Torenbeek, Synthesis of subsonic airplane design: an introduction to the preliminary design, of subsonic general aviation and transport aircraft, with emphasis on layout, aerodynamic design, propulsion, and performance (Delft University Press, Dordrecht, 1982).
- [13] J. Roskam, Layout of landing gear and systems, in Airplane Design (Roskam Aviation and Engineering, Ottawa, Kansas, 1985) Chap. Part IV.
- [14] H. Conway, Landing gear design. (Chapman and Hall,, London:, 1958).
- [15] N. S. Currey, *Aircraft Landing Gear Design Principles and Practices* (American Institute of Aeronautics and Astronautics, 1988).
- [16] M. C.-Y. Niu, Landing gear, in Airframe Structural Design Practical Design Information and Data on Aircraft Structures (AD Adaso/Adastra Engineering LLC, 1999) 2nd ed., pp. 430–470.
- [17] S. T. Chai and W. H. Mason, *Landing Gear Integration in Aircraft Conceptual Design. Revision*, Tech. Rep. (Virginia Polytechnic Inst. and State Univ., Blacksburg, 1997).
- [18] N. van Oene, Landing Gear Design Integration for the TU Delft Initiator, Msc thesis, Delt University of Technology (2019).
- [19] N. Heerens, Landing gear design in an automated design environment, Msc thesis, Delft University of Technology (2014).

- [20] D. R. Brill, COMFAA, (2014).
- [21] International Civil Aviation Organisation (ICAO), Aerodromes: annex 14 to the convention on international civil aviation Vol. 1, Aerodrome design and operations. (ICAO, Montreal:, 2004).
- [22] International Civil Aviation Organisation (ICAO), *Aerodrome Design Manual*, Tech. Rep. (International Civil Aviation Organization, Montreal, 2005).
- [23] M. A. Page, Tilting Landing Gear Systems and Methods, (2016).
- [24] B. Sankar, Effect Of Jump Strut Nose Landing Gear In Preliminary Design Of Aircraft, in AIAA Atmospheric Flight Mechanics Conference (American Institute of Aeronautics and Astronautics, Reston, Virigina, 2012).
- [25] A. Kazda and R. E. Caves, Airport design and operation (2015).
- [26] European Aviation Safety Agency (EASA), *CS-25 Easy Access Rules for Large Aeroplanes*, Tech. Rep. (European Aviation Safety Agency (EASA), 2018).
- [27] European Aviation Safety Agency (EASA), Certification Specifications and Acceptable Means of Compliance for Large Aeroplanes (CS-25, amendment 22), Tech. Rep. 22 (European Aviation Safety Agency (EASA), 2018).
- [28] The Royal Aeronautical Society, ESDU Data Items, Tech. Rep. 70023 (IHS ESDU, 1982).
- [29] The Royal Aeronautical Society, ESDU Data Items, Tech. Rep. A.06.01.00 (IHS ESDU, 1980).
- [30] The Royal Aeronautical Society, ESDU Data Items, Tech. Rep. A.07.01.00 (IHS ESDU, 2015).
- [31] J. Kay, W. H. Mason, and W. Durham, *Control authority assessment in aircraft conceptual design,* in *AIAA Aircraft Design, Systems and Operations Meeting* (American Institute of Aeronautics and Astronautics, Monterey, California, 1993).
- [32] A. Huebner, G. Rogé, S. Hitzel, K. Badcock, P. Eliasson, A. Khrabov, and M. Lahuta, *European Benchmark on Numerical Prediction of Stability and Control Derivatives*, in *27th AIAA Applied Aero-dynamics Conference* (American Institute of Aeronautics and Astronautics, San Antonio, Texas, 2009).
- [33] IHS Inc., IHS ESDU, (2019).
- [34] T. A. Toll and M. J. Queijo, *Approximate relations and charts for low-speed stability derivatives of swept wings*, Tech. Rep. (National Advisory Committee for Aeronautics, Langley Field, Virginia, 1948).
- [35] M. J. Bamber and R. O. House, *Wind-tunnel Investigation of Effect of Yaw on Lateral-stability Characteristics I : Four N.A.C.A. 23012 Wings of Various Plan Forms with and Without Dihedral*, Tech. Rep. (National Advisory Committee for Aeronautics, Langley Field, Virginia, 1939).
- [36] The Royal Aeronautical Society, ESDU Data Items, Tech. Rep. 76003 (IHS ESDU, 2011).
- [37] The Royal Aeronautical Society, ESDU Data Items, Tech. Rep. 79006 (IHS ESDU, 1999).
- [38] The Royal Aeronautical Society, ESDU Data Items, Tech. Rep. 82010 (IHS ESDU, 1982).
- [39] The Royal Aeronautical Society, ESDU Data Items, Tech. Rep. 70011 (IHS ESDU, 1970).
- [40] The Royal Aeronautical Society, ESDU Data Items, Tech. Rep. A.06.01.09 (IHS ESDU, 1970).
- [41] The Royal Aeronautical Society, ESDU Data Items, Tech. Rep. A.06.01.03 (IHS ESDU, 1970).
- [42] The Royal Aeronautical Society, ESDU Data Items, Tech. Rep. W.01.01.01 (IHS ESDU, 1989).
- [43] The Royal Aeronautical Society, ESDU Data Items, Tech. Rep. 80033 (IHS ESDU, 1963).
- [44] The Royal Aeronautical Society, ESDU Data Items, Tech. Rep. 73006 (IHS ESDU, 1973).

- [45] Airbus S.A.S., *A340-200/300 Aircraft Characteristics, Airport and Maintenance Planning*, Tech. Rep. (Airbus S.A.S., Blagnac, 2005).
- [46] Airbus S.A.S., *A330 Aircraft Characteristics, Airport and Maintenance Planning*, Tech. Rep. (Airbus S.A.S., Blagnac, 2005).
- [47] Airbus S.A.S., *A350 Aircraft Characteristics, Airport and Maintenance Planning*, Tech. Rep. (Airbus S.A.S., Blagnac, 2016).
- [48] Boeing Commercial Airplanes, 777-200/300 Airplane Characteristics for Airport Planning, Tech. Rep. July (Boeing Commercial Airplanes, Seattle, Washington, 1998).
- [49] Boeing Commercial Airplanes, 777-200LR/-300ER/-Freighter Airplane Characteristics for Airport Planning, Tech. Rep. May (Boeing Commercial Airplanes, Seattle, Washington, 2015).
- [50] Bridgestone Group, *Tire Specifications*, (2016).
- [51] The Goodyear Tire & Rubber Company, Global Aviation Tires, (2018).
- [52] European Aviation Safety Agency (EASA), Certification Specifications and Guidance Material for Aerodromes Design CS-ADR-DSN, Tech. Rep. 4 (European Aviation Safety Agency (EASA), 2017).
- [53] European Aviation Safety Agency (EASA), *Easy Access Rules for Aerodromes (Regulation (EU) No 139 / 2014)*, Tech. Rep. (European Aviation Safety Agency (EASA), 2018).
- [54] L. Savoni and R. Rudnik, *Pylon design for a short range transport aircraft with over-the-wing mounted uhbr engines*, AIAA Aerospace Sciences Meeting, 2018, 1 (2018).
- [55] R. Munjulury, P. Berry, D. Borhani Coca, A. Parés Prat, and P. Krus, *Analytical weight estimation of landing gear designs*, Proceedings of the Institution of Mechanical Engineers, Part G: Journal of Aerospace Engineering **231**, 2214 (2017).
- [56] C. J. Xue, J. H. Dai, T. Wei, B. Liu, Y. Q. Deng, and J. Ma, *Structural Optimization of a Nose Landing Gear Considering Its Fatigue Life*, Journal of Aircraft **49**, 225 (2012).
- [57] J. Wong, L. Ryan, and I. Y. Kim, *Design optimization of aircraft landing gear assembly under dynamic loading*, Structural and Multidisciplinary Optimization **57**, 1357 (2018).
- [58] D. S. Lacy and A. J. Sclafani, *Development of the high lift common research model (HL-CRM): A representative high lift configuration for transports,* in *54th AIAA Aerospace Sciences Meeting*, January (American Institute of Aeronautics and Astronautics, San Diego, California, 2016) pp. 1–24.
- [59] M. Rivers, C. Hunter, and V. Vatsa, Computational fluid dynamic analyses for the high-lift common research model using the USM3D and FUN3D flow solvers, in AIAA SciTech Forum - 55th AIAA Aerospace Sciences Meeting, January 2017 (American Institute of Aeronautics and Astronautics, Grapevine, Texas, 2017) pp. 1–26.
- [60] E. Obert, R. Slingerland, D. J. W. Leusink, T. van den. Berg, J. H. Koning, M. J. L. van. Tooren, Technische Hogeschool Delft. Afdeling der Luchtvaart- en Ruimtevaarttechniek., and IOS Press., *Aerodynamic design of transport aircraft* (Ios Press, Amsterdam, the Netherlands:, 2009).
- [61] L. Jenkinson, P. Simpkin, and D. Rhodes, *Civil Jet Aircraft Design, Data Sets, Table 8 Miscellaneous Manufacturers,* (1999).
- [62] F. Jiang, M. Y. An, and S. J. Mysko, *Computational analysis of aileron effectiveness characteristics on an advanced wing,* in *18th Applied Aerodynamics Conference* (American Institute of Aeronautics and Astronautics, Longbeach, California, 2000) pp. 541–551.
- [63] F. Jiang, Assessing computational fluid dynamics predictions for control surface effectiveness, Journal of Aircraft **38**, 1032 (2001).

- [64] R. M. Rennie and E. J. Jumper, *Experimental Measurements of Dynamic Control Surface Effectiveness*, Journal of Aircraft **33**, 880 (1996).
- [65] S. M. Waters, M. Voskuijl, L. L. M. Veldhuis, and F. J. J. M. M. Geuskens, *Control allocation performance for blended wing body aircraft and its impact on control surface design, Aerospace Science and Technology* **29**, 18 (2013).
- [66] H. V. de Castro, Flying and handling qualities of a fly-by-wire blended-wing-body civil transport aircraft, Ph.D. thesis, Cranfield University (2003).
- [67] F. O. Smetana, D. C. Summery, and W. D. Johnson, *Riding and handling qualities of light aircraft: A review and analysis*, Tech. Rep. (North Carolina State Univ.; NASA, Raleigh, 1972).
- [68] European Aviation Safety Agency (EASA), *Type-Certificate Data sheet for Trent XWB series engines*, (2018).
- [69] A. J. Santosh, *Influence of Ground Effect on the Flying V aircraft*, Msc thesis, Delft University of Technology (2020).
- [70] H. L. J. Morgan. and J. W. J. Paulson, *Low-speed aerodynamic performance of a high-aspect-ratio supercritical-wing transport model equipped with full-span slat and part-span double-slotted flaps*, Tech. Rep. (NASA Langley Research Center, Hampton, Virginia, 1979).